

# Volatile Organic Compound Detection Using Insect Odorant-Receptor Functionalised Field-Effect Transistors

by

Eddyn Oswald Perkins Treacher

A thesis submitted in fulfilment of the  
requirements of the degree of  
Doctor of Philosophy in Physics  
School of Physical and Chemical Sciences  
Te Herenga Waka - Victoria University of Wellington

Apr 2024





# Table of contents

<b>Acknowledgements</b>	<b>1</b>
<b>1. Characteristics of Pristine Carbon Nanotube &amp; Graphene Field Effect Transistors</b>	<b>3</b>
1.1. Introduction . . . . .	3
1.2. Carbon Nanotube Network Morphology and Composition . . . . .	4
1.2.1. Atomic Force Microscopy . . . . .	4
1.2.2. Raman Spectroscopy . . . . .	10
1.3. Electrical Characteristics of Pristine Devices . . . . .	12
1.3.1. Python Analysis . . . . .	12
1.3.2. Carbon Nanotube Network Devices . . . . .	14
1.3.3. Graphene Devices . . . . .	19
1.4. Aqueous Sensing of Phosphate Buffered Saline Concentration . . . . .	21
1.4.1. Control Series and Baseline Drift . . . . .	21
1.4.2. Sensing Series . . . . .	25
1.5. Vapour Sensing with Ethyl Hexanoate . . . . .	30
1.5.1. Baseline Drift . . . . .	30
1.5.2. Sensing Series . . . . .	33
1.6. Conclusion . . . . .	36
<b>2. Non-Covalent Functionalisation of Carbon Nanotubes and Graphene</b>	<b>39</b>
2.1. Introduction . . . . .	39
2.2. Non-Covalent Bonding and $\pi$ -Stacking . . . . .	39
2.3. Attachment of 1-Pyrenebutanoic Acid N-Hydroxysuccinimide Ester . . . . .	41
2.3.1. Comparing Attachment Methods . . . . .	41
2.3.2. Examining 1-Pyrenebutanoic Acid N-Hydroxysuccinimide Ester Purity . . . . .	45
2.3.3. Electrical Characterisation . . . . .	46
2.4. Attachment of 1-Pyrenebutyric Acid . . . . .	50
2.4.1. Comparing Attachment Methods . . . . .	50
2.4.2. Raman Spectroscopy . . . . .	50
2.4.3. Electrical Characterisation . . . . .	52
2.5. Attachment of PEGlyated Pyrene-Based Linkers . . . . .	54
2.5.1. Pyrene-NTA, Pyrene-Biotin and PEGylation . . . . .	54
2.6. Identifying Functionalisation Issues using Fluorescence Microscopy . . . . .	55
2.6.1. General Overview . . . . .	55

*Table of contents*

2.6.2. Photoresist Contamination . . . . .	56
2.6.3. Hydrophobicity of Carbon Nanotubes and Graphene . . . . .	58
2.6.4. Substrate Interaction with Linker Molecules . . . . .	61
2.6.5. Coffee-Ring Effect . . . . .	61
2.7. Verifying Linker-OR Nanodisc Attachment with Fluorescence Microscopy	62
2.7.1. GFP-OR Nanodisc Functionalisation . . . . .	62
2.7.2. Fluorescence Microscopy . . . . .	63
2.8. Conclusion . . . . .	65
<b>3. Biosensing with Insect Odorant-Receptor Functionalised Carbon Nanotube Devices</b>	<b>67</b>
3.1. Introduction . . . . .	67
3.2. Aqueous Sensing of Ethyl Hexanoate with OR22a-functionalised Carbon Nanotube Transistor . . . . .	67
3.2.1. OR Nanodisc Functionalisation . . . . .	67
3.2.2. Aqueous Sensing of Ethyl Hexanoate . . . . .	72
3.3. Variability in Biosensor Behaviour . . . . .	76
3.4. Potential Sources of Variability . . . . .	81
3.4.1. Surfactant Contamination . . . . .	82
3.4.2. Aggregation of Odorant Receptor Nanodiscs . . . . .	82
3.4.3. Solvent Contamination . . . . .	82
3.5. Other Sources of Variability . . . . .	82
3.6. Vapour Sensing with Empty Nanodiscs . . . . .	82
3.7. Conclusion . . . . .	82
<b>Appendices</b>	<b>83</b>
<b>A. Vapour System Hardware</b>	<b>83</b>
<b>B. Python Code for Data Analysis</b>	<b>85</b>
B.1. Code Repository . . . . .	85
B.2. Atomic Force Microscope Histogram Analysis . . . . .	85
B.3. Raman Spectroscopy Analysis . . . . .	85
B.4. Field-Effect Transistor Analysis . . . . .	85

# Acknowledgements

69450

Rifat, Alex - vapour sensor  
Erica Cassie - FET sensing setup  
Rob Keyzers and Jennie Ramirez-Garcia - NMR spectra  
Patricia Hunt - Computational chemistry



# 1. Characteristics of Pristine Carbon Nanotube & Graphene Field Effect Transistors

## 1.1. Introduction

A range of methods were followed to fabricate carbon nanotube network and graphene field-effect transistors for biosensor use. This chapter therefore looks to use the characterisation techniques outlined in the previous chapter to compare and contrast the device channel morphologies and electrical characteristics resulting from various methods.

The three carbon nanotube film types used for devices were the solvent-deposited, surfactant-deposited and steam-assisted surfactant-deposited (steam-deposited) films discussed in the previous chapter. As minor changes were made to fabrication processes throughout the thesis, the fabrication dates of devices used are stated, which can be cross-referenced with **?@sec-fabrication** to identify the specific process used. Atomic force microscopy and Raman spectroscopy was performed on the carbon nanotube networks to identify the distribution of carbon nanotube diameters and the defects present on the carbon nanotube networks. Electrical characterisation was then used to see how the morphology of each film type affects the performance of the completed devices. Both back-gated and liquid-gated transfer characteristics were compared, as well as key parameters taken from the liquid-gated characteristics. The electrical behaviour of liquid-gated graphene devices was also examined, as well as the impact of water on the performance of back-gated devices for vapour sensing use.

Finally, as a control measurement for liquid-gated sensing and to verify the behaviour of the pristine device as a sensor, a salt concentration sensing series was performed with a steam-deposited carbon nanotube network device. The device characteristics were taken and device drift was examined and modelled. The sensing series was performed by successively diluting 1XPBS electrolyte in the polydimethylsiloxane ‘well’ (electrolyte container) while passing a current through the device, and measuring the current response to dilutions. Various filters were applied to the collected data to better understand the signal change.

## 1.2. Carbon Nanotube Network Morphology and Composition

### 1.2.1. Atomic Force Microscopy

Figure 1.1 shows a side-by-side comparison of the surface morphology of carbon nanotube films fabricated using the methods described in [?@sec-dep-carbon-nanotubes](#). These images were collected using an atomic force microscope and processed in the manner described in [?@sec-afm-characterisation](#). Figure 1.1a shows a film of carbon nanotubes deposited in solvent, Figure 1.1c shows a film of carbon nanotubes dropcast in surfactant, and Figure 1.1e shows carbon nanotubes dropcast in surfactant in the presence of steam. As discussed in previous works using solvent-based deposition techniques for depositing carbon nanotubes, in each network multi-tube bundles form due to strong mutual attraction between nanotubes [1]–[4]. However, when surfactants are present, they adsorb onto the carbon nanotubes and form a highly repulsive structure able to overcome the strong attraction between nanotubes. This repulsion keeps the individual carbon nanotubes more isolated [5]–[9]. The diameter range provided by the supplier for the individual carbon nanotubes used is 1.2–1.7 nm, while the length range is 0.3–5.0 µm (Nanointegris).

It has previously been demonstrated that the diameter range of deposited single-walled carbon nanotubes can be modelled via a normal or Gaussian distribution [10]–[12]. However, when the height profiles from the 2.5 µm × 2.5 µm AFM images are directly extracted and binned, as plotted in black in Figure 1.1, the histograms obtained do not follow a normal distribution. One reason for this result is the surface roughness of the silicon dioxide substrate. The carbon nanotubes do not lie perfectly level on a perfectly level silicon oxide substrate. In practice, both the SiO<sub>2</sub> substrate and the surface of the carbon nanotubes both have a degree of roughness. To find the contribution of surface roughness to the height profile histogram corresponding to each network deposition method, silicon dioxide substrates were modified using the same processes as in Figure 1.1 but without carbon nanotubes present in the solutions used. 2.5 µm × 2.5 µm AFM images of the modified surfaces are shown in Figure 1.2.

$$f(x) = \frac{2}{\omega} \phi\left(\frac{x - \xi}{\omega}\right) \Phi\left(\alpha\left(\frac{x - \xi}{\omega}\right)\right) \quad (1.1)$$

In Figure 1.2, it appears that each substrate surface has a roughness that follows a normal distribution with some degree of skewness. Figure 1.2b and Figure 1.2d are negatively skewed distributions. The equation for a skew-normal distribution is given in Equation 1.1, where  $\alpha$  is the “shape parameter”,  $\xi$  is the “location parameter”,  $\omega$  is the “scale parameter”,  $\phi(x)$  is the standard normal distribution and  $\Phi(x)$  is the corresponding cumulative distribution function.  $\alpha$  indicates the skewness of the distribution.  $\xi$  and  $\omega$  correspond to the mean and standard deviation of the skew-free normal distribution

## 1.2. Carbon Nanotube Network Morphology and Composition

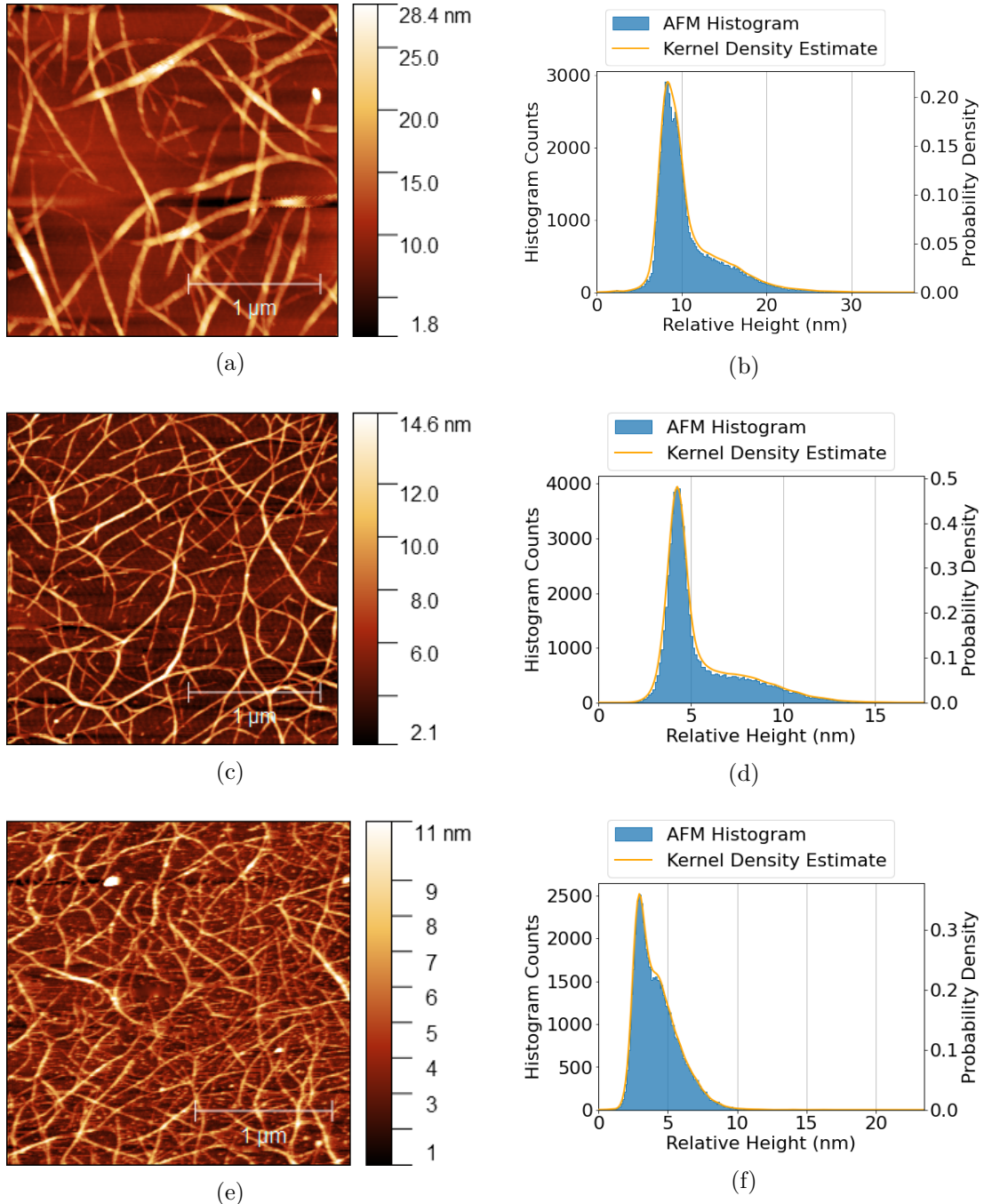


Figure 1.1.:  $2.5 \mu\text{m} \times 2.5 \mu\text{m}$  atomic force microscope (AFM) images of carbon nanotube films deposited using various methods, shown side-by-side with histogram height distributions and kernel density estimate (KDE) plots corresponding to each image. The network shown in (a) with height distribution shown in (b) was deposited in solvent, the network shown in (c) with height distribution shown in (d) was dropcast in surfactant, and the network shown in (e) with height distribution shown in (f) was dropcast in surfactant with steam present.

## 1. Characteristics of Pristine Carbon Nanotube & Graphene Field Effect Transistors

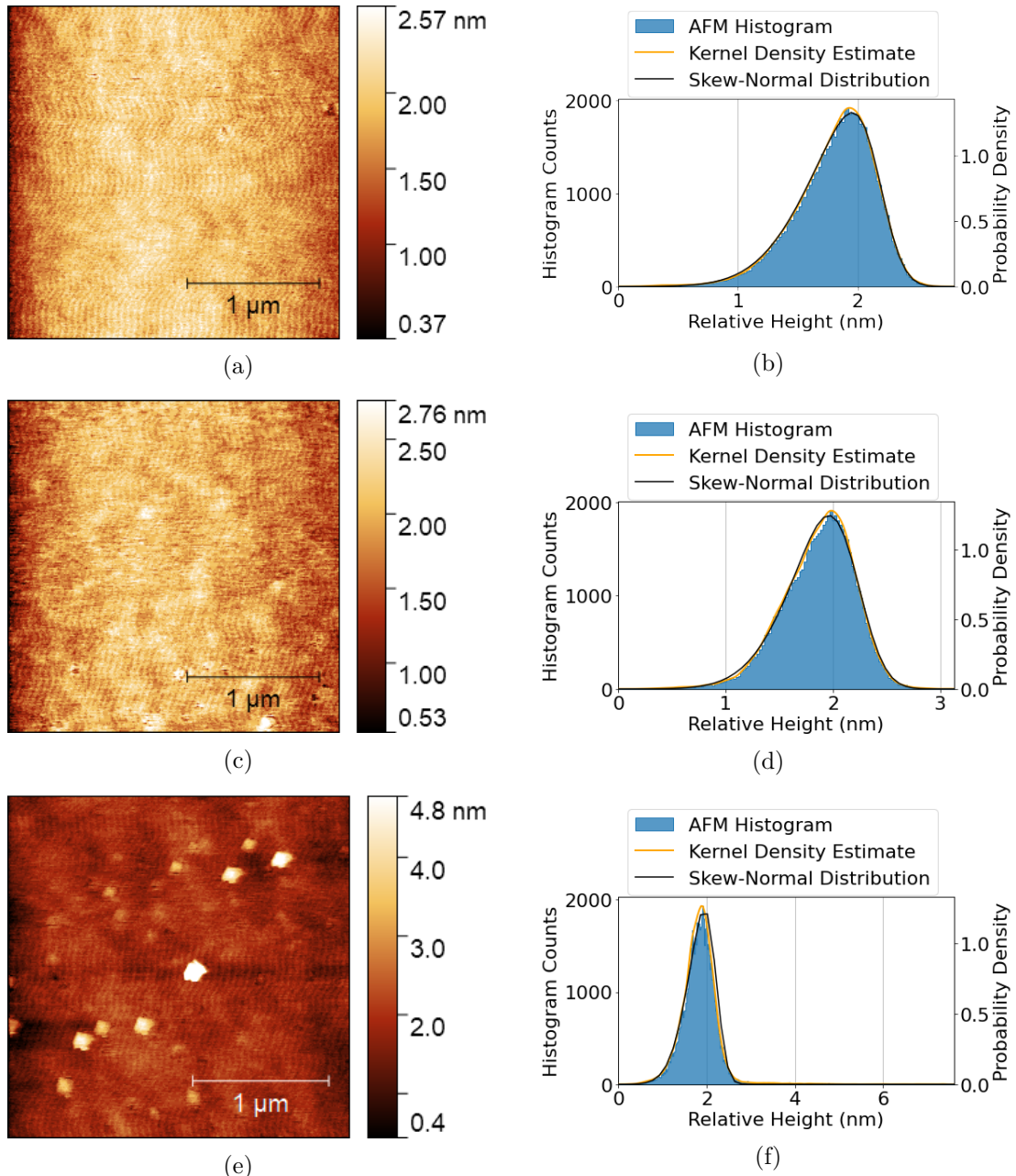


Figure 1.2.:  $2.5 \mu\text{m} \times 2.5 \mu\text{m}$  atomic force microscope (AFM) images of silicon dioxide substrates alongside histogram height distributions and KDE plots corresponding to each image. The substrate in (a) and (b) was exposed to solvent, the substrate in (c) and (d) was exposed to surfactant, and the substrate in (e) and (f) was exposed to surfactant with steam present.

## 1.2. Carbon Nanotube Network Morphology and Composition

when  $\alpha$  is set equal to zero [13]. The fitted skew-normal distribution in Figure 1.2b has  $\alpha = -3.2$ ,  $\xi = 2.2$  nm and  $\omega = 0.5$  nm, while in Figure 1.2d  $\alpha = -2.2$ ,  $\xi = 2.2$  nm and  $\omega = 0.5$  nm. The close correspondence between  $\xi$  and  $\omega$  for these distributions but not  $\alpha$  implies that the skewness is a variable imaging or processing artifact rather than a physical property of the surface. Without distortion, the roughness of a clean SiO<sub>2</sub> surface should follow a normal distribution [14].

However, Figure 1.2f has a pronounced positive skew with a long tail. The tail appears to result from the contribution of residual surfactant aggregates to surface morphology, observed in Figure 1.2e and recently discussed elsewhere in the literature [12], [15]. Attempting to fit a skew-normal distribution to this histogram fails when all three variables are allowed to vary due to the presence of the tail. Instead, previous values obtained for  $\xi$  and  $\omega$  can be used for the fitting process, with only  $\alpha$  allowed to change. Fixing  $\xi$  and  $\omega$  at 2.2 nm and 0.5 nm respectively gives the result shown in Figure 1.2f. The fitted distribution has an  $\alpha$  of -2.4. The distribution closely fits the negative tail of the histogram, but deviates slightly from the positive tail due to the presence of surfactant. Since this deviation is small, the quality of the fit is still reasonably high, with an R-squared value of 0.98. Surfactant contamination could have negative effects on both sensitivity of carbon nanotubes and also could damage attached biological elements.

Using the morphology analysis technique outlined by Vobornik *et al.* [12], five successive diameter measurements of 30 carbon nanotube bundles were collected using Gwyddion. Measurements were not taken at bundle junctions. A height threshold ‘mask’ was defined in Gwyddion to determine average substrate height, as shown in Figure 1.3a. This background value was subtracted from our diameter measurements to determine the actual bundle height. The mean background heights of the solvent-deposited, surfactant-deposited and steam-assisted surfactant-deposited bundle diameter histograms were  $8.8 \pm 4.0$  nm,  $4.2 \pm 1.8$  nm and  $3.3 \pm 1.0$  nm respectively. An increased maximum feature height leads to an increased mean background height, and by examining the AFM images in Figure 1.1 it appears this may be due to deep artifacts on the surface of the substrate in the vicinity of large features. The average of the five height-adjusted values for each carbon nanotube bundle was then calculated, and these 30 averages were sorted into six equal-sized bins. The binned bundle diameter measurements, alongside estimated probability density, are shown in Figure 1.3.

From Figure 1.3, it is clear that each histogram appears to follow a positively skewed normal distribution, different to the skew-free normal distribution expected from previous works [10]–[12]. The skew is likely another artifact from imaging the network with the atomic force microscope. The force of the atomic force microscope tip is known to cause larger bundles to undergo some degree of compression, and the resulting systematic underestimation of their height may be responsible for the distribution skewness [12]. The fitted skew-normal distribution in Figure 1.3b has  $\alpha = 2.7$  (shape; skew),  $\xi = 4.3$  nm (location; mean),  $\omega = 5.9$  nm (scale; standard deviation), the distribution in Figure 1.3c has  $\alpha = 2.4$ ,  $\xi = 2.2$  nm,  $\omega = 2.6$  nm, and the distribution in Figure 1.3d has  $\alpha = 3.6$ ,  $\xi = 2.2$  nm and  $\omega = 1.5$  nm. The probability density for the carbon nanotube

1. Characteristics of Pristine Carbon Nanotube & Graphene Field Effect Transistors

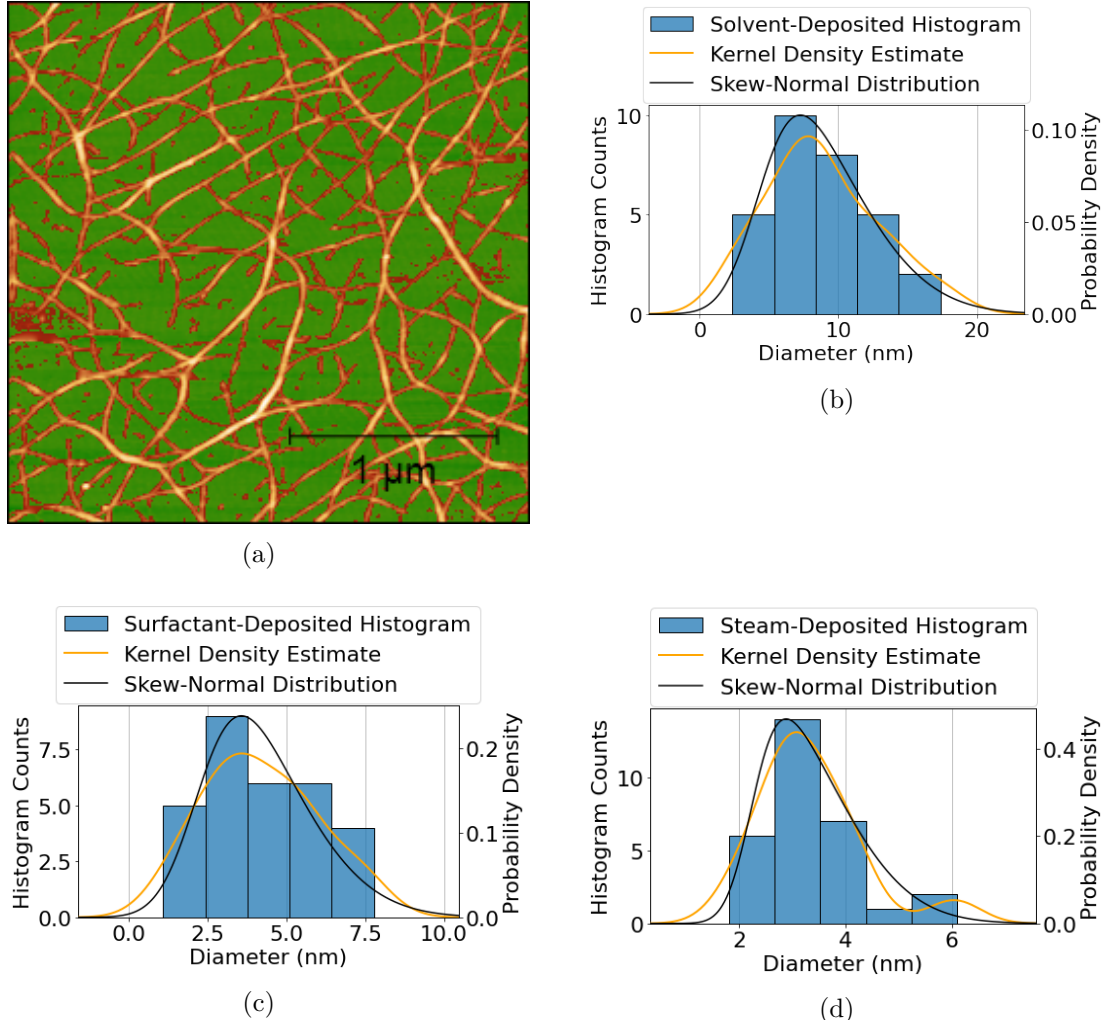


Figure 1.3.: An masked AFM image is shown in (a), where the masked carbon nanotube bundles are shaded blue. The mask sets a height threshold so that masked features are excluded from the height dataset. Histogram height distributions with corresponding KDE plots collected via the morphology analysis method outlined by Vobornik *et al.* [12] are shown in (b)-(d). The substrate in (b) was exposed to solvent, the substrate in (c) was exposed to surfactant, and the substrate in (d) was exposed to surfactant with steam present.

## 1.2. Carbon Nanotube Network Morphology and Composition

bundle histogram drops to approximately zero at or before 0 nm, which is physically appropriate.

Warning: package 'kableExtra' was built under R version 4.3.3

Table 1.1.: The first eight optimised ratios of 2D packed circle diameter to encompassing circle diameter, given to 3 s.f. (encompassing circle diameter =  $d$ , number of packed circles =  $n$ , approximate packed circle diameter =  $d_n$ ).

$n$	2	3	4	5	6	7	8	9
$d/d_n$	2.00	2.15	2.41	2.70	3.00	3.00	3.30	3.61

Previously, analysis of the morphology of carbon nanotube networks has been simplified by assuming the component nanotubes are cylinders, follow 2D packing and are of equal diameter [2]. Table 1.1 shows the relationship between the diameter of a bundle of 2D packed cylinders and the constituent diameters of up to nine cylinders within that bundle. From looking up the relevant  $d/d_n$  packing ratios, and assuming an average carbon nanotube diameter of 1.45 nm, it is possible to use Table 1.1 to find the approximate number of nanotubes  $n$  likely to be present in the mean bundle size corresponding to each deposition type [16], [17]. These estimates are shown in Table 1.2. Also shown in Table 1.2 is an estimate of the ratio of single- to multi-tube bundles for each deposition. This estimate was obtained by taking the integral of each distribution with a lower bound of 2.9 nm, the minimum multi-tube bundle size for 1.45 nm diameter nanotubes. As the area under the curve represents the probability a bundle will have a particular diameter, this integral should give a good estimate of the relative proportion of multi-tube bundles. Table 1.2 should be interpreted as lower-limit estimates of the size and relative proportion of bundles, recalling that the distribution skewness indicates underestimation of the true bundle height.

Table 1.2.: The mean of histogram distributions for carbon nanotube films deposited using various methods, alongside estimates for the number of nanotubes present per mean bundle and the estimated proportion of multi-tubed bundles present across the network.

	Mean Bundle Diameter (nm)	Tubes per Average Bundle	% Multi-Tube Bundles
Solvent deposited	$8.8 \pm 4.0$	28	> 96%
Surfactant deposited	$4.2 \pm 1.8$	5	> 75%
Surfactant deposited with steam	$3.3 \pm 1.0$	3	> 65%

## *1. Characteristics of Pristine Carbon Nanotube & Graphene Field Effect Transistors*

Both the carbon nanotube bundle diameter mean and standard deviation are small for surfactant-deposited films when compared to the mean and standard deviation of solvent-deposited films. However, despite the presence of surfactant, it is apparent both from Figure 1.1 and Table 1.2 that not all surfactant-dispersed carbon nanotubes are deposited individually. Bundling may occur during the process of deposition onto the substrate, which could disrupt the repulsive forces from the surfactant coating and allow attractive forces to temporarily dominate. It is possible that the bundling of surfactant-dispersed carbon nanotubes is a consequence of dynamics introduced by the coffee-ring effect [18], [19]. The coffee-ring effect refers to a build-up of dispersed solid forming around the edges of a dispersion evaporating on a surface. This process occurs due to the dispersion edges being fixed by surface forces, leading to capillary flow outwards to replace liquid evaporating at the edges, bringing solid material along with it. The presence of vapour is known to disrupt this capillary effect [20], which may explain why mean bundle diameter is lower for the films deposited in surfactant with steam present relative to films deposited in surfactant without steam.

The discussion in this section gives us a new understanding of the histograms shown in Figure 1.1. It is now apparent that these histograms are linear combinations of skewed normal distributions. These distributions include a negatively-skewed distribution corresponding to the substrate surface and a positively-skewed distribution corresponding to the carbon nanotube bundles. X and Y junctions between overlapping nanotubes may also form a similarly skewed normal distribution as part of the full histogram [2]. The complete linear combination could be modelled mathematically in order to rapidly extract key parameters from atomic force microscope images [21], but implementing this approach is outside of the scope of this thesis. Another outcome of this discussion is awareness that carbon nanotube bundling within a network is lowered by the presence of surfactant during deposition. Introducing steam when depositing with surfactant lowers bundling even further, but also leads to residual surfactant pooling and attaching to the substrate surface. These results may both be explained by the presence of steam enabling surfactant to follow carbon nanotubes to the substrate surface, which keeps them from bundling during the attachment process. The unwanted persistence of surfactant means that higher temperature vacuum annealing may be required for robust biosensors [22].

### **1.2.2. Raman Spectroscopy**

Raman spectroscopy was also used to analyse and compare the deposited carbon nanotube networks. Raman spectra were collected from a solvent-deposited carbon nanotube film and a steam-assisted surfactant-deposited film, both on silicon dioxide, in the manner described in **?@sec-raman-characterisation**. These spectra were then processed using the Python script mentioned in Section B.3. For each location, spectra over two wavenumber ranges were collected. A peak corresponding to the silicon dioxide substrate, found in the range between  $100\text{ cm}^{-1}$  and  $650\text{ cm}^{-1}$ , was used as a reference

## 1.2. Carbon Nanotube Network Morphology and Composition

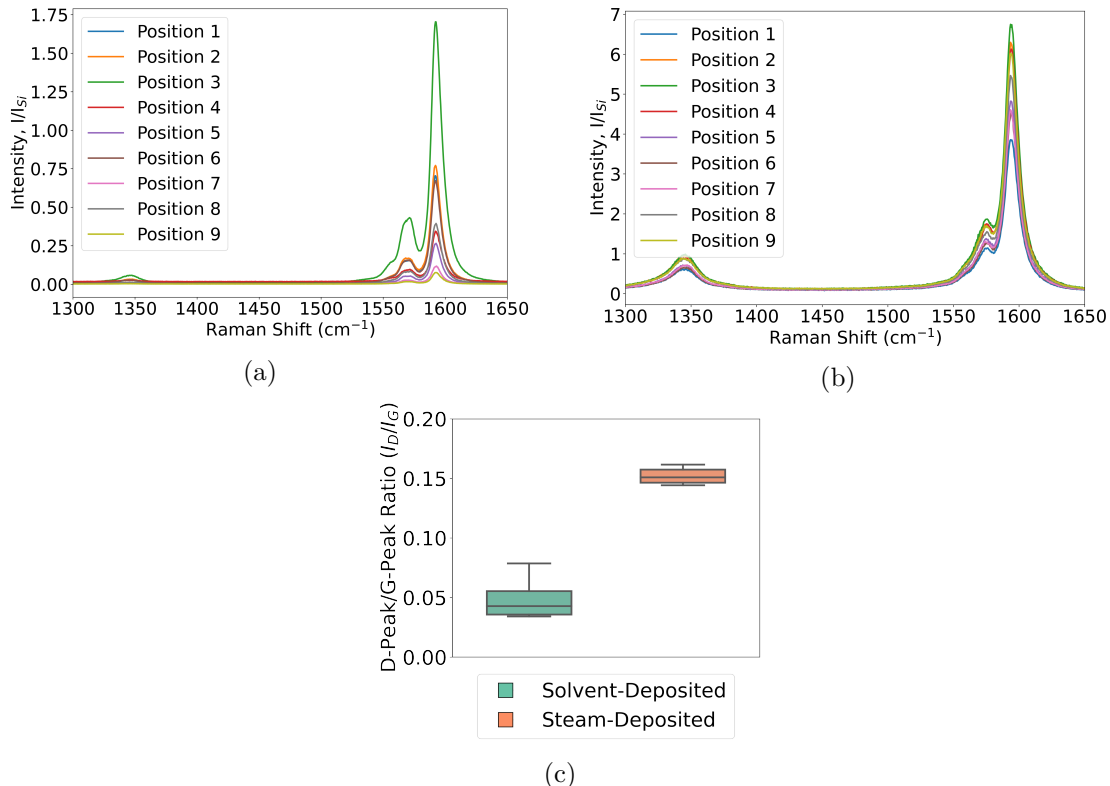


Figure 1.4.: A series of nine Raman spectra at different locations across a  $40 \mu\text{m} \times 100 \mu\text{m}$  carbon nanotube film region, where (a) shows spectra from a film deposited using solvent while (b) shows spectra from a film deposited with surfactant in the presence of steam. (c) shows the spread of the D-peak/G<sup>+</sup>-peak spectral ratios corresponding to each film.

## *1. Characteristics of Pristine Carbon Nanotube & Graphene Field Effect Transistors*

peak for the normalisation of intensity across the wavenumber range between  $1300\text{ cm}^{-1}$  and  $1650\text{ cm}^{-1}$ . These normalised spectra are shown in Figure 1.4. In all spectra, a D-band comprising a single D-peak is observed at  $\sim 1320\text{ cm}^{-1}$ , and a G-band comprising two G-peaks,  $G^-$  and  $G^+$ , is observed between  $\sim 1525\text{ cm}^{-1}$  and  $\sim 1650\text{ cm}^{-1}$ . These features are characteristic of networks of semiconducting carbon nanotubes [23], [24].

Closer inspection of the D peak and G peaks can give us important information about network composition.  $G^-$  is a minor peak found at  $\sim 1570\text{ cm}^{-1}$ , while  $G^+$  is a larger feature at  $\sim 1590\text{ cm}^{-1}$ . The  $G^+$  feature describes the in-plane vibration of carbon bonds along the length of the carbon nanotubes, while the  $G^-$  feature describes the in-plane vibration of bonds about the nanotube circumference [24], [25]. The splitting between the wavenumber location of the  $G^-$  and  $G^+$  local maxima is lower in Figure 1.4b than in Figure 1.4a, indicating more metallic nanotubes are present in the surfactant-deposited network [25]. The D-peak gives an indication of the defects present in the carbon nanotube atomic structure [24], [25]. The size of the normalised D-peak appears much lower in Figure 1.4a than in Figure 1.4b, indicating the solvent deposition process introduces less defects to the carbon nanotubes than surfactant-mediated deposition.

It is also possible to compare the relative magnitude of the D-peak and  $G^+$ -peak intensity to quantify carbon nanotube structural disorder, which disrupts in-plane lattice vibration [23], [24]. Figure 1.4c gives a summary of the ratios between the D-peak and  $G^+$ -peak across all nine positions for the solvent-deposited and surfactant-deposited film. It is immediately observed that  $I_D/I_G$  is significantly larger for the steam-assisted, surfactant-deposited films than for the solvent-deposited films. This is a further indication of the presence of defects across the steam-deposited network. These defects are likely introduced through the introduction of charge impurities by surfactant aggregates present around the carbon nanotubes [15]. However, at the same time, the range of values for the  $I_D/I_G$  ratio is lower for the steam-deposited network. This spatially homogeneous vibrational behaviour implies the steam-deposited network is more evenly distributed than the solvent-deposited network, which matches the discussion in Section 1.2.

## **1.3. Electrical Characteristics of Pristine Devices**

### **1.3.1. Python Analysis**

Analysis of electrical measurements was performed using the three modules described in Section B.4. The first of the three modules is for processing sensing datasets. This module cleans, analyses and filters sensing data and produces a variety of plots. These plots include normalised plots (type of normalisation can be set in the code config file), plots with fitted curves, plots with the linear baseline drift removed, plots of signal with analyte addition, “despiked” plots and “filtered” plots. The analysis used to produce these plots is described further below. It is possible to add annotations to any of these plots using the config file, and it is possible to produce a plot with a combination of these

### 1.3. Electrical Characteristics of Pristine Devices

modifications. The module can also fit exponential and linear trendlines to regions of the sensing data, and find the signal change per analyte addition; the module then returns spreadsheets containing the results of these analyses, including the standard deviation for all calculated parameters.

The `scipy.optimize.curve_fit` function is used in the first module to fit linear and exponential curves to regions of interest of the sensing data. For a linear fit  $c_1 t + c_2$ , initial parameters are simply set as  $c_1 = 1$  and  $c_2 = 0$ . For an exponential fit  $I_0 \exp(-t/\tau) + I_C$ , rough approximations are used for the initial parameters:  $I_C$  is set as the final current measurement of the region of interest,  $I_0$  is set as the initial current measurement minus  $I_C$ , and  $\tau$  is set as the time where current has dropped to  $e^{-1}I_0 + I_C$ .

“Despiked” plots have had spurious datapoints removed through the use of an interquartile range rolling filter. The window size of the rolling filter used was 40 datapoints, and datapoints in each window with a z-score above  $\pm 3$  were removed from the plotted/processed data. “Filtered” plots had noise reduced using a moving median filter. The moving median filter is more effective at removing noise than a simple moving average, and has advantages over other filters (such as the Savitzky-Golay filter) when removing noise from data with sharp edges, as is the case for sensing data. Median filtering can also be used for baseline drift compensation, though this approach was not used in this thesis [26]. The moving median filter used had a window of 40 datapoints.

Plots of signal with analyte addition were constructed from current data after first removing baseline drift and applying a moving median filter. A simple difference calculation between the mean of the filtered current before an addition and the mean of the filtered current after the addition was performed at each addition. These differences were then normalised relative to the initial current. The signal with analyte addition give reasonably consistent results regardless of whether baseline drift was removed from the data, as shown in Figure 1.5. We can therefore be confident that robust signal with analyte addition plots are robust even in the presence of significant drift.

The second module creates combined and individual plots of transfer data collected from eight channels on a single device. In combined plots, channels which are non-working, due to being shorted or non-conducting, are removed via setting a maximum and minimum possible on-current in the config file. Various parameters from the transfer characteristics are saved as a spreadsheet along with standard error. These parameters include on current, off current, subthreshold slope and threshold voltage for the carbon nanotube devices, and on current, off current and major Dirac point voltage for graphene devices. The device type being analysed can be set in the config file.

The third module allows for comparison of transfer measurements taken of the same channel before and after some modification. It also calculates the shift in either threshold voltage or major Dirac voltage of the device.

## 1. Characteristics of Pristine Carbon Nanotube & Graphene Field Effect Transistors

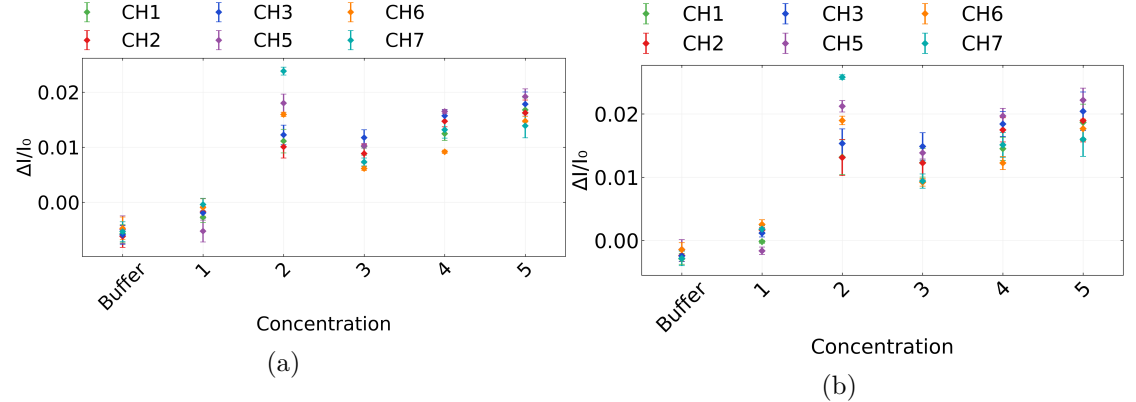


Figure 1.5.: A comparison of signal with analyte addition plots taken from the same salt concentration sensing dataset (the same dataset as used in Figure 1.11). In (a), a simple difference calculation performed on filtered data was used, while in (b) the same calculation was performed on filtered data with the baseline drift removed, the method used in the body of the thesis.

### 1.3.2. Carbon Nanotube Network Devices

Each carbon nanotube device fabricated was electrically characterised as described in [?@sec-electrical-characterisation](#), and electrical data was analysed using the Python code discussed in Section B.4. Devices with a 100 nm or 300 nm SiO<sub>2</sub> layer were used for liquid gated measurements, and devices with a 100 nm SiO<sub>2</sub> layer were used for backgated measurements. Figure 1.6 displays multi-channel measurements of representative devices fabricated as described in [?@sec-fabrication](#). To ensure a consistent comparison, each device here was encapsulated with AZ® 1518 encapsulation before measurements were taken. The channels which did not exhibit reliable transistor characteristics are not shown. These ‘non-working’ channels were either shorted, due to metal remaining on the channel after lift-off, or were very low current, due to a very sparse carbon nanotube network. Devices shown here with a solvent-deposited carbon nanotube network were fabricated prior to Jan 2022; devices with a surfactant-deposited network without steam present were fabricated prior to Jun 2021; devices with a surfactant-deposited network without steam were fabricated prior to Sep 2022.

#### Liquid-Gated CNTFETs

The liquid-gated devices in Figure 1.6a, Figure 1.6c and Figure 1.6e each exhibited ambipolar characteristics, commonly observed in liquid-gated carbon nanotube network FETs [2], [27]–[31]. When devices were appropriately configured, leakage current (shown by the dashed traces) did not exceed  $\sim 1 \times 10^{-7}$  V across the forward and reverse sweep. The devices shown which used steam-deposited carbon nanotube films showed the least

### 1.3. Electrical Characteristics of Pristine Devices

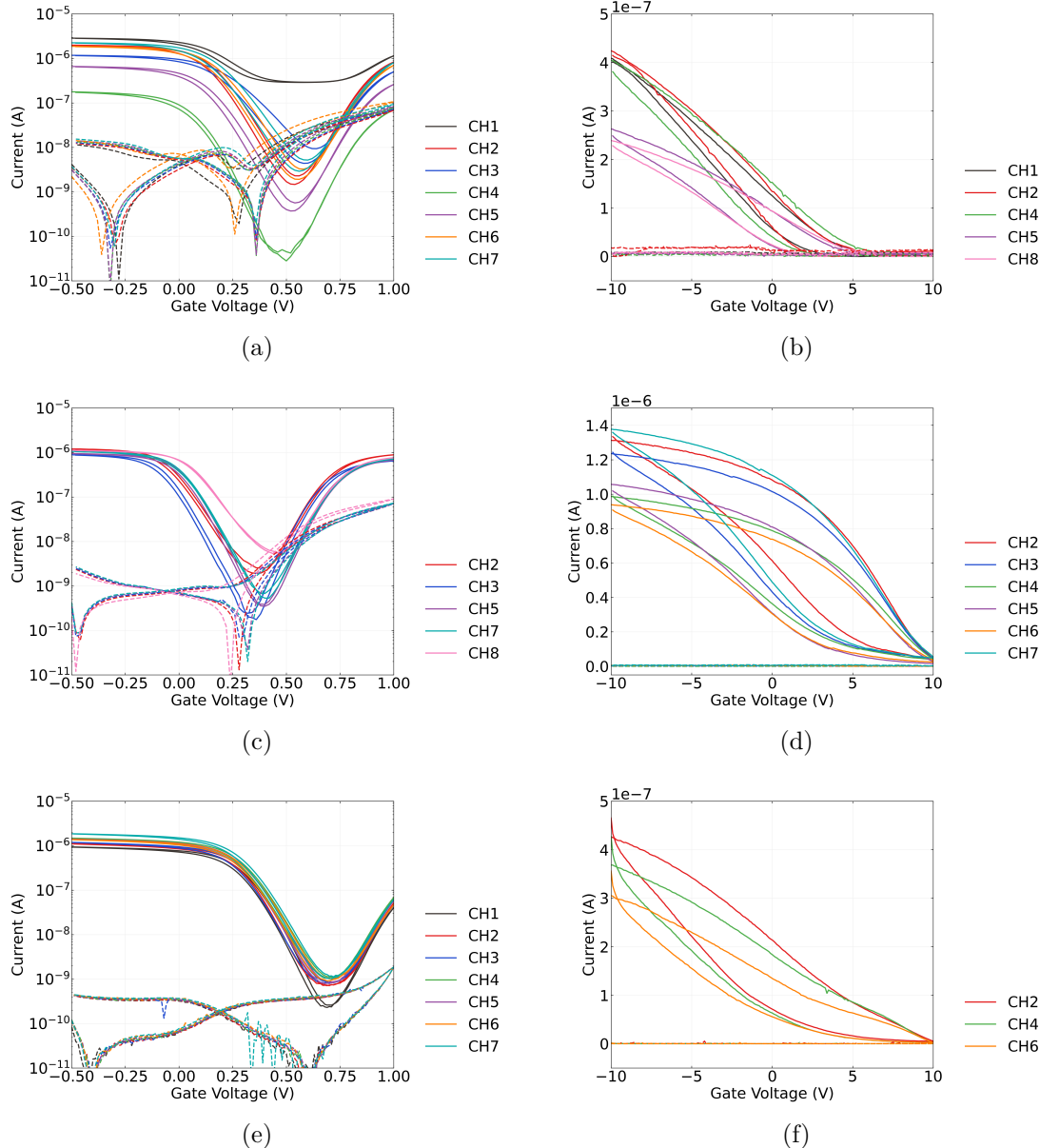


Figure 1.6.: Liquid-gated (left) and back-gated (right) transfer characteristics of AZ® 1518 encapsulated field-effect transistors, where the film was deposited with solvent in (a) and (b), deposited with surfactant in (c) and (d), and deposited with surfactant in the presence of steam in (e) and (f). A step size of 100 mV was used for the backgated sweeps in (a), (c) and (e), while a step size of 20 mV was used for the liquid-gated sweeps in (b), (d) and (f). Gate current (leakage current) is shown with a dashed line. The source-drain voltage used for all sweeps was  $V_{ds} = 100\text{mV}$ , and 1XPBS was used as the buffer for the liquid-gated measurements here.

1. Characteristics of Pristine Carbon Nanotube & Graphene Field Effect Transistors

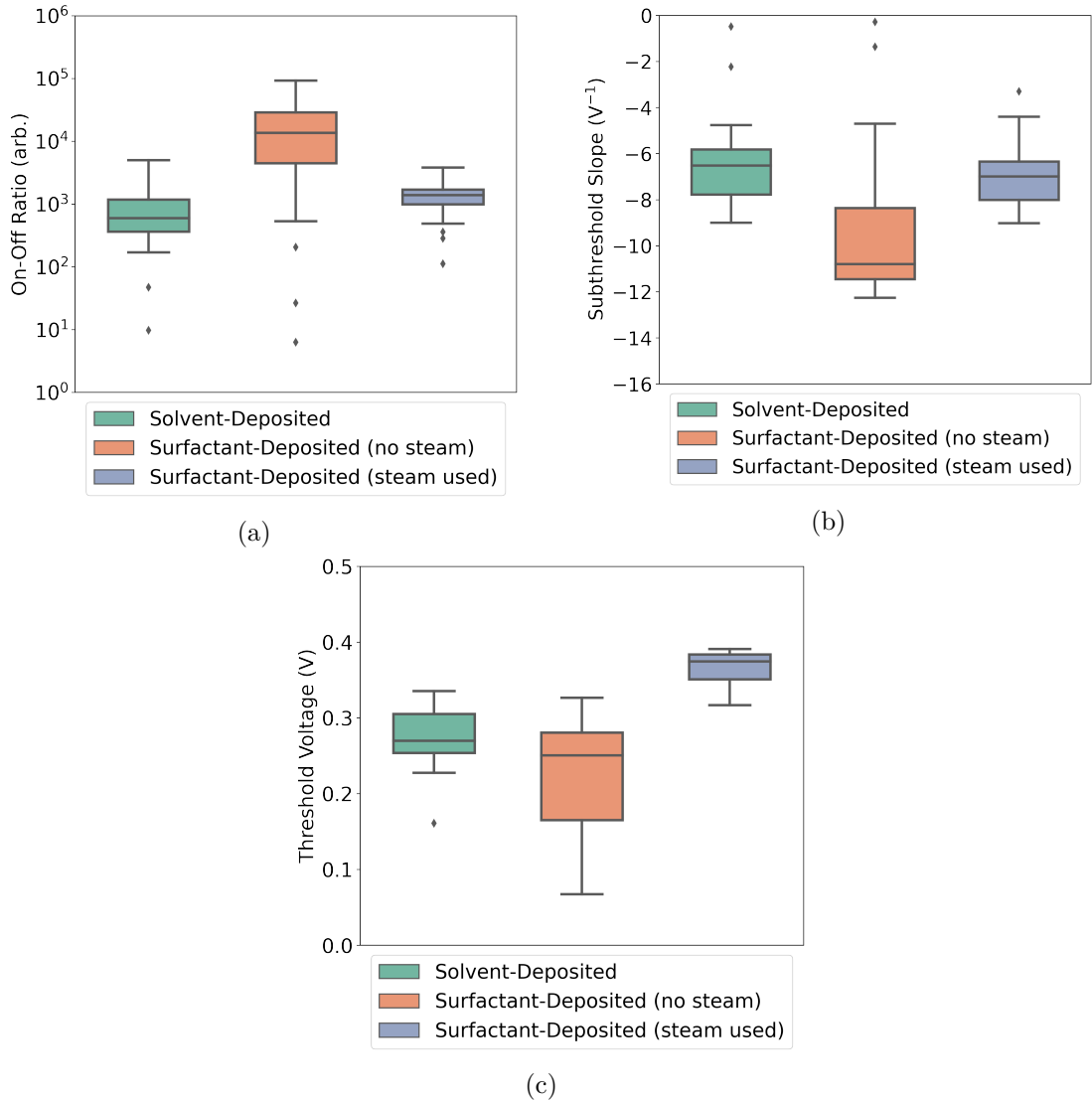


Figure 1.7.: These boxplots illustrate the statistical distribution of (a) the on-off ratio, (b) the subthreshold slope, and (c) the threshold voltage of AZ® 1518 encapsulated liquid-gated transistor channels corresponding to each type of carbon nanotube film deposition. For each deposition type, electrical characteristics were taken of 21 channels of at least three separate devices. The boxes indicate the 25th and 75th percentile of the distribution.

### 1.3. Electrical Characteristics of Pristine Devices

hysteresis. Section 1.2.1 demonstrates that the mean diameter of the bundles in these films is about 0.9 nm less than the mean bundles in films deposited without steam present, and 5.5 nm less than those in films deposited in solvent. Hysteresis is known to scale roughly linearly with bundle diameter, due to trapped charge increasing as bundle density of states is increased [32]. Steam-deposited devices also showed significantly less channel-to-channel variation in electrical characteristics more generally. Channel 1 in Figure 1.6a has a much higher off-current than the other channels of the same device, which appears to be due to a uncommonly high proportion of metallic carbon nanotubes present in the network conduction pathways of this channel [33], [34].

A summary of key parameters of pristine liquid-gated devices is shown in Figure 1.7. The full dataset consists of three sets of 21 liquid-gated transfer characteristics of working channels, with each set corresponding to the use of a particular method of carbon nanotube network deposition in the device fabrication. Measurements from at least three devices are included in each set. Each entry in the summary corresponds to the average of the specific parameter in the forward and reverse sweep direction. When steam was used for surfactant deposition of films, the resulting devices showed highly consistent channel-to-channel electrical properties. Since the carbon nanotube films on these devices are relatively dense, as seen in Figure 1.1e, the network should be well above the percolation threshold. As many carbon nanotube pathways connect across the channel in parallel, small variations in the network morphology have less of an impact on the overall channel behaviour [2]. Figure 1.3 and Table 1.2 indicate that the range of bundle sizes is relatively low in the steam-deposited films used in these devices, meaning the electrical behaviour of dominant conduction pathways is more spatially consistent. The repeatable subthreshold regime behaviour between channels seen for steam-deposited devices is a desirable attribute for reliable real-time multiplexed biosensing [27], [28], [35].

Channels from surfactant-deposited film devices usually showed a larger on-off ratio and subthreshold slope than those from solvent-deposited devices. Decreasing the ratio of gate-sensitive semiconducting carbon nanotubes to metallic nanotubes tends to decrease the on-off ratio [2], [10], [33], [34]. Section 1.2.2 seems to indicate there are more metallic nanotubes present in the surfactant-deposited films than in the solvent-deposited films. However, percolating conduction pathways dominate device behaviour and nanotube pathways across the channel with a lower degree of bundling are less likely to contain metallic tubes [2]. Therefore, the larger on-off ratio for surfactant-deposited film devices is likely a result of their reduced nanotube bundle size and reduced bundle size variation relative to other films, as discussed in Section 1.2. The larger subthreshold slope is likely due to increased mobility from a denser nanotube network in surfactant-deposited films [33], as seen in Figure 1.1e. A larger on-off ratio and subthreshold slope results in a larger change in conductance in response to changes in the transfer characteristic curve. Therefore, the larger on-off ratio and subthreshold slope of steam-deposited devices is desirable for improved sensor performance [27], [28], [35].

All channels characterised had a positive threshold voltage ( $V_{th}$ ). The threshold voltage

## 1. Characteristics of Pristine Carbon Nanotube & Graphene Field Effect Transistors

was largest and most consistent for steam-assisted surfactant-deposited films. The relatively high values of  $V_{th}$  which correspond to channel measurements from steam-assisted surfactant-deposited devices indicates increased *p*-doping of the network relative to networks deposited via alternative processes [2], [36], [37]. As seen from Figure 1.2e-f and Figure 1.4c, the steam deposition process leads to the presence of significant, persistent surfactant aggregates. It has been previously established that residual surfactant can *p*-dope carbon nanotubes, alongside enhancing *p*-doping from adsorbed oxygen and water [15], [22], [38]. The presence of residual surfactant may also explain the lowered subthreshold slope, and therefore mobility, of the steam-deposited devices relative to devices with films deposited in surfactant without steam. The analysis by Kane *et al.* shows that the thermal annealing at 150°C used in this work to remove residual surfactant is likely inadequate for this purpose. Oxidation of devices and vacuum annealing at high temperatures ( $> 600^\circ\text{C}$ ) may be required for effective desorption of the persistent surfactant [22], [39]. Devices using films made using the alternative two methods have the advantage of not requiring careful treatment to remove surfactant.

### Back-Gated CNTFETs

When characterising devices using the vapour delivery system chip carrier, the setup arrangement meant all measurements were taken using a backgate. Figure 1.6b, Figure 1.6d and Figure 1.6f show that backgated devices exhibit *p*-type transistor behaviour. Gate current leakage was negligible, as shown by the dashed line staying close to zero across the sweep. Significant hysteresis was observed. The hysteresis can be explained by the presence of defects or charge traps within and on the surface of the silicon dioxide and at interfaces between the silicon dioxide and carbon nanotubes [40]–[42]. The hysteresis observed was much greater than for the corresponding liquid-gated sweeps on the right. The devices fabricated with a solvent-based deposition were switched off at a lower voltage than the devices which used surfactant during deposition.

Transfer measurements were taken to determine whether backgated measurements could be taken of an unencapsulated device in the vapour sensor chamber with 1XPBS covering the channels. Figure 1.8 shows the behaviour of an unencapsulated backgated device with a 300 nm SiO<sub>2</sub> layer before and after being covered by 50 µL of 1XPBS (phosphate buffered saline). The on-off ratio and hysteresis of the channels increase significantly. The presence of water increases hysteresis through introducing charge traps at the silicon dioxide surface around the carbon nanotubes and at the surface of the nanotubes themselves [40], [42]–[44]. There is also a significant increase in current leakage to the backgate for larger applied voltages, despite the electrolyte having no visible physical contact with the silicon backgate or copper plane. This leakage current may simply be due to an increase in relative humidity around the device due to the presence of water [45]. As any variation in threshold voltage due to hysteresis and significant leakage current are undesirable for sensing procedures, this configuration was not used for vapour sensing purposes.

### 1.3. Electrical Characteristics of Pristine Devices

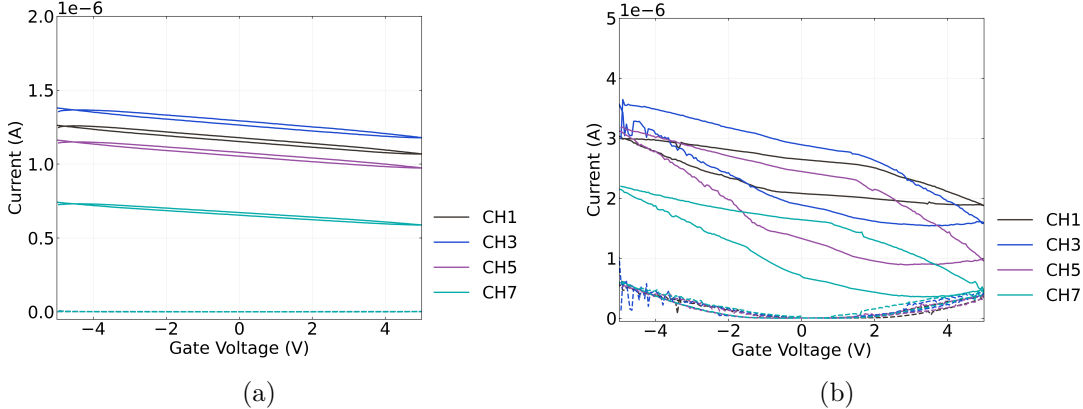


Figure 1.8.: Backgated transfer sweeps were taken of an single unencapsulated device with a 300 nm  $\text{SiO}_2$  layer and steam assisted surfactant-deposited carbon nanotube network channels before and after being covered in 50  $\mu\text{L}$  1XPBS electrolyte.

#### 1.3.3. Graphene Devices

Graphene field-effect transistor devices were electrically characterised in the manner described in [?@sec-electrical-characterisation](#) and analysed using the Python code discussed in Section B.4.

Figure 1.9 shows the liquid-gated transfer characteristics of two graphene devices. These devices were fabricated prior to Jun 2021. Both devices exhibit the ambipolar characteristics typical of liquid-gated graphene devices [46]–[49]. As with the carbon nanotube network devices, leakage current remained below  $\sim 1 \times 10^{-7}$  V across both the forward and reverse sweep. Hysteresis between the forward and reverse sweep is caused by trapping of charge within and on the surface of the  $\text{SiO}_2$  dielectric [50]. The major Dirac point for these devices is slightly to the right of  $V_{\text{Dirac}} \approx 0$  V, which indicates *p*-doping of the channel. This slight *p*-doping is likely a result of a adsorption of oxygen and water from the air and residue resist from photolithography [49], [51], [52].

Some devices exhibited a double-minima feature, indicating the presence of two Dirac points. This effect arises due to doping of graphene by the metal contacts. In shorter length channels, metal doping affects the entire channel length, leading to a consistent Fermi level and a single Dirac point. However, for longer channel lengths like ours, the doping effect from metal contact no longer reaches the entire channel, leading to a difference in Fermi level between the graphene in the channel and graphene under the metal contact. The difference in Fermi levels results in the presence of a second Dirac point [50], [53], [54]. The global minimum of the transfer characteristic can be referred to as the ‘major’ Dirac point.

Figure 1.9 also shows the effect of 1XPBS on the graphene channels. The channels

## 1. Characteristics of Pristine Carbon Nanotube & Graphene Field Effect Transistors

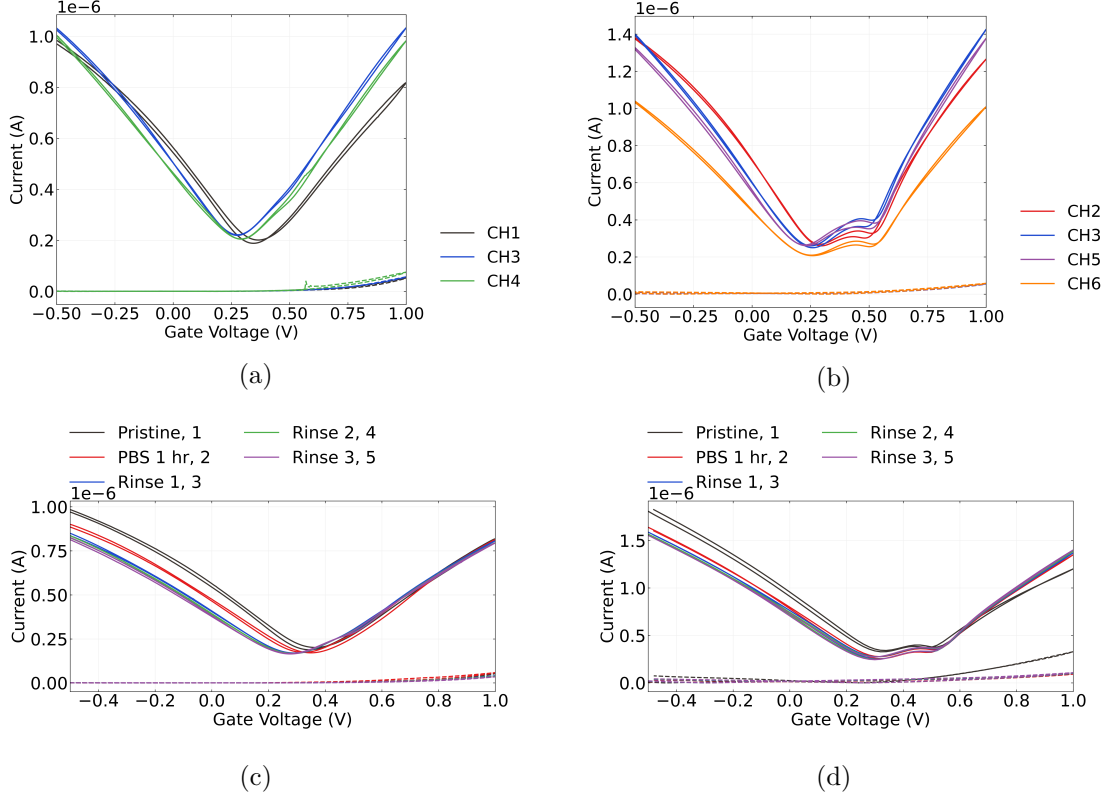


Figure 1.9.: These figures show liquid-gated transfer characteristics of channels from two AZ® 1518 encapsulated graphene devices. The characteristics of working device channels upon initial exposure to 1XPBS are shown in (a) and (b). The transfer characteristics of channel 1 in (a) and channel 5 in (b) after various degrees of exposure to 1XPBS are shown in (c) and (d) respectively, with each transfer sweep numbered in the order the sweeps were taken. The dashed lines correspond to measurements of gate leakage current.

#### 1.4. Aqueous Sensing of Phosphate Buffered Saline Concentration

were measured on exposure to 1XPBS, after exposure to 1XPBS for one hour, and after the device surface was rinsed and 1XPBS was replaced in the well one time, two times and three times successively. A slight negative shift of the major Dirac point was observed. This effect is possibly a result of gate bias stress, where successive transfer sweeps introduce charge traps to the graphene layer and alters the current level at a given gate voltage [55], [56]. Alternatively, Kireev *et al.* found that a series of liquid-gated sweeps also reduced the size of the second Dirac point, and suggested that it indicated the gate current was removing atmospheric contaminants from the graphene surface via current annealing [49]. This could be explained as the removal of contaminants causing improved contact between the metal and graphene surface, and thus increasing metal doping and consistency of the Fermi level across the channel. If the contaminants removed are *p*-dopants, then this effect could also explain the negative shift of the major Dirac point.

Table 1.3.: Average on-off ratio and major Dirac point voltage for AZ® 1518 encapsulated liquid-gated graphene transistor channels at various stages of exposure to 1XPBS. Electrical characteristics were taken of 6 channels total, three channels from each of two devices.

	1XPBS: Initial	1XPBS: After 1 hr	1XPBS: Rinse
On-Off Ratio (arb.)	$5.1 \pm 0.3$	$5.0 \pm 0.7$	$5.0 \pm 0.6$
Dirac Point Voltage (V)	$0.28 \pm 0.04$	$0.31 \pm 0.03$	$0.28 \pm 0.02$

Table 1.3 shows the on-off ratio and major Dirac point voltage of the graphene devices. Apart from the previously-mentioned slight negative shift of the major Dirac point, these values were highly consistent before and after exposure to 1XPBS.

#### 1.4. Aqueous Sensing of Phosphate Buffered Saline Concentration

##### 1.4.1. Control Series and Baseline Drift

Table 1.4.: The threshold voltages  $V_{th}$  of each working channel of a steam-deposited device, and the difference between each  $V_{th}$  and the mean device threshold voltage  $V_{th,mean}$ .

Channels	CH1	CH2	CH3	CH5	CH6	CH7
Threshold voltage (mV)	160	150	130	140	180	140
Relative to mean (mV)	10	0	-20	-10	30	-10

## 1. Characteristics of Pristine Carbon Nanotube & Graphene Field Effect Transistors

To verify the sensitivity of the fabricated field-effect transistors and therefore verify their suitability for sensing, control measurements replicating a typical sensing experiment were taken before functionalising the channels of a carbon nanotube network device. The first step to verifying device suitability was ensuring the device showed no response to 1XPBS. This sequence is referred to in this thesis as the ‘PBS control series’. The PDMS well contained 80  $\mu\text{L}$  1X PBS at 0 s. The PBS control series ran over the first 1800 s, with 20  $\mu\text{L}$  phosphate buffer saline (1XPBS) additions at 100 s, 200 s and 300 s, and 20  $\mu\text{L}$  subtractions at 400 s, 500 s and 600 s. The device was left untouched over the next 1200 s to allow the current level to settle. The gate voltage was held at  $V_g = 0 \text{ V}$ .

Figure 1.10a shows the transfer sweeps of the six working channels of a steam-assisted surfactant-deposited carbon nanotube field-effect transistor measured using the NI PXIe. The device was fabricated on a substrate with a 300 nm  $\text{SiO}_2$  layer, the carbon nanotube film was deposited using the steam-assisted surfactant method and encapsulated with AZ® 1518 before measurement. The central feature in the transfer characteristics of channels 1 and 7 are absolute-value measurements of negative current. These are unphysical measurements due to equipment error, and can be considered as regions where zero current passes through the channel. The threshold voltages of the channels are shown in Table 1.4. Table 1.4 also shows the difference between the threshold voltage of each channel and the mean threshold voltage of the device. The mean threshold voltage was  $V_{th} = 150 \pm 20 \text{ mV}$ . As discussed previously, the electrical characteristics are highly consistent between the channels due to the film deposition method used.

Figure 1.10b shows the PBS control series corresponding to each device channel alongside gate current. In both series, there is no clear stepwise response to any addition or subtraction of 1XPBS. Gate leakage current remains negligible across the entire control series, with no change in response to 1XPBS additions. The current has a period of short-term decay followed by much longer term baseline drift, similar to observations by Lin *et al.* and more recently Noyce *et al.* for parallel arrangements of single carbon nanotubes in air or vacuum [56], [57]. This effect results from changes in the occupancy of charge traps in and around the substrate and carbon nanotubes. The magnitude of baseline drift is lower for our devices than for those characterised by Noyce *et al.*, which may be a result of numerous device and setup differences which affect the presence of charge traps. These differences include liquid-gating instead of back-gated, the use of a network of carbon nanotubes instead of single nanotubes, a different channel length, the use of a 300 nm instead of 90 nm  $\text{SiO}_2$  layer, and the use of an asymmetric, liquid-gated transfer sweep over a shorter voltage range to characterise devices before each control series was measured [56].

#### 1.4. Aqueous Sensing of Phosphate Buffered Saline Concentration

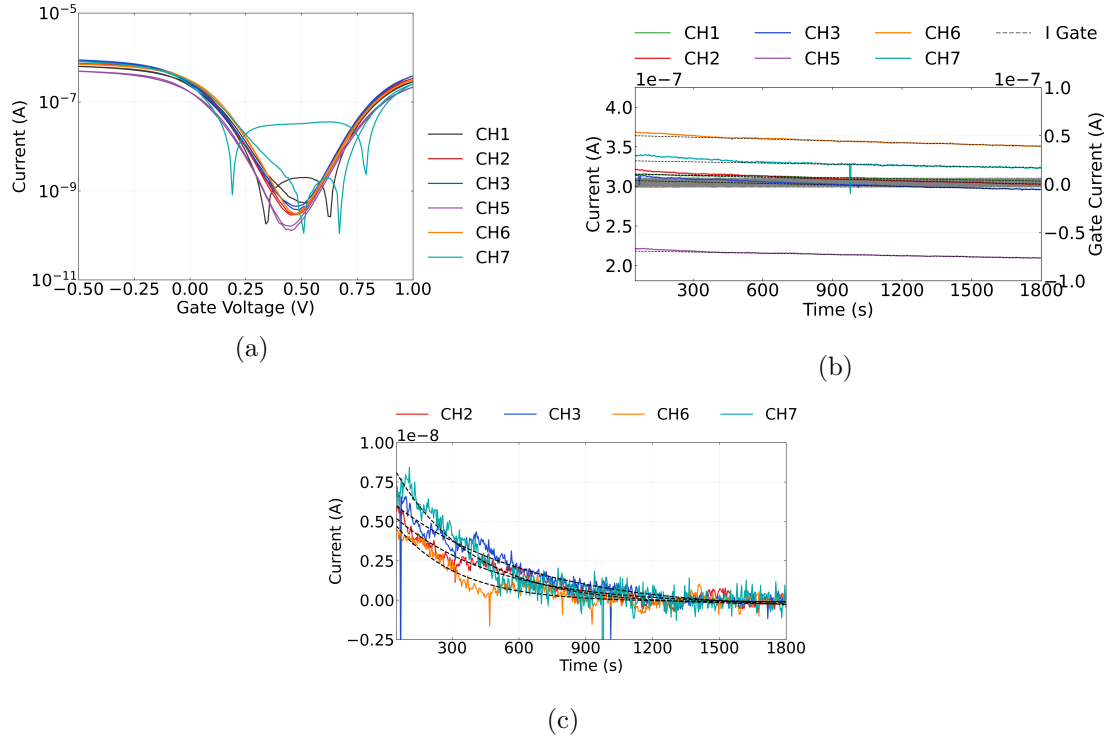


Figure 1.10.: The transfer characteristics in (a) were taken of the steam-deposited carbon nanotube field-effect transistor used here for an example of salt concentration sensing. The absolute values of measurements are shown, so that negative values resulting from measurement error can be visualised. Linear fits to the PBS control series from each channel from 1200 s onwards are shown in (b), while exponential fits to the PBS control series from 0 – 1200 with the linear fit subtracted are shown in (c). No significant response to PBS additions are seen at any of the addition times from 100 – 600 s.

## 1. Characteristics of Pristine Carbon Nanotube & Graphene Field Effect Transistors

Table 1.5.: The coefficients of linear fits to the PBS control series of each channel between 1200 – 1800 s, where  $c_1$  is the gradient and  $c_2$  is the constant term.

Channels	CH1	CH2	CH3	CH5	CH6	CH7
$c_1$ (pA/s)	-5.1±0.2	-7.2±0.1	-6.5±0.1	-5.0±0.1	-7.6±0.1	-5.1±0.2
$c_2$ ( $\mu$ A)	0.316	0.316	0.308	0.218	0.364	0.332

Table 1.6.: The coefficients of exponential fits to the PBS control series of each channel between 0 – 1200 s, after the linear fit has been subtracted, where  $I_0$  is the gradient and  $\tau$  is the time constant.

Channels	CH2	CH3	CH6	CH7
$I_0$ (nA)	6.07 ± 0.08	7.19 ± 0.11	5.75 ± 0.12	9.68 ± 0.41
$\tau$ (s)	450 ± 10	610 ± 30	280 ± 10	350 ± 30

As a first-order approximation to the longer time constant exponentials discussed by Noyce *et al.* [56], linear fits were performed on each PBS control series from 1200 – 1800 s. These fits are tangent to the curve of the sum of the larger time constant exponentials, and are a close approximation to this curve when higher order terms in the series expansion are approximately zero. This is only the case when  $t \ll \tau_i$ , where the time interval of interest  $t$  is much shorter than the time constants of the larger time constant exponentials,  $\tau_i$ . These linear fits are shown by the dashed yellow lines in Figure 1.10b. The parameters from each fit in Figure 1.10b are shown in Table 1.5, where  $I = c_1 t + c_2$ . The fits for channels 1, 5 and 7 are all in parallel within error. The gradient value for each fit in Figure 1.10b is consistent within a 2.6 pA/s range across all channels. The current data from channel 1 is closely approximated by the linear across the entire control series. No short-term decay is present for this channel, indicating the channel has low net trapped charge. It is unclear why this short-term exponential decay behaviour is only absent for channel 1.

The long-term linear fits were next subtracted from the raw control series data. Figure 1.10c shows exponential fits to the remaining curve from 0 – 1800 s, which was successful for all channels except channels 1 and 5. The parameters from each fit are shown in Table 1.6, where  $I = I_0 \exp(-t/\tau)$ . Any constant term  $I_C$  resulting from the fit was negligible and so could be neglected. The exponential fits had characteristic time constants  $\tau$  ranging between 280 – 610 s. Note that the value of peak-to-peak noise is above 5% of the initial current value for all channels. This result indicates that 3 time constants is a sufficient length of time for this short-term baseline drift to decay almost completely for each channels. At most,  $1830 \pm 150$  s is required to minimise the drift

#### 1.4. Aqueous Sensing of Phosphate Buffered Saline Concentration

present when sensing is performed, which is fulfilled by the chosen length of the control series.

From this analysis it appears that the baseline drift for the liquid-gated carbon nanotube devices can generally be approximated as a combination of a exponential and linear term. The lack of response to 1XPBS at any of the six PBS addition and removal times gives us confidence that this is a stable baseline which can be used for reliable chemical sensing. Furthermore, after  $\sim 1800$  s the baseline drift can be reasonably approximated as linear, with a small gradient of less than -10 pA/s. The approximately linear current change means that it becomes easier to distinguish responses due to analyte addition. It can therefore be concluded that the 1800 s length of the PBS control series is appropriate for minimising baseline drift for more reliable sensing.

##### 1.4.2. Sensing Series

A salt concentration sensing series were performed from 1800 s onwards, directly after the PBS control series. The responses to successive dilutions of the liquid-gate electrolyte were recorded to confirm the fabricated devices were sensitive to small environmental changes in their pristine state, to check for spurious signals, and to ensure gate current leakage or other confounding factors were not contributing to sensing responses. The PDMS well contained 80  $\mu$ L 1X PBS at 1800 s. During the series, successive additions of deionised water were made to reduce the concentration of PBS in the well. An initial 1X PBS addition was performed at 2100s, to confirm no changes occurred during the PBS control series that would interfere with sensing. All additions to the well in the sensing series and resulting changes to the PBS concentration in the well are shown in Table 1.7.

Table 1.7.: This table shows the times at which 20  $\mu$ L additions were made to the PDMS well, with 300 s between each addition. The concentration in the well after each addition and the change in concentration after each addition are also shown. The well contained 80  $\mu$ L of 1X PBS at 1800 s.

	1X PBS Addition	DI Water Additions				
Time (s)	2100	2400	2700	3000	3300	3600
Final PBS volume ( $\mu$ L)	100	120	140	160	180	200
Final PBS concentration	1X	0.83X	0.71X	0.63X	0.56X	0.50X
$\Delta$ PBS concentration	0	-0.17X	-0.12X	-0.09X	-0.07X	-0.06X

Figure 1.11a shows a multiplexed salt concentration sensing series from the channels of a single AZ® 1518 encapsulated device, measured with the NI-PXIe. The gate voltage used was 0 V, which meant current measurements were well above the magnitude of

## 1. Characteristics of Pristine Carbon Nanotube & Graphene Field Effect Transistors

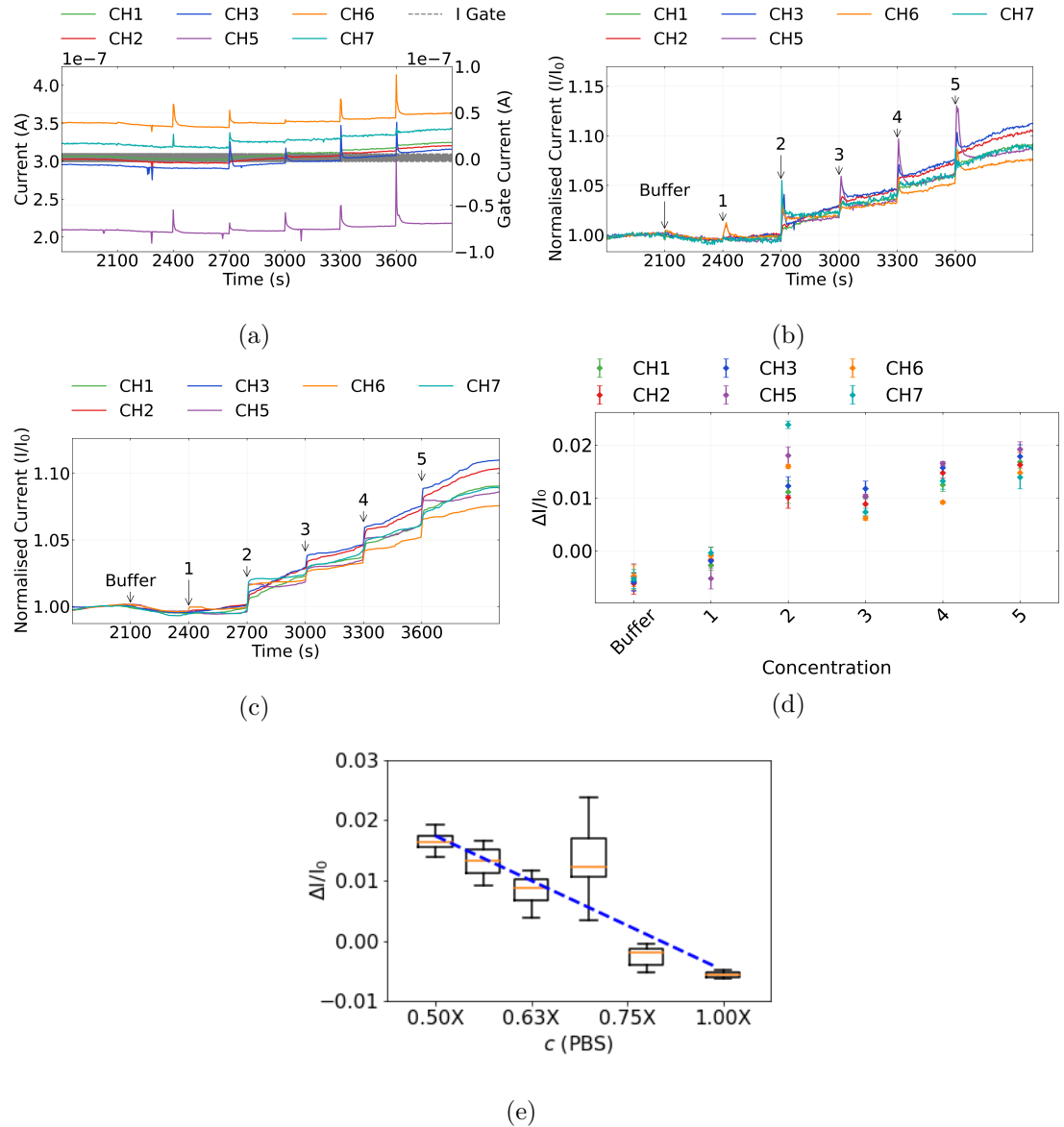


Figure 1.11.: Various visualisations of a multiplexed salt concentration sensing series taken from a single device. The source-drain voltage  $V_{ds}$  was 100 mV, and gate voltage  $V_g$  was 0 V. In (a), the raw current measurements for each channel are shown alongside gate current. The same measurements after despiking, removal of baseline drift and normalisation to initial current are shown in (b), (c) shows the data in (b) after being processed with a moving median filter, and (d) shows the signal changes in (c). The signal data in (d) is shown in box plot format in (e) alongside a fit to the median change in signal for each addition. The R squared value for the fit was 0.86.

#### 1.4. Aqueous Sensing of Phosphate Buffered Saline Concentration

the subthreshold device current. Gate current measurements did not exceed 1 nA for the SU8 encapsulated devices, and did not exceed 10 nA for the AZ® 1518 devices. At each of the deionised water addition times, the current traces for at least two out of six channels showed a sharp, transient increase in current followed by a return to an increased baseline. It is well established that changing the salt concentration of the liquid gate has an electrostatic gating effect on the carbon nanotubes or graphene, and changes the transfer characteristics of the channel. This shift in transfer characteristic leads to a real-time signal response to each addition [28], [47], [49].

Using the data in Table 1.5, the linear term approximating baseline drift ( $c_1 t$ ) for each channel can be subtracted from the data in Figure 1.11a to account for the downward drift. The mean current level just before 1800 s then becomes roughly constant. Next, each channel is normalised relative to their initial mean current level  $I_0$ . Artifacts resulting from PXIE-2737 module lag, single datapoints which fall well below the current level of the immediately preceding and succeeding datapoints, are also removed. This ‘despike’ process uses an interquartile range filter, which is described in Section 1.3.1. The resulting dataset is shown in Figure 1.11b. This figure shows that the signal-to-noise ratio remains roughly similar across all channels of the device. However, the behaviour of the initial transient increase with each addition is highly variable across channels and between additions for a single channel.

As measurement of the highly variable initial transient is not useful for robust sensing purposes, a moving median filter was applied, with the implementation of this filter discussed in Section 1.3.1. The filtered data is shown in Figure 1.11c. Noise and initial transients are removed completely, while the clearly defined step to a new current baseline is retained. Using the realtime data in Figure 1.11c, a plot of signal against addition can be created using the method described in Section 1.3.1, shown in Figure 1.11d. This presentation of the data allows us to see the increase at each step relative to  $I_0$ .

Intriguingly, even though the largest change in PBS concentration occurred at the first deionised water addition (see Table 1.7), there was very little signal change across all channels, while a relatively large change occurred at the second addition. The logarithm of final salt concentration has previously been shown to be proportional to conductance change in the linear on-regime [47]. Figure 1.11e shows the signal change presented in terms of this logarithmic relationship. The median values of the first two additions do not line up well with the overall logarithmic trend; insufficient mixing in the tightly enclosed PDMS well environment for the first few additions may be responsible for this result. Subsequent additions may improve mixing in the well, leading to the change in concentration at the surface of the channel being more representative of the overall concentration in the well.

In Figure 1.11b and Figure 1.11c, from around the second deionised water addition onwards, the drift behaviours of individual channels begin to significantly diverge. This deviation from the baseline drift subtracted from the raw data occurs either because the linear fit is only a first-order approximation which weakens with time, or because the additions themselves affect the drift behaviour. Displaying the data as discrete signal

## 1. Characteristics of Pristine Carbon Nanotube & Graphene Field Effect Transistors

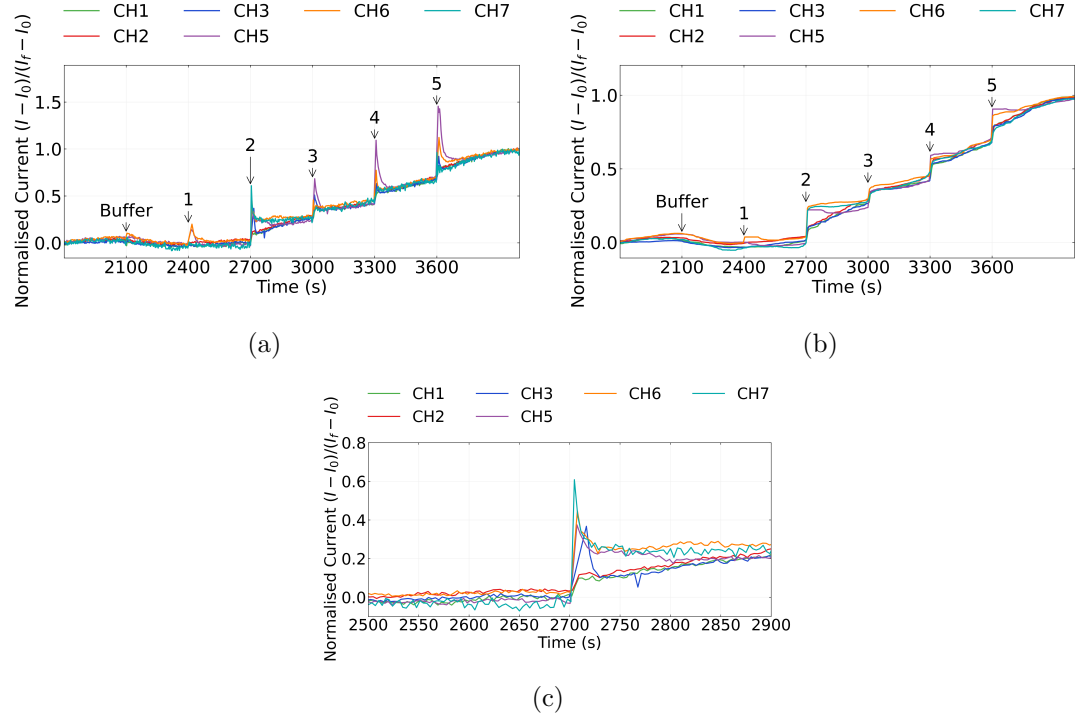


Figure 1.12.: The processed data shown in Figure 1.11b and Figure 1.11c is normalised to  $I_0$ , but an alternative normalisation can more effectively filter out remaining drift present. This normalisation presents data relative to both  $I_0$  and the final current reading  $I_f$  using the formula  $(I - I_0)/(I_f - I_0)$ . Using this normalisation, the data in Figure 1.11b and Figure 1.11c can be displayed instead as (a) and (b) respectively. (c) shows a magnified version of the step at addition 2 in (a).

#### 1.4. Aqueous Sensing of Phosphate Buffered Saline Concentration

changes, as in Figure 1.11d, is one way of excluding these deviations (see Section 1.3.1). An alternative way of presenting the signal changes, by normalising relative to both  $I_0$  and the final current reading with the formula  $(I - I_0)/(I_f - I_0)$ , is shown in Figure 1.12. This approach is useful for filtering out remaining unaccounted-for drift behaviour in order to compare the short-term transient responses to additions across the device channels. Furthermore, it lets us better understand how the short-term transient responses affect the longer-term step responses discussed earlier.

Figure 1.12a and Figure 1.12c show that the transient responses to DI water additions vary significantly across the surface of the device. For example, Figure 1.12c shows that in response to the second DI water addition, channel 7 gives a large initial transient response about twice the size of the step increase between 2600 and 2800 s. Meanwhile, channels 1 and 2 show no transient response above the step increase. Figure 1.12c indicates transient size is based on location across the device, with neighbouring channels showing the most similar behaviour. This spatially-dependent behaviour may indicate transient responses are determined by the location of the channel relative to either the location of water additions or the slightly-variable location of the liquid gate. Larger and longer-lasting transient responses are not entirely removed by the moving median filter, as shown by comparing Figure 1.12a to Figure 1.11c, and so careful placement of additions is important when sensing to minimise this effect. However, even the longest-lasting transients appear to decay to zero within about 200 s, demonstrating that a 200 s spacing between additions at minimum is necessary for reliable real-time liquid-gated sensing using this setup.

#### Signal-to-Noise Ratio

To understand the effect of gate voltages on signal-to-noise ratio, two PBS control and salt concentration sensing series were performed with the same channel at different gate voltages. The transfer characteristics of this channel are shown in Figure 1.13a, with coloured dashed lines marking the voltages used for gating the transistor during each sensing series. Figure 1.13 shows the initial PBS and DI water additions made after 1800 s. Previous work on the signal-to-noise ratio for liquid-gated, encapsulated carbon nanotube devices suggests that gating devices close to  $V_{gap}$  should give the largest signal-to-noise ratio for salt concentration additions [28]. However, this was not what was observed for our carbon nanotube field-effect transistor, as Figure 1.13 shows improved signal-to-noise ratio, i.e. the signal step can be more clearly distinguished, when gated at a voltage further removed from  $V_{gap}$ . This discrepancy could be a result of the use of a network of carbon nanotubes rather than a single nanotube; gating may have less of an impact on noise when a network morphology is used. Alternatively, it could be a result of a lack of mixing in our static well setup leading to inconsistent signal sizes with concentration change. Heller *et al.* used a flow cell during their signal-to-ratio work [28]. By using a flow cell with our devices, it would be possible to confirm whether this

## 1. Characteristics of Pristine Carbon Nanotube & Graphene Field Effect Transistors

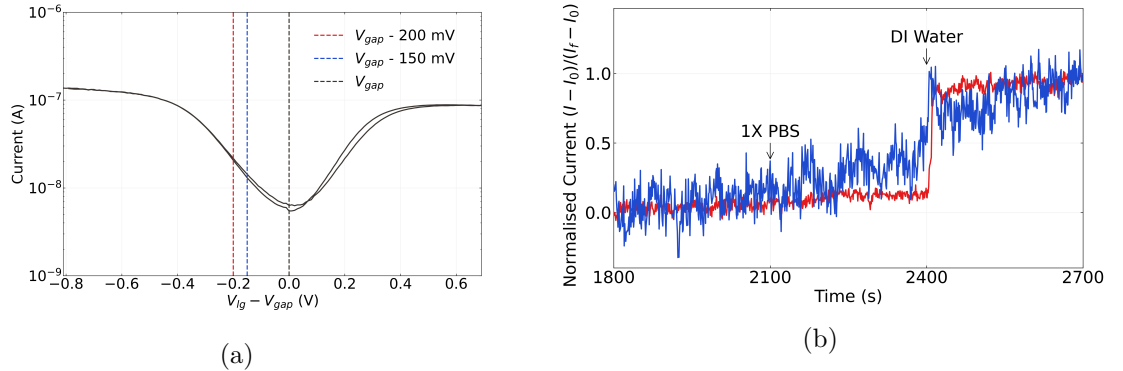


Figure 1.13.: The transfer characteristics of a single steam-deposited carbon nanotube field-effect transistor channel are shown in (a).  $V_{gap}$  is the gate voltage corresponding to the center of the transistor bandgap, found at the minimum of the characteristic curve. The signal-to-noise ratio of the channel response to a deionised water addition after a suitable control series is shown in (b). The blue current trace in (b) was performed gating the device 150 mV away from  $V_{gap}$ , while the red current was performed gating the device 200 mV away from  $V_{gap}$ .

is the case, and this might also help us reduce the size of unwanted transient responses resulting from drop-wise additions.

## 1.5. Vapour Sensing with Ethyl Hexanoate

### 1.5.1. Baseline Drift

When sensing vapour in the vapour delivery system, devices have no liquid gate and are instead backgated when taking measurements. Therefore, the baseline drift of devices characterised in this manner should be considered separately to those characterised in an liquid-gated environment. Device baseline drift of a backgated device in the vapour sensing chamber is therefore examined here in more detail. A AZ® 1518 encapsulated carbon nanotube network device was used in this discussion. The device was fabricated on a substrate with a 300 nm SiO<sub>2</sub> layer, and the carbon nanotube film was deposited using the steam-assisted surfactant method. Before measurements were taken, the vapour system was purged of vapour, the total dilution flow into the chamber was set at 200 sccm as read by the Tylan mass flow controller and flow to the PID was set to 150 sccm on the flowmeter. The transfer sweep of a channel on this device (channel 6) is shown in Figure 1.14, measured using the B1500A semiconductor device analyser.

Figure 1.15 (a) shows 3600 s of baseline drift from the same channel when the device was backgated at  $V_g = 0$  V and a source-drain voltage of  $V_{ds} = 100$  mV was placed

### 1.5. Vapour Sensing with Ethyl Hexanoate

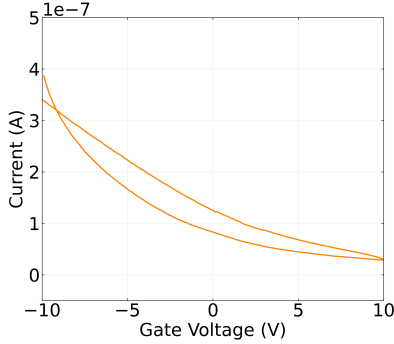


Figure 1.14.: Transfer sweep of a steam-deposited carbon nanotube network field-effect transistor, backgated in the vapour delivery system device chamber.

across the channel. During this period of time, a 200 sccm nitrogen flow was placed through the device chamber with the dilution mass flow controller. Gate leakage current remains negligible across the entire control series. As seen for the liquid-gated device in Section 1.4.1, there is a period of rapidly-disappearing exponential decay followed by a period of stable, approximately linear baseline drift. The baseline drift observed here appears to be significantly lower than that seen by Noyce *et al.* [56]. This observation suggests that the higher magnitude of drift observed by Noyce *et al.* is not a result of backgating in air, as previously suggested, but instead due to the use of a significantly different fabrication process for their devices.

A linear least-squares fit was performed on the samples taken between 2400 s – 3600 s, and the fit obtained had an R-squared value of 0.998. The constants obtained for the linear fit, where  $I = c_1 t + c_2$ , were  $c_1 = -17.31 \pm 0.05 \text{ pAs}^{-1}$  and  $c_2 = 0.779 \mu\text{A}$ . Both linear and constant terms are higher than that of the average liquid-gated device drift. The linear fit was then subtracted from the raw data, and an exponential least-squares fit was performed on the remaining dataset. Figure 1.15 (b) shows the exponential fit to this remaining dataset from 0 s – 3600 s. The constants obtained for the exponential fit  $I = I_0 \exp(-t/\tau)$  were  $I_0 = 7.20 \pm 0.05 \text{ nA}$  and  $\tau = 730 \pm 10 \text{ s}$ . The exponential term is similar in size to those found for the channels of the liquid-gated device, which may indicate the magnitude of this decay behaviour is independent of the type of transistor gating. Three time constants equates to  $2190 \pm 30$ , indicating the length of the control sequence could be safely reduced to 2400 s without the short-term exponential drift being present during sensing.

This analysis indicates that the baseline drift for the backgated carbon nanotube under nitrogen flow can be approximated as a combination of a exponential, linear and constant term. Furthermore, while only measured here for a single channel, it appears likely that we can expect backgated baseline drift behaviour to be similar to the multiplexed liquid-gated drifts observed in Section 1.4.1, except possibly with a longer time constant for the exponential term. It seems that the baseline drift behaviour in these devices is primarily due to the general nature of the carbon nanotube network. It appears possible

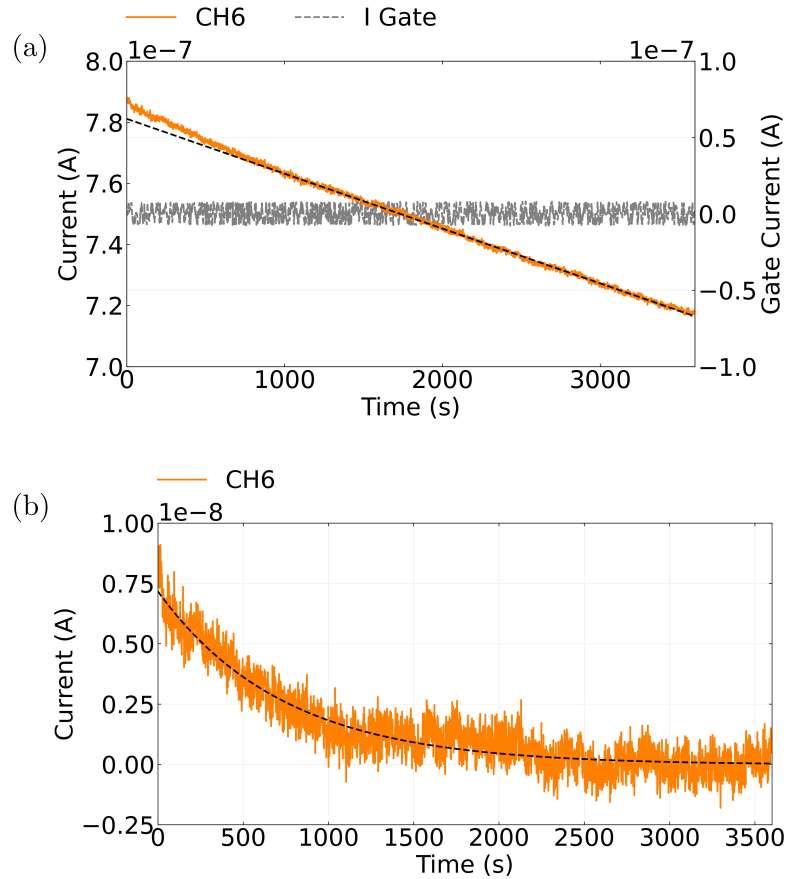


Figure 1.15.: The source-drain and gate current measured for a backgated device channel across 3600 s, where  $V_{ds} = 100$  mV and  $V_g = 0$  V is shown in (a). A linear fit to the data from 2400 s onwards has been indicated on (a) with a black dashed line. The linear fit has then been subtracted from (a) to give the dataset shown in (b). An exponential fit to the dataset in (b) is also shown in black.

that the type of gating used for device characterisation may affect the rate at which the exponential term decays. However, further experimentation may be needed to confirm this relationship, which is outside the scope of this thesis.

### 1.5.2. Sensing Series

Directly after the 3600 s control series, the device was exposed to four intervals of ethyl hexanoate vapour flow from the carrier line. 5 mL of ethyl hexanoate was placed into the analyte bottle on the carrier line before testing for the sensing series. The same settings for the vapour delivery system were kept from Section 1.5.1. A total flow of 200 sccm between the two mass flow controllers was kept through the chamber at all times. During each interval 150 sccm flow was placed through the carrier line. Apart for the duration of these intervals, flow through the carrier line was kept at zero. The intervals were of varying lengths to see how the carbon nanotube device responded to various concentrations of vapour in the chamber as recorded by the PID. A 1200 s recovery period was placed between each carrier flow interval, where 200 sccm flow was placed into the chamber from the dilution line. A separate test was also performed in an identical manner, except no ethyl hexanoate was placed into the analyte bottle. The chamber temperature was  $22^{\circ}\text{C} \pm 2^{\circ}\text{C}$  for all measurements.

Figure 1.16 shows the result of these interval tests, both with and without ethyl hexanoate placed in the analyte bottle. The data presented in Figure 1.16 (a) has been normalised, despiked, filtered and corrected for baseline drift in the manner described in both Section 1.3.1 and Section 1.4.2. Each interval of exposure to carrier line flow corresponds to a current increase. These increases have been labelled with the length of the corresponding interval used. When ethyl hexanoate is present in the analyte bottle on the carrier line, the response to each exposure interval is considerably larger than the response when no analyte is present. It should be noted that some response to carrier line flow is observed even when the analyte bottle is empty. This is most likely to be the result of low levels of residual analyte in the carrier line being pumped into the chamber. It appears very low levels of analyte persist in the line even after purging the system lines with a roughing pump. Concentration measurements taken using the photoionisation detector, shown in Figure 1.17, also indicate some low-level, residual vapour reaches the chamber during each interval even when the analyte bottle is left empty.

The signal response seen corresponds to a change in conductance of the exposed carbon nanotubes within the device channel. These conductance changes occur due to the molecular adsorption of ethyl hexanoate vapour onto the external and internal surfaces of the nanotubes. The vapour can dope the semiconducting carbon nanotubes in the channel, causing a shift in the channel threshold voltage, and can cause carrier scattering when adsorbed onto the metallic nanotubes present. Binding of analyte to a gas sensing material can be reversible or irreversible. In general, adsorption onto carbon nanotube sensors is irreversible. This irreversibility means after a response to analyte, readings from the sensor will not return to the original baseline within the same timescale as the

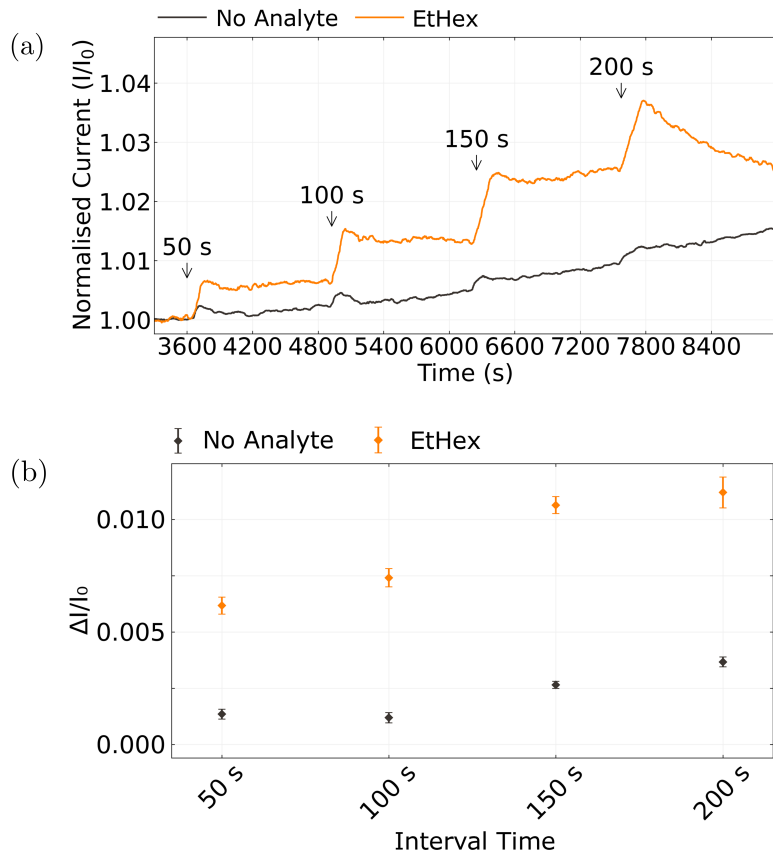


Figure 1.16.: Device channel responses to intervals of flow from the carrier line into the vapour delivery system chamber. Intervals begin at 3600 s, 4850 s, 6150 s and 7500 s. The length of each interval is indicated above the corresponding normalised current responses in (a) for both ethyl hexanoate (EtHex) and for no analyte present in the analyte bottle. The signal changes corresponding to the current responses to each interval for both ethyl hexanoate and for no analyte present are shown in (b).

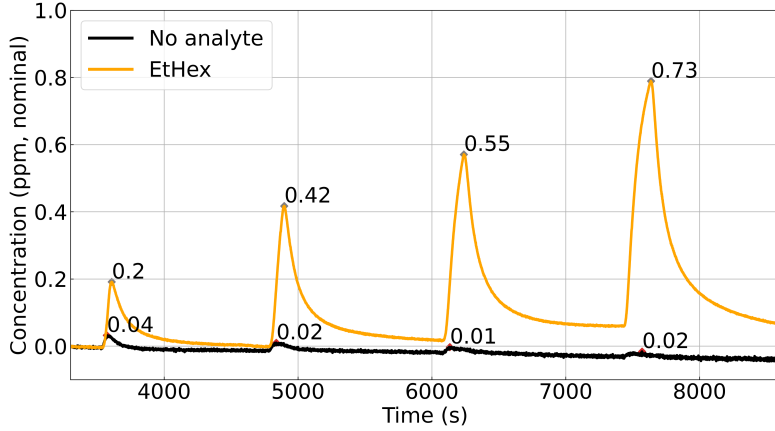


Figure 1.17.: Nominal concentration measurements by the photoionisation detector taken from the device chamber during device current sampling from 3600 s onwards, both with and without ethyl hexanoate (EtHex) in the analyte bottle. The maximum nominal concentration reached during each carrier flow interval is indicated above each peak.

sensing response, even after stopping analyte flow to the chamber [58], [59]. From Figure 1.16, it is clear that the carbon nanotube sensor configuration used here is primarily irreversible, where the current level does not return to baseline within a period of 1200 s after analyte exposure.

Assuming that the signal response is directly proportional to the degree of surface coverage by adsorbed analyte on the carbon nanotube network [59], it should be possible to model the relationship between signal response and concentration in the device chamber with an adsorption isotherm [58]. Figure 1.18 shows the maximum nominal concentration measured for every peak shown in Figure 1.17 plotted against the corresponding signal responses shown in Figure 1.16 (b). The Freundlich adsorption isotherm (Equation 1.2) models adsorption onto a heterogeneous surface.  $K_F$  is the adsorption capacity and  $1/n$  is adsorption intensity.  $1/n$  can be used to understand the heterogeneity of adsorbate sites [60], [61]. The vapour response factor is denoted as  $k_{RF}$ , which is equal to 1.6 for a 10.6 eV photoionisation detector (PID). As the PID has been run uncalibrated, a factor  $k_D$  has been included to account for linear span drift. As span drift due to window contamination can cause concentration readings to be reduced up to 30% after six months of PID operation, it is expected that  $k_D$  falls within the range of 0.2 – 1 [62], [63].

$$q_e = K_F(k_D k_{RF} C_e)^{1/n} \quad (1.2)$$

The best-fit Freundlich isotherm is shown alongside the experimental data in Figure 1.18, fitted using linear least-squares methods with an R-squared value of 0.921. The fitted isotherm had a value for  $1/n$  of  $1/n = 0.5 \pm 0.2$ . The isotherm has previously been used to model adsorption of volatile organic molecules onto single-walled carbon nanotubes.

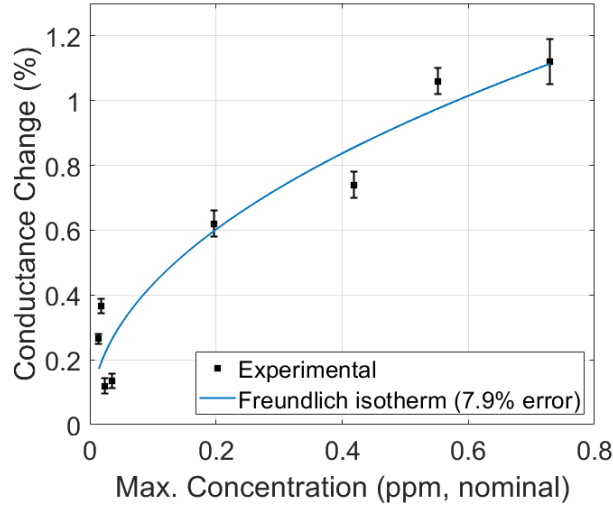


Figure 1.18.: Device response against maximum concentration measurement corresponding to each interval of carrier flow. The experimental results have been fitted with two adsorption isotherm models. The chamber temperature was  $22^{\circ}\text{C} \pm 2^{\circ}\text{C}$  across both datasets.

A value for  $1/n$  above  $\sim 0.2$  indicates the carbon nanotube network morphology of a sensor has a relatively high maximum adsorption capacity. This results from using a nanotube network morphology with a relatively high external surface area [58]. The relatively high value of  $1/n$  here indicates that the morphology used has a high external surface area and is therefore highly sensitive.

## 1.6. Conclusion

To ensure fabricated transistors were suitable for biosensing purposes, the morphology and electrical properties of the pristine carbon nanotube and graphene transistors were investigated.

The morphology of the carbon nanotube networks were found to have a significant impact on the electrical characteristics of the devices, which was determined through comparison of the skew-normal height profile of the carbon nanotube network and the key electrical parameters of a range of carbon nanotube devices. When networks were highly bundled ( $> 90\%$ ), there was a large range of carbon nanotube bundle diameters present in the network. This large variation in the size of conducting pathways resulted in a wide range of on-off ratios and threshold voltages for the liquid-gated devices created using these carbon nanotube films. In contrast, devices using films fabricated with a relatively low percentage of bundling ( $< 75\%$ ) showed highly consistent on-off ratios and threshold voltages, along with low hysteresis, due to the relatively consistent bundle

## 1.6. Conclusion

diameters and high density of these networks. These low-bundling networks were found to have a mean bundle distribution height of  $3.3 \pm 1.0$  nm. When performing multiplexed sensing, consistent channel behaviour is highly desirable since comparing sensing behaviour between channels is more straightforward.

However, atomic force microscope imaging and Raman spectroscopy also indicated that less bundled networks had the most surface contamination present. Aggregated surfactant present on the surface had a height of more than 4 nm, and introduced significant defects to the carbon nanotube network. The introduction of *p*-dopants to the carbon nanotubes by surfactant appears to have significantly increased the threshold voltage of steam-assisted surfactant-deposited network devices relative to steam-free surfactant-deposited network devices. Since the presence of surfactant could negatively impact biosensing, techniques to remove contaminants should be explored in more detail. Oxidation and thermal annealing of carbon nanotube films at high temperatures could be used to resolve this issue, and this is discussed further in **?@sec-future-work**. The presence of electrolyte on the surface of a backgated transistor for use in vapour sensing was also found to significantly adversely affect its electrical characteristics.

Constant voltage real-time measurements of the carbon nanotube field-effect transistor devices had a characteristic drift that could be modelled using a exponential and linear term. This was true for both liquid-gated and back-gated devices. The linear term of liquid-gated baseline drift had a reasonably consistent gradient between device channels, with a mean value of  $-6.1 \pm 1.2$  pAs<sup>-1</sup>, indicating that similar drift behaviour should be reproducible between devices fabricated in the same manner. The time constant of the exponential term for liquid-gated drift ranged from  $\tau = 280 \pm 10$  s to  $\tau = 610 \pm 30$  s for the device characterised. The linear term of back-gated baseline drift in nitrogen found for a single channel was  $-17.31 \pm 0.05$  pAs<sup>-1</sup>, higher than all measurements for liquid-gated linear drift. The exponential term found was  $\tau = 730 \pm 10$  s, higher than that of the liquid-gated channels. These results indicate a control series length of 1800 s is appropriate for minimising the effects of baseline drift on liquid-gated sensing, while a control series length of 2400 s is sufficient in the case of a backgated device under nitrogen flow.

A PBS dilution sensing series indicated that the carbon nanotube transistor devices were highly sensitive to environmental changes in an aqueous environment. Successive additions of deionised water to the 1XPBS present in the well gave signal responses of up to 2.5% above the control response. The signal response was found to be proportional to the logarithm of concentration, giving a fit to the median response sizes with an  $R^2 = 0.86$ . Deviations from this trend can possibly be explained by the enclosed sensing environment preventing sufficient mixing of electrolyte concentrations within the PDMS well, which could possibly be addressed by using a flow cell for sensing work. It was also seen that the signal size relative to baseline drift was highly consistent between channels. This is a promising result when it comes to ensuring consistent multiplexing, but it cannot be guaranteed that this behaviour carries over to sensing with biofunctionalised devices.

## *1. Characteristics of Pristine Carbon Nanotube & Graphene Field Effect Transistors*

Furthermore, vapour sensing with ethyl hexanoate showed that the transistor devices were responsive to vapour in a manner that corresponded to the responses from a photoionisation-based reference sensor. Exposure of the carbon nanotube device to parts-per-million concentrations of ethyl hexanoate resulted in irreversible signal responses of up to 0.8% above the corresponding control measurement. Each signal response coincided with a local maximum in chamber vapour concentration as measured by the photoionisation detector. It was found that the relationship between signal response to vapour and their corresponding maximum concentration value could be modelled using a Freundlich adsorption isotherm, where the R-squared value of the model with the dataset was 0.921. An adsorption intensity of  $1/n = 0.5 \pm 0.2$  was found for the sensor response to ethyl hexanoate, indicating that the carbon nanotube morphology used is particularly sensitive. Again, this is promising for the sensitivity of these devices when biofunctionalised, but poses potential issues in regard to the selectivity of these devices.

Graphene field-effect transistor devices were often found to possess a double-minima feature, which appears to be the result of a lack of doping from the metal contacts in the center of the device channels. These double Dirac points are unlikely to have an significant effect on the sensing behaviour of graphene devices. The graphene device characteristics were found to be consistent after 1 hour exposure to 1X PBS with minimal drift, with an on-off ratio of 5 and major Dirac point voltage of 0.3 V. There was some indications from the transfer characteristics that *p*-dopants were present on the graphene surface. Salt concentration and vapour sensing with graphene FETs is not shown in this thesis, but it is important to perform this experiment and use similar analysis techniques if there are any concerns about the sensitivity of a fabricated batch of graphene devices.

## 2. Non-Covalent Functionalisation of Carbon Nanotubes and Graphene

### 2.1. Introduction

In previous chapters, I have discussed methods of fabricating carbon nanotube and graphene devices and then shown that they are sensitive to environmental changes in a saline solution. However, for specific sensing, the devices require (bio)chemical functionalisation. Instead of responding to stimuli themselves, the sensing signal is picked up by attached receptors. The devices then act as passive transducers for the received signal. Receptors previously used with carbon nanotube and graphene devices include aptamers [4], [64]–[68] and a range of proteins [69]–[72], including animal odorant receptors [73]–[78]. A common approach to attaching receptors to the transducer involves the use of a linker molecule to tether the receptor to the transducer. Verifying that this linker molecule is bridging between the transducer and the receptor element is important for a complete understanding of the behaviour of these sensors. This verification involves providing evidence for effective attachment of linker molecule to the transducing device channel, then showing successful tethering of odorant receptors and other biomolecules to the attached linker molecule.

This chapter therefore takes some time exploring the following selection of available linker molecules for specific biosensing: 1-Pyrenebutanoic Acid N-Hydroxysuccinimide Ester (PBASE), 1-Pyrenebutyric Acid (PBA), Pyrene-PEG-NTA (PPN) and Pyrene-PEG-Biotin (PPB). The linker molecules used are discussed in detail, and numerous hurdles to successful functionalisation via linker molecules are identified and addressed. Next, it looks at verifying that the odorant receptor proteins of interest have specifically attached to these linker molecules. The experimental parameters used for both the attachment of linker molecules and receptor proteins are also varied, and the impact of these variations on successful functionalisation is investigated via Raman spectroscopy, fluorescence microscopy and electrical characterisation.

### 2.2. Non-Covalent Bonding and $\pi$ -Stacking

Linker molecules may be attached via covalent or non-covalent bonding to carbon nano-materials, such as carbon nanotubes and graphene. Covalent bonding is stronger than

## 2. Non-Covalent Functionalisation of Carbon Nanotubes and Graphene

non-covalent bonding, and therefore gives a more permanent attachment between linker molecules and the transducer. However, non-covalent bonding has the advantage of having less of an impact on the structure of a nanomaterial than covalent bonding, meaning non-covalent bonding is less likely to negatively affect the electrical properties of the transducer [9], [64], [67], [72], [79]. For example, one group found covalent bonding of diazonium linker caused a  $\sim 50\%$  drop in graphene channel mobility [69]. In comparison, only a  $\sim 5\%$  drop in mobility was seen for attachment of a mixture of linkers containing pyrene to a graphene channel via non-covalent  $\pi$  stacking [80].

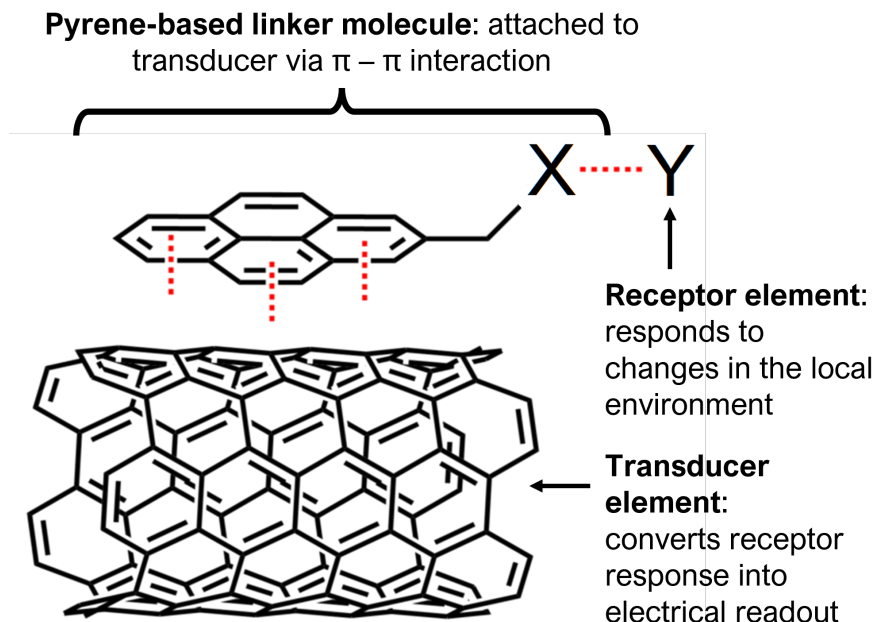


Figure 2.1.: Attachment of pyrene-based linker molecule pyrene-X and receptor Y to a carbon nanotube, representing the transducer element of a field-effect transistor. Source: Adapted from [81].

$\pi$ -stacking or  $\pi - \pi$  interaction is often used to describe a type of non-covalent bonding which occurs due to dispersion forces between unsaturated polycyclic molecules [82]. It has been argued that this label is unhelpfully specific and a misrepresentation of what can be simply classed as a type of Van Der Waals bonding [82], [83]. However, as the use of the term is widespread in the literature, it is also used here for the sake of clarity. Carbon nanotubes and graphene consist of a network of carbon atoms attached to each other by  $sp^2$  hybrid orbitals in a polycyclic structure. They are therefore able to strongly interact with linker molecules with aromatic moieties, such as pyrene [7], [67], [82]. Figure 2.1 is a visual demonstration of the relationship between the pyrene-based linker molecule with the transducer and receptor elements. A wide range of pyrene-based linker molecules have been used for non-covalent modification of carbon nanotubes and graphene [84].  $\pi$ -stacking with pyrene is the bonding mechanism underlying all the

### 2.3. Attachment of 1-Pyrenebutanoic Acid N-Hydroxysuccinimide Ester

functionalisation processes in this thesis.

## 2.3. Attachment of 1-Pyrenebutanoic Acid N-Hydroxysuccinimide Ester

### 2.3.1. Comparing Attachment Methods

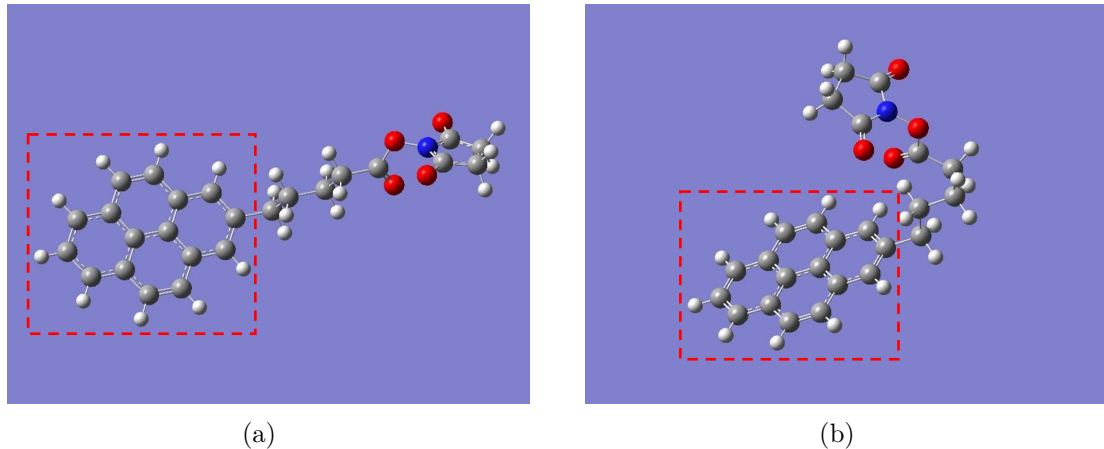


Figure 2.2.: Two conformations of PBASE molecule with geometry optimised via *ab initio* calculations performed with Gaussian 16 software [85]. White balls correspond to hydrogen, grey to carbon, red to oxygen and blue to nitrogen. The pyrene moiety is highlighted in the image with a red dashed outline.

1-pyrenebutanoic acid N-hydroxysuccinimide ester (also known commercially and in the literature both as 1-pyrenebutyric acid N-hydroxysuccinimide ester and 1-pyrenebutanoic acid succinimidyl ester; acronyms include PBASE, PBSE, PyBASE, PASE, PYSE, PSE, Pyr-NHS and PANHS) is a aromatic molecule commonly used for tethering biomolecules to the carbon rings of graphene and carbon nanotubes. Using computational modelling, two locally stable molecular conformations were found to exist, a straight (Figure 2.2a) and bent (Figure 2.2b) structure. The conformation in Figure 2.2a has a Hartree-Fock energy of -3427728.67 kJ/mol, while the conformation in Figure 2.2b has a Hartree-Fock energy of -3427729.66 kJ/mol. The difference between computed Hartree-Fock energies is 1.0 kJ/mol, small enough that the existence of both molecular conformations is physically feasible. Similar straight and bent structures have previously been modelled for PBASE attached to graphene [86].

## 2. Non-Covalent Functionalisation of Carbon Nanotubes and Graphene

Table 2.1.: Comparison of PBASE functionalisation processes used for immobilisation of proteins and aptamers onto carbon nanotubes and graphene. Experimentally optimised variables are marked with a star (\*). Blank entries indicate there was no mention of the parameter in a particular paper.

Solvent	Channel	Conc. (mM)	Incubation type	Time (hr)	Rinse steps	References
DMF	CNT	5	Immersed	1	PBS	Maehashi, 2007. [87]
		6	Immersed	1	DMF, PBS	García-Aljaro, 2010. [88]
		6	Immersed	1	DMF	Chen, 2001. [89]
		6	Immersed	1	DMF	Cella, 2010. [90]
		6	Immersed	1	DMF	Das, 2011. [91]
		6	-	2	DMF	Besteman, 2003. [92]
	Graphene	-	-	2	DMF	Tsang, 2019. [93]
		-	-	20	-	Wiedman, 2017. [94]
		0.2	Immersed	20	DMF, IPA, DI water	Gao, 2018. [95]
		1	Dropcast	6	DMF, IPA, DI water	Nekrasov, 2021. [66]
		5	Immersed	1	DMF, DI water	Hwang, 2016. [96]
		5*	Immersed	3*	DMF	Hao, 2020. [97]
2-Methoxyethanol	Graphene	5	Immersed	4*	DMF, DI water	Mishyn, 2022. [67]
		6	Dropcast	2	DMF, DI water	Nur Nasufiya, 2020. [98]
		10	Dropcast	2	DMF, DI water	Campos, 2019. [99]
		10	Immersed	2	DMF, PBS	Kuscu, 2020. [100]
		10	Immersed	1	DMF	Xu, 2017. [101]
	CNT	10	Immersed	12	DMF, EtOH, DI water	Khan, 2020. [102]
		50	Immersed	4*	MeOH	Wang, 2020. [72]
		1	Immersed	1	DI water	Ono, 2020. [103]
		1	Immersed	1	MeOH, DI water	Zheng, 2016. [104]
		1	Immersed	2	MeOH	Kim, 2009. [105]
Methanol	Graphene	100	Dropcast	1	DI water	Yoo, 2022. [78]
		5	Immersed	2	-	Sethi, 2020. [106]
		5	Immersed	1	MeOH, PBS	Ohno, 2010. [107]
	CNT	10	-	1	DI water	Lopez, 2015. [108]
		10	Immersed	1	PBS	Strack, 2013. [109]

### 2.3. Attachment of 1-Pyrenebutanoic Acid N-Hydroxysuccinimide Ester

The pyrene moiety, highlighted with a red dashed outline in Figure 2.2a-b, non-covalently bonds to the carbon rings of the carbon nanotube and graphene surface. The N-hydroxysuccinimide (NHS) ester group, seen on the right-hand side of Figure 2.2, is highly reactive with amine groups. It can undergo a nucleophilic substitution reaction with amines attached to proteins or aptamers, tethering these biomolecules via an amide or imide bond [7], [67], [89], [110].

The non-covalent functionalisation of proteins onto a single-walled carbon nanotube using PBASE was first reported by Chen *et al.* in 2001 [89]. Two successful methods for protein functionalisation and immobilisation were reported, with the only differences being the solvent used to dissolve the PBASE powder (DMF, methanol) and the final concentration of the resulting solutions (6 mM, 1 mM respectively). PBASE powder appears to dissolve poorly in methanol at higher concentrations, which might explain the use of different concentrations of PBASE in each solvent. An extensive comparison of methods used in the literature for PBASE functionalisation of carbon nanotube and graphene devices with aptamers and proteins is given in Table 2.1. Several listed works directly cite Chen *et al.* when discussing functionalisation with PBASE [90], [92], [99], [104], [107]. The other works listed do not explicitly reference Chen *et al.* in their methodology; however, the frequency of methods detailing the use of 6 mM PBASE in dimethylformamide (DMF) and 1 mM PBASE in methanol indicate that these processes are largely copying the process used by Chen *et al.*.

However, it is also apparent from Table 2.1 that there is a large degree of variation in the methods used for PBASE functionalisation. Various electrical characterisation, microscopy and spectroscopy techniques have been used to demonstrate successful functionalisation. Until recently, there has been little justification provided for the selection of variables used in the functionalisation procedure (e.g. length of time submerged in solvent containing PBASE), despite the wide-ranging use of this process in the literature [72], [111], [112]. This is surprising, given that the sensitivity of functionalised devices is considered to be closely related to the density of surface functionalisation [110], [113], [114]. Furthermore, a detailed investigation of PBASE functionalisation process variables has only been undertaken for graphene-based devices [67], [72], [97], [112].

Zhen *et al.* [112], Wang *et al.* [72] and Mishyn *et al.* [67] have all claimed that carefully tuning the surface concentration of PBASE is required to avoid multilayer coverage of the graphene surface, as this negatively impacts sensing. Mishyn *et al.* [67] used cyclic voltammetry to demonstrate that less receptor attachment to the graphene surface occurs when multiple layers of PBASE are present. However, none of these groups have presented analyte sensing results from their functionalised graphene devices. In contrast, Hao *et al.* [97] found that maximising the PBASE surface coverage of a channel resulted in more sensitive aptameric sensing, thereby reaching the opposite conclusion. The inconsistency in these recent findings mean more work is needed to understand the PBASE functionalisation process to achieve optimal biosensor sensitivity. It may also be the case that a specific functionalisation process is required for optimal sensitivity with the use of a specific type of receptor.

2. Non-Covalent Functionalisation of Carbon Nanotubes and Graphene

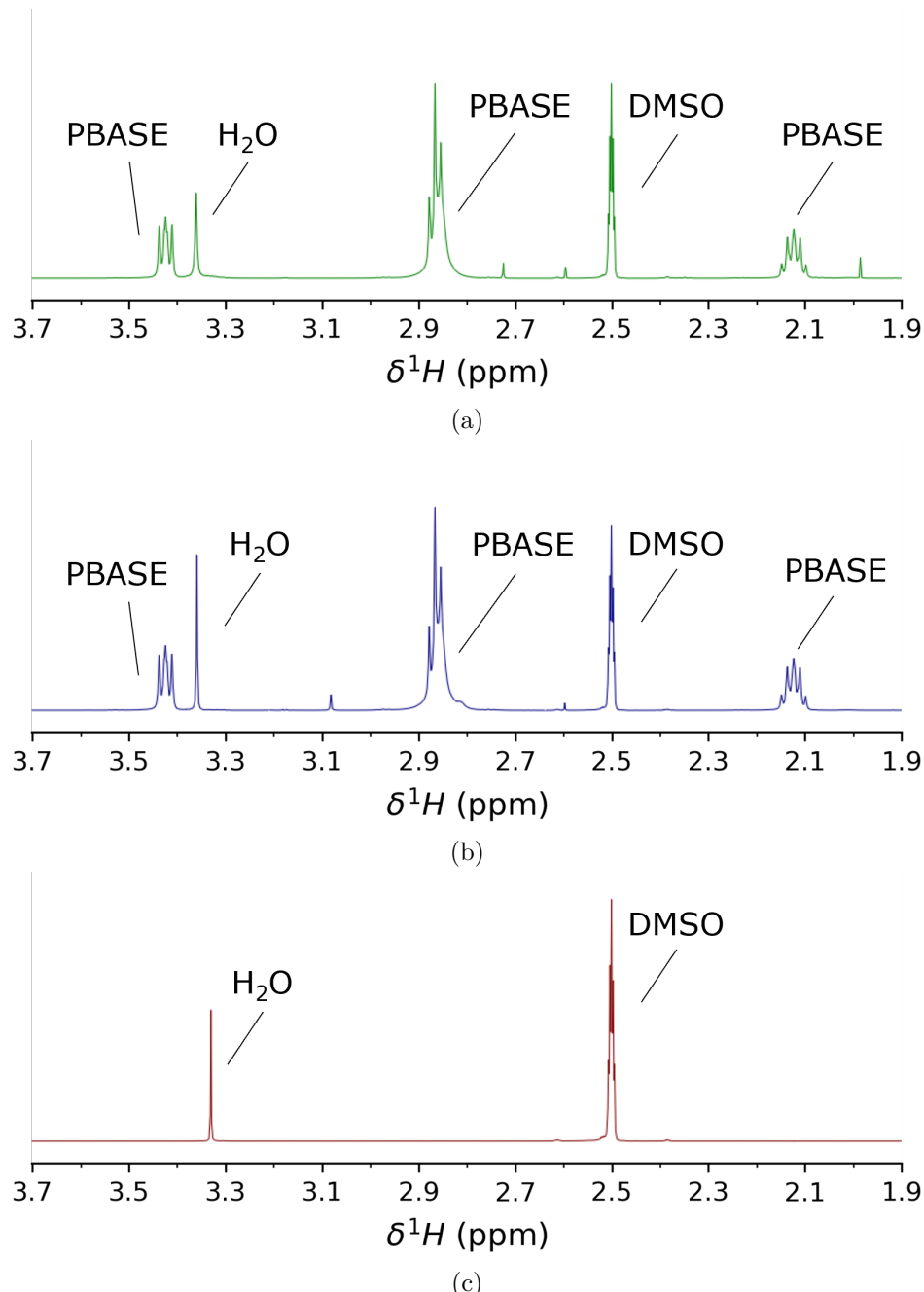


Figure 2.3.:  $^1\text{H}$  Nuclear Magnetic Resonance (NMR) spectra, performed with  $\text{DMSO-d}_6$  used as the NMR solvent. (a) and (b) show NMR spectrum for commercially purchased PBASE, from Sigma-Aldrich and Setareh Biotech respectively, while (c) shows the blank spectrum taken with only  $\text{DMSO-d}_6$  present. Spectra were taken by Jennie Ramirez-Garcia, School of Chemical and Physical Sciences, Te Herenga Waka - Victoria University of Wellington. Unlabelled peaks correspond to sample impurities.

### *2.3. Attachment of 1-Pyrenebutanoic Acid N-Hydroxysuccinimide Ester*

Once fastened to a bioreceptor via an amide or imide bond, the attachment to the linker molecule is not easily broken. However, prior to use in functionalisation processes, the NHS ester may react with any water present. This ester hydrolysis converts PBASE to its corresponding carboxylic acid, 1-pyrenebutyric acid (PBA), leaving it unavailable to react further with amine groups [67], [110], [115]. If the amine group functionalisation is performed within a  $\sim$  1 hour period, with a high concentration of bioreceptor used at close to neutral pH, competing hydrolysis should not have a significantly adverse impact on the functionalisation process [110]. However, if PBASE is exposed to water during storage over a significant length of time, the presence of 1-Ethyl-3-(3-dimethylaminopropyl)carbodiimide (EDC) can be used to restore the NHS ester and enable the substitution reaction to take place (see discussion of PBA/EDC in Section 2.4).

#### **2.3.2. Examining 1-Pyrenebutanoic Acid N-Hydroxysuccinimide Ester Purity**

I purchased PBASE from two suppliers, Sigma-Aldrich and Setareh Biotech. Sigma recommended DMF and methanol as suitable solvents for dissolving PBASE, alongside chloroform and dimethyl sulfoxide (DMSO). Setareh Biotech indicated methanol can be used for dissolving PBASE. The two suppliers had conflicting information for suitable storage of PBASE, with Sigma recommending room temperature storage while Setareh Biotech recommends storage of -5 to -30°C and protection from light and moisture. I used nuclear magnetic resonance (NMR) spectroscopy to verify the purity of PBASE from various suppliers. As water can react with PBASE to form unwanted byproducts, it appears that protection from moisture is particularly important. A particular emphasis was placed on detecting water presence in the received samples, considering the long travel time of the PBASE with uncertain storage conditions.

Figure 2.3 compares the shapes of hydrogen NMR spectra of PBASE from each supplier when dissolved in deuterated DMSO, alongside a blank deuterated DMSO spectrum. Both PBASE samples possessed characteristic chemical shift features between 2.1 – 2.2 ppm, 2.8 – 2.9 ppm, and 3.4 – 3.5 ppm. These chemical shifts roughly correspond to those seen in previous NMR spectra for PBASE [116]. The feature at 2.50 ppm represents the deuterated DMSO solvent, while the single peak between 3.3 – 3.4 ppm represents the water present in the sample. By comparing the area of these peaks, a rough estimate of the amount of water originally present in the PBASE sample can be obtained. The H<sub>2</sub>O:DMSO ratio is 1:7 in the blank spectrum, but  $\sim$  1:3 in the provided samples, possibly indicating the introduction of water to the PBASE during production or storage. However, DMSO is strongly hygroscopic and slight differences in DMSO storage time, as well as differences in humidity during sample preparation, may have had a significant impact on this result [117]. Other impurities are also seen on both PBASE spectra, though their small size indicates they make up only a small percentage of each sample. Strack *et al.* [109] recommend leaving frozen PBASE at

## 2. Non-Covalent Functionalisation of Carbon Nanotubes and Graphene

room temperature for 15 minutes before exposing it to air to prevent condensation near the PBASE, as this can cause unnecessary  $\text{H}_2\text{O}$  contamination.

### 2.3.3. Electrical Characterisation

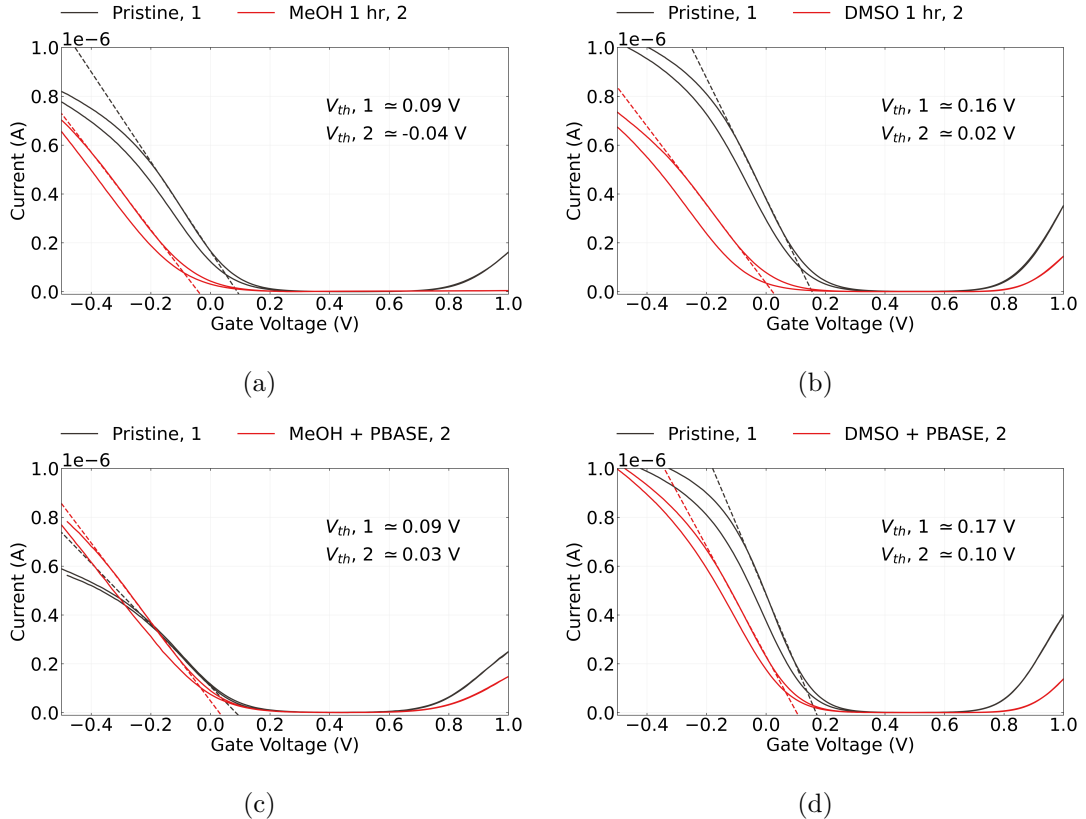


Figure 2.4.: The electrical transfer characteristics of carbon nanotube transistors ( $V_{ds} = 100 \text{ mV}$ ) before and after being submerged in methanol (a) or dimethyl sulfoxide (b) for one hour and subsequently rinsed with deionised water. The change in characteristics of similar transistor channels after being submerged in these same solvents containing 1 mM PBASE for one hour and then rinsed are shown in (c) and (d) respectively. Average threshold voltages for each transfer characteristic curve are also shown (taking the average of forward and reverse sweep values).

The electrical characteristics of the carbon nanotube or graphene transistor are often used to verify successful functionalisation and make a statement about the effect of chemical modification on the channel. However, this verification usually does not account for the effect of the solvent on the transistor channel. Figure 2.4a and Figure 2.4b show that by exposing a steam-deposited carbon nanotube network channel to solvents

### 2.3. Attachment of 1-Pyrenebutanoic Acid N-Hydroxysuccinimide Ester

commonly used in PBASE functionalisation processes (Table 2.1), such as methanol (MeOH) or dimethyl sulfoxide (DMSO), a significant negative shift in channel threshold voltage occurs even after thorough rinsing with deionised water. It appears that the carbon nanotubes have adsorbed solvent which persists even after thoroughly rinsing the device. From the shape of the change in the transfer curve, it seems the residual polar solvent molecules capacitively gate the channel [37], [118]. Besteman *et al.* reported observing a similar effect from prolonged exposure of a single carbon nanotube to dimethylformamide (DMF) [92]. Atomic force microscopy also indicates that solvent lingers after device cleaning. Figure 2.5 shows that after 1 hour exposure to DMSO, the feature height of the network is significantly increased.

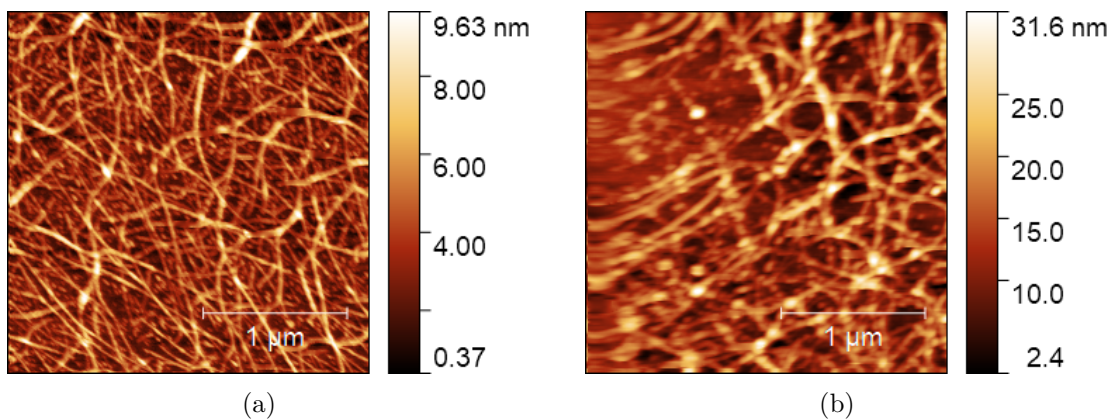


Figure 2.5.: 2.5  $\mu\text{m}$  x 2.5  $\mu\text{m}$  atomic force microscope images of a surfactant-deposited carbon nanotube film before (a) and after (b) 1 hour submersed in dimethyl sulfoxide (DMSO). Image blurring in (b) appears to be due to the presence of adsorbed DMSO.

Capacitive gating results from dense coverage of adsorbed molecules on the carbon nanotube surface which have a low permittivity relative to the surrounding electrolyte [37]. The relative permittivity of MeOH and DMSO are  $\sim 33$  [119] and  $\sim 47$  [120] respectively, which are both much lower than the relative permittivity of phosphate buffer saline,  $\sim 80$  [65]. From Figure 2.4a and Figure 2.4b, the threshold shift values found resulting from exposure to each solvent, taking the average of forward and reverse sweep values from a single device, were  $\Delta V = -0.15 \pm 0.02$  V and  $\Delta V = -0.15 \pm 0.01$  V for MeOH and DMSO respectively. The average threshold shift value for a second device exposed to MeOH was  $\Delta V = -0.16 \pm 0.02$  V, indicating that this threshold shift result is reproducible.

Using the same characterisation process as in this work, Murugathas *et al.* [75] showed that the attachment of PBASE to a solvent-deposited carbon nanotube network had little effect on channel threshold voltage, implying the presence of PBASE had not significantly influenced channel gating. Here, an average threshold voltage shift of  $-0.06 \pm 0.04$  V is seen after PBASE functionalisation in MeOH and  $-0.06 \pm 0.01$  V after PBASE

## *2. Non-Covalent Functionalisation of Carbon Nanotubes and Graphene*

functionalisation in DMSO. These threshold voltage shifts are small compared to solvent only. It is possible that the attachment of PBASE prevents solvent adsorption, and has a small negative gating effect on the channel. Alternatively, while the solvent negatively gates the channel, resulting in a threshold shift of -0.15 V, the PBASE may be counteracting this by positively gating the channel, resulting in a threshold shift of +0.09 V. Murugathas *et al.* also observed a slight increase in channel conductance after PBASE functionalisation [75]. Figure 2.4 also shows a slight increase in channel conductance post-functionalisation in both Figure 2.4c and Figure 2.4d relative to the solvent-only case in Figure 2.4a and Figure 2.4b. This result implies that the presence of PBASE molecules increases channel mobility and therefore conductance [37].

The absorption of organic solvent by the carbon nanotube network has unknown but potentially negative implications for biosensor functionalisation. Use of organic solvents in functionalisation can also attack the encapsulation layer of devices, promoting gate current leakage. In light of these issues, recent work has begun to explore alternative aqueous-based methods for functionalisation of biosensors [64]. The discussion here also illustrates the importance of considering each substance used when electrical characterising a device to verify if functionalisation has worked. The qualitative presence of a change in characteristics (or lack of one) over the full process is not sufficient to make conclusive remarks regarding successful functionalisation. A full set of electrical control measurements are required for an understanding of electronic changes occurring during the functionalisation process, in the manner of Besteman *et al.* [92].

### 2.3. Attachment of 1-Pyrenebutanoic Acid N-Hydroxysuccinimide Ester

Table 2.2.: Comparison of 1-pyrenebutanoic acid (PBA) functionalisation processes used for immobilisation of proteins, enzymes and aptamers onto carbon nanotubes and graphene. 1-ethyl-3-(3-dimethylaminopropyl) carbodiimide hydrochloride (EDC) and NHS were co-mingled in buffer/electrolyte solution or DI water in each process - some papers used N-hydroxysulfosuccinimide instead of N-hydroxysuccinimide, and both compounds are abbreviated as NHS in this table for simplicity. Device exposure times to each solution are shown next to the solution concentration. Blank entries indicate there was no mention of the parameter in a particular paper. <sup>†</sup>PEG or PEG pyrene were used to reduce non-specific binding. <sup>††</sup>Several pyrene-based linkers were compared and PBA gave an optimal functionalisation result.

Solvent	Channel	PBA (mM)	Time (hr)	EDC (mM)	NHS (mM)	Time (min)	References
DMF	Graphene	0.6	1	-	-	120	Gao, 2016 <sup>†</sup> . [121]
		5	2	2	5	30	Mishyn, 2022. [67]
	CNT	100	3	200	-	30	Min, 2012. [122]
	Graphene, CNT	7.6	2	8	20	120	Xu, 2014. [123]
DI water	CNT	-	-	32	12	Overnight	Pacios, 2012 <sup>†</sup> . [124]
Ethanol	CNT	1	1	100	100	20	Filipiak, 2018 <sup>†</sup> . [125]
Acetonitrile	Graphene	1	1	400	100	60	Tong, 2020 <sup>††</sup> . [71]
Borax	CNT	2	24	2.5	-	1080	Liu, 2011 <sup>†</sup> . [126]
DMSO	Graphene	5	1	50	50	90	Fenzl, 2017. [127]

## 2.4. Attachment of 1-Pyrenebutyric Acid

### 2.4.1. Comparing Attachment Methods

Another linker molecule that can be used to attach receptor molecules to a carbon nanotube or graphene channel is 1-pyrenebutyric acid (PBA or PyBA). As with PBASE, the pyrene group of PBA has a  $\pi$  interaction with the carbon rings of the channel surface. It is possible to react PBA with 1-ethyl-3-(3-dimethylaminopropyl) carbodiimide hydrochloride (EDC or EDAC) to form an *O*-acylisourea intermediate, which can then react with an amine group on a biomolecule and form an amide bond [128], [129]. The water solubility of EDC means that, unlike PBASE, it is possible to functionalise with EDC dissolved in water rather than in an organic solvent. However, like PBASE, EDC and the *O*-acylisourea intermediate are prone to hydrolysis, especially in acidic conditions. Therefore, like PBASE, it should be stored at  $-20^{\circ}\text{C}$ , and warmed to room temperature to prevent condensation build-up, since exposure to condensation will hydrolyse the reagent [129]. Furthermore, by adding N-Hydroxysuccinimide (NHS) or N-hydroxysulfosuccinimide (sulfo-NHS) to the reaction vessel, PBASE is formed as an active intermediate, which is less prone to hydrolysis and increases the PBA/EDC reaction yield [128]–[130].

A full comparison of functionalisation procedures used for linking carbon nanotube and graphene devices to aptamers and proteins with PBA is given in Table 2.2. To the best of my knowledge, this table is as complete a summary as possible of 1-pyrenebutyric acid functionalisation processes for carbon nanotube and graphene field-effect transistor biochemical sensors. By comparing Table 2.1 and Table 2.2, it is clear that PBASE is more widely used for non-covalent functionalisation than PBA/EDC. As was the case for PBASE, there are a wide range of process variables used for the functionalisation process, with little justification used for variables chosen. Also notable is the frequent use of polyethylene glycol (PEG) or pyrene-PEG for prevention of non-specific binding (NSB). Non-specific binding is discussed further in [?@sec-non-specific-binding](#). Despite being less widely used, Mishyn *et al.* [67] state a preference for the use of PBA/EDC over PBASE, as they found it was less prone to hydrolysis and gave a larger reaction yield when binding ferrocene to graphene. A potential downside of using PBA/EDC for protein immobilisation is that EDC has numerous ways of interacting with proteins, and not all of these are necessarily desirable; furthermore, the addition of NHS may also cause other issues, such as precipitation of the reaction compound [129]. The greater range of process variables involved in the functionalisation also adds to the complexity of reproducing past results.

### 2.4.2. Raman Spectroscopy

Raman spectroscopy was used to verify the attachment of PBA to a carbon nanotube network film with a silicon dioxide substrate in the manner outlined in [?@sec-raman-](#)

## 2.4. Attachment of 1-Pyrenebutyric Acid

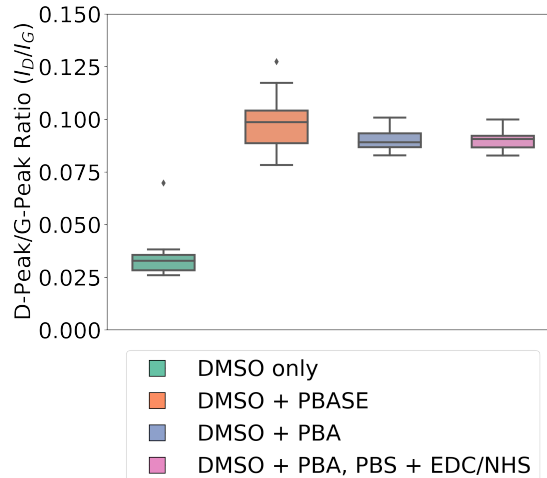


Figure 2.6.: This box plot shows the distribution of D-band peak to  $G^+$ -band peak ratio,  $I_D/I_G$ , across nine locations for a selection of chemically-modified carbon nanotube films. The D-band and G-band intensities for all samples were first normalised to the intensity peak corresponding to the silicon dioxide substrate.

**characterisation.** As highly-bundled devices were found to have less defects present prior to modification, as discussed in Section 1.2.2, solvent-deposited films were used for the verification of pyrene attachment to prevent the initial presence of defects influencing the analysis. Droplets of DMSO solution were placed on three (solvent-deposited) carbon nanotube films taken from the same wafer. The DMSO solution on one film contained 5 mM PBA, the solution on another film contained 5 mM PBASE, and the DMSO on the final film contained no linker molecule. After incubation for 1 hour, films were rinsed for 15 s with DMSO, then for 15 s with IPA to remove excess DMSO while avoiding hydrolysis of the PBASE. After the first set of Raman spectra was taken, the film initially exposed to PBA was further exposed to a solution of 20 mM EDC and 40 mM NHS in 1XPBS electrolyte for 30 minutes, and a second set of Raman spectra was taken for this film. As in Section 1.2.2, two spectra taken at each position were processed according to Section B.3, and the silicon dioxide reference peak measured in the wavenumber range  $100\text{ cm}^{-1} - 650\text{ cm}^{-1}$  was used to normalise the D-band and G-band peaks from the wavenumber range  $1300\text{ cm}^{-1} - 1650\text{ cm}^{-1}$ . The ratio between the average intensity of the D-peak and the  $G^+$ -peak at each position was calculated, and the distribution of ratio values corresponding to each modified film is shown in Figure 2.6.

There is a  $\sim 3\times$  increase in the intensity ratio  $I_D/I_G$  for both the films modified with PBASE and PBA compared to the film which was only exposed to DMSO. Previous works have found that a change in the intensity ratio indicates successful  $\pi$ -stacking on the carbon nanotube surface, as it indicates surface modification of the carbon nanotubes has occurred [131], [132]. Wei *et al.* [131] found functionalisation with PBASE altered

## 2. Non-Covalent Functionalisation of Carbon Nanotubes and Graphene

the ratio by a factor of  $\sim 1.5\times$ , while Lan *et al.* [132] found that functionalisation with PBA altered the ratio by a factor of  $\sim 0.8\times$ . The reason for the large difference between results is not immediately clear, but may result from the significant differences in the pristine composition and morphology of carbon nanotube networks used in each publication, and differences in the functionalisation method used. Across all scan locations in **?@fig-raman-comparison**, the value found for  $I_D/I_G$  is consistently  $\sim 0.095$  for both PBA and PBASE. Furthermore, subsequent Raman measurements of the PBA-modified film after further functionalisation with EDC/NHS do not show a significant change in  $I_D/I_G$ . These results indicate that presence of the NHS ester has little effect on the Raman shift. It should be clarified that Raman spectroscopy cannot be used to distinguish between the presence of PBA and PBASE on the device surface. However, it is clear that functionalisation of the carbon nanotube network with both the PBA and PBASE has led to measurable *pi*-stacking between the network and the pyrene group attached to each compound.

### 2.4.3. Electrical Characterisation

Figure 2.7 shows the transfer characteristics of a carbon nanotube transistor channel at various stages of a PBA/EDC functionalisation, where a excess of N-hydroxysuccinimide (NHS) was added alongside EDC. A solvent-deposited carbon nanotube film was used for the device. The PBA was dissolved in DMSO, and the device channels were exposed to this solution for 1 hour. The electrical change resulting from PBA exposure is shown in Figure 2.7a. The threshold shift with the addition of 5 mM PBA in DMSO for 1 hour is equivalent to the shift seen when only DMSO is added,  $\Delta V = -0.15$  V. The lack of a significant threshold shift directly attributable to the PBA is a result of pyrene having a neutral charge state; any contributions from the charged carboxyl group are screened from the carbon nanotube sidewalls by surrounding water molecules [133]. However, as in the case of the addition of PBASE, there also appears to be an increase in hole mobility, which may be due to the pyrene groups increasing connectivity within the carbon nanotube network [75].

Subsequently, the device was rinsed with 1XPBS and exposed to 20 mM EDC and 40 mM NHS in 1XPBS electrolyte for 30 minutes. Figure 2.7b shows the change resulting from subsequent EDC/NHS exposure. When EDC/NHS is added, a threshold shift of  $\Delta V \sim -0.08$  V was observed on multiple channels. The exposure to EDC/NHS negatively shifts the transfer characteristic curve, most likely due to the PBA present reacting to form positively-charged *O*-acylisourea esters and negatively gating the attached carbon nanotube network [37], [129]. Figure 2.7c shows that this shift is not significantly affected by further exposure of the channel to PBS. This indicates that hydrolysis over the course of one hour is insufficient to hydrolyse a significant proportion of the *O*-acylisourea back to PBA, as PBA is charge neutral. We therefore expect that the a significant amount of *O*-acylisourea remains active within this time period and available for reaction with biomolecule amine groups.

## 2.4. Attachment of 1-Pyrenebutyric Acid

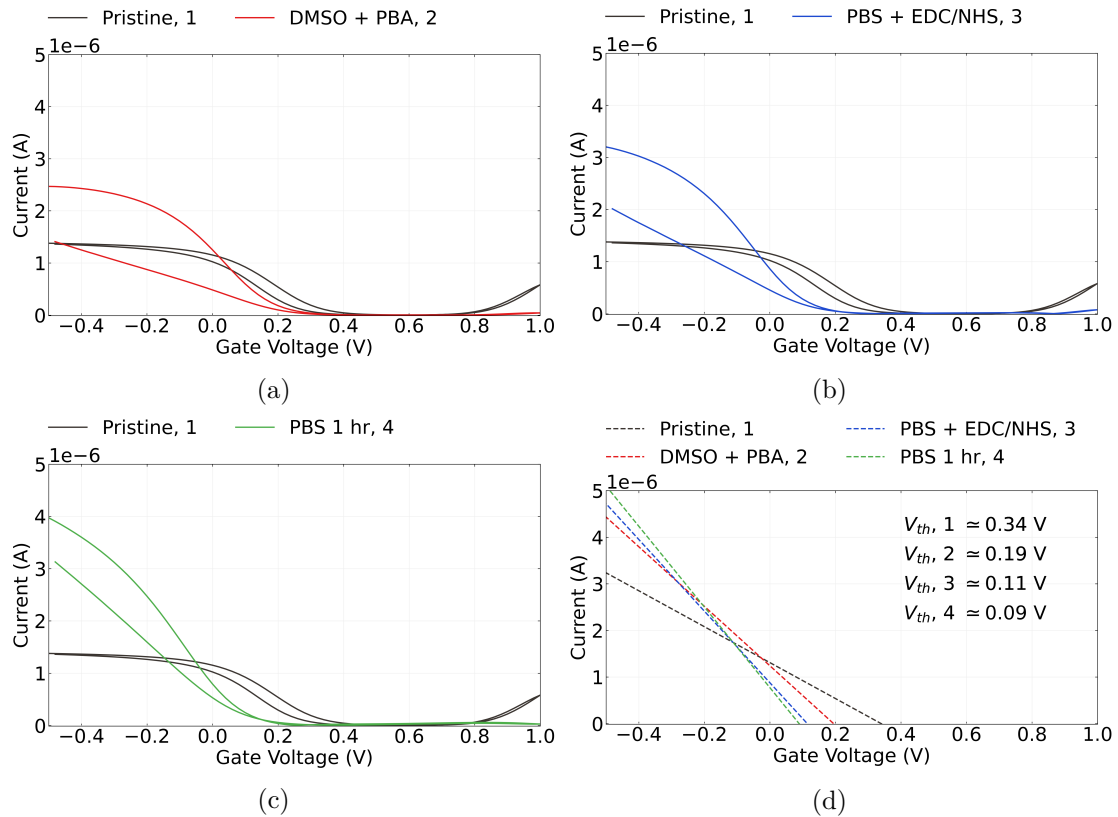


Figure 2.7.: Electrical transfer characteristics of a carbon nanotube transistor before functionalisation alongside the transfer characteristics (a) after being submerged in DMSO containing 5 mM PBA for 1 hour in red, (b) after being submerged in 1XPBS containing 20 mM EDC and 40 mM NHS for 30 min in blue, and (c) after being submerged in fresh 1XPBS for 1 hour in green. The dashed lines in (d) are linear fits tangent to the subthreshold slope of each characteristic curve, and are shown alongside the threshold voltages calculated by finding the intercept of each fit.

## 2.5. Attachment of PEGylated Pyrene-Based Linkers

### 2.5.1. Pyrene-NTA, Pyrene-Biotin and PEGylation

Through chemical coupling/conjugation, it is possible to replace the NHS ester group on PBASE with other groups that can undergo binding reactions with proteins. Unlike PBASE, these groups do not suffer the drawback of being readily hydrolysed. For example, PBASE can be modified with Na<sub>2</sub>Na<sub>2</sub>-Bis(carboxymethyl)-L-lysine hydrate (also known as N-(5-Amino-1-carboxypentyl)iminodiacetic acid, AB-NTA) to produce pyrene-nitrilotriacetic acid (pyrene-NTA). The attached NTA group is able to chelate with metal ions such as Cu<sup>2+</sup> or Ni<sup>2+</sup>, which then can then coordinate with polyhistidine-tags attached to a protein [134]–[136]. Use of Cu<sup>2+</sup> ions over Ni<sup>2+</sup> gives stronger histidine bonding and less non-specific adsorption [136]. Functionalisation using the NTA-Ni<sup>2+</sup> chemistry was successfully used to attach mammalian odorant receptors to a single carbon nanotube for detection of eugenol vapour in real-time [73]. Pyrene-biotin (pyrene butanol biotin ester) can also be produced for attaching avidin or streptavidin [134]. As avidin and streptavidin are tetrameric, they can be attached to both pyrene-biotin and biotinylated avi-tagged proteins simultaneously via strong non-covalent bonding, therefore linking the transducer and receptor [137]–[140]. As the presence of his-tags and avi-tags on proteins can be readily controlled, these methods offer improved specificity and directionality over the traditional amide bonding seen earlier.

It is also possible to attach polyethylene glycol (PEG) chains to a pyrene group and modify them with reactive groups such as NTA and biotin to attach proteins in the manner outlined in the previous paragraph [141], [142]. Once modified with PEG, the water solubility of pyrene linkers increases, making it possible to perform a full functionalisation procedure exclusively in aqueous solution [141]. By setting the length of the PEG chain, the size of the linker molecule can be controlled - selection of a short chain is important for ensuring attached receptors remain within the Debye length of the transducer [65]. Functionalisation of a graphene transducer with pyrene-PEG-biotin has previously been used to bind streptavidin to a graphene field-effect transistor device [143]. The PEGylated linkers used in the following sections were purchased pre-prepared. Pyrene-PEG-NTA (2 kDa) was purchased from Nanocs, while pyrene-PEG-FITC (2 kDa, 10 kDa), pyrene-PEG-rhodamine (3.4 kDa), mPEG-Pyrene (10 kDa) and pyrene-PEG-biotin (10 kDa) were purchased from Creative PEGworks.

## 2.6. Identifying Functionalisation Issues using Fluorescence Microscopy

### 2.6.1. General Overview

Various dyes and fluorescent tags were used to investigate approaches for identifying successful attachment of biomolecules to a carbon nanotube or graphene surface with fluorescence microscopy. The dyes included fluorescein isothiocyanate (FITC), Rhodamine B and Cyanine 3 (Cy3). Green fluorescent protein was also used for this testing process. It is important to note that these dyes and the GFP chromophore all contain benzene rings which are able to  $\pi$ -stack with carbon rings to some degree [144]–[147]. However, there is also significant variation in the effectiveness of this  $\pi$ -stacking, as shown by Figure 2.8. Here, a clear, specific interaction is seen between Rhodamine B and graphene, but little interaction between FITC and graphene is observed, even when a longer exposure time is used. Whether the addition of pyrene linker groups to these dyes, or dye-modified biomolecules, was therefore investigated in further detail. This process then led to the identification of multiple issues that could impede a successful device functionalisation.

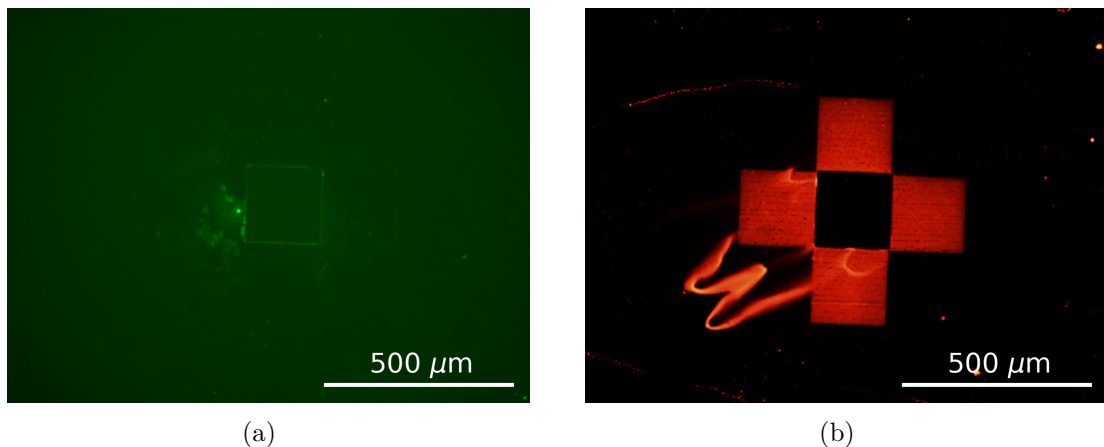


Figure 2.8.: Four 200  $\mu\text{m} \times 200 \mu\text{m}$  graphene squares modified with the dyes (a) fluorescein isothiocyanate (FITC) and (b) Rhodamine B. No pyrene/PEG/pyrene-PEG was attached to these dyes. In (a), an FITC filter and 6.5 s exposure time was used, and in (b) a Texas Red filter and 1.4 s exposure time was used.

Both SU8 and AZ® 1518 photoresist fluoresced under a variety of microscope filters, resulting from light interacting with the photoactive component present in both resists [148]. This background fluorescence was found to drown out fluorescence from a dye-functionalised device channel, and so photoresist encapsulated devices were not used for fluorescence imaging. (Consider a photograph of a dim outdoor lamp; if the photograph

## 2. Non-Covalent Functionalisation of Carbon Nanotubes and Graphene

was taken on a starless night, the light from the lamp would show up clearly, but with the sun out the light would be very difficult to see regardless of how the photograph was taken.) A different type of encapsulation could potentially be used to verify linker attachment with fluorescence after a device has been encapsulated. These alternative encapsulation methods for use with fluorescence microscopy are discussed in [?@sec-future-work](#).

### 2.6.2. Photoresist Contamination

An functionalisation issue quickly encountered when characterising pyrene-PEG-FITC (PPF) interaction with sensing channels via fluorescence microscopy was an unwanted secondary interaction between the linker and residual photoresist. Figure 2.9a and Figure 2.9b are fluorescence images of SU8 encapsulation (using the pre-2023 mask) before and after being exposed to PPF. Despite the same microscope settings being used to take the images (filter, ISO, contrast, exposure time), the SU8 exposed to PPF appears much brighter than the pristine SU8. This result indicates that the linker appears to have an extensive interaction with the photoresist via an unknown mechanism. No fluorescence is seen from the device channel. The length of exposure time required to see fluorescence from the modified channel would lead to fluorescence from the modified linker attached to the photoresist – as well as the photoresist itself – flooding the image with light. Therefore, it is not clear whether the carbon nanotubes have been functionalised with the dye-modified linker. However, out of caution we can assume that the presence of this secondary interaction is not desirable.

A similar interaction was seen between AZ® 1518 photoresist and fluorescent-tagged, amine-terminated aptamer. An unencapsulated carbon nanotube network device, fabricated using the pre-June 2022 process outlined in [?@sec-fabrication](#), was incubated with 500 nM Cy3-tagged aptamer in Tris buffer at 4°C overnight. The aptamer was first denatured by heating in a water bath at 95°C for 5 minutes then cooling in an ice bath for 10 minutes before use.

Figure 2.9c and Figure 2.9d are fluorescence images of the device channel region before and after exposure to aptamer. A thick red ring is visible around the electrodes after functionalisation, despite no PBASE being used to tether the amine-terminated aptamer. It appears that these bright patches correspond to patches of residual photoresist which have not been completely removed from the carbon nanotube square by the development process. These patches have then interacted with the aptamer, causing them to appear bright under the fluorescence microscope. Beyond potentially interfering with functionalisation, photoresist residue blocking a device channel will prevent interaction with the buffer and prevent sensing.

To test whether residual resist could be prevented from interacting with aptamer by crosslinking the resist, two unencapsulated devices were prepared as follows. Devices were first spincoated with AZ® 1518 in the manner described in [?@sec-fabrication](#).

## 2.6. Identifying Functionalisation Issues using Fluorescence Microscopy

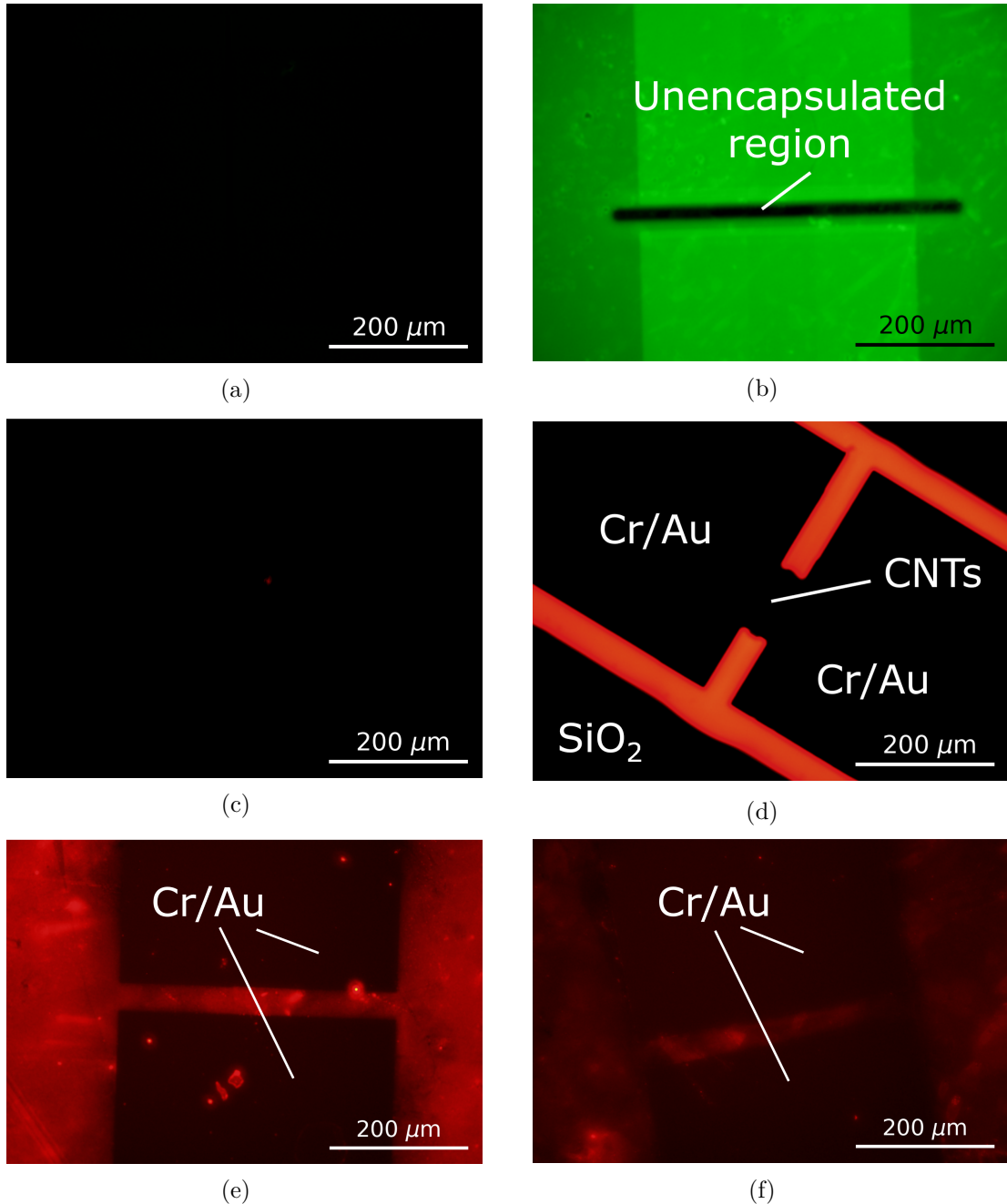


Figure 2.9.: A fluorescence image of a SU8-encapsulated carbon nanotube device is shown in (a), while (b) shows the same channel after modification with an solution of 1 mM Pyrene-PEG-FITC. A 0.35 s exposure time and FITC filter were used for (a)-(b). The fluorescence image in (c) shows an unencapsulated channel, while (d) shows the same channel after Cy3-tagged aptamer exposure. A 10 s exposure time and mCherry filter were used for (c)-(d). The fluorescence images in (e) and (f) show devices pre-coated with a thin layer of photoresist then submerged in Cy3-tagged aptamer, where the device in (f) was hardbaked before aptamer exposure. An mCherry filter and 30 s exposure time were used for (e)-(f).

## *2. Non-Covalent Functionalisation of Carbon Nanotubes and Graphene*

Next, the majority of resist was removed by soaking the device in acetone for 1 minute. This process left a thin coating of photoresist on the devices. One of these devices was then hardbaked at 200°C for 1 hour. Both devices were subsequently functionalised in the following manner:

1. Unencapsulated device was submerged in 1 mM PBASE in methanol solution for 1 hour.
2. The device was then rinsed with methanol and Tris buffer.
3. 1  $\mu$ M Cy3-tagged aptamer was denatured by heating in a water bath at 95°C for 5 minutes then cooling in an ice bath for 10 minutes before use.
4. The device was incubated with aptamer in Tris buffer at 4°C overnight.

Fluorescence microscope images of channels from each device are shown in Figure 2.9e and Figure 2.9f, where the latter is the device hardbaked before functionalisation. By comparing the two images, it is apparent that hardbaking the AZ® 1518 photoresist significantly reduces the amount of fluorescent aptamer attached to the surface. This result is an indication that sufficient heating of the photoresist can prevent it interacting with PBASE or amine-tagged biological material. However, there is still some Cy3-tagged aptamer fluorescence visible in Figure 2.9f. It appears that hardbaking has not completely prevented photoresist from interacting with the aptamer. It is possible that heating from the bottom of the device is insufficient to hardbake the photoresist layer completely, an effect that would be amplified for the thick photoresist layer on encapsulated devices. Therefore, from June 2023 onwards devices were vacuum annealed for 1 hour at 150°C prior to functionalisation. This approach was taken to ensure photoresist was heated from above as well as below and made chemically inert across its surface.

This result demonstrates the use of fluorescence microscopy as a tool to detect residue and test suitable residue elimination measures. Further testing showed that performing a 1 minute flood exposure (for positive resist only) then placing a device in AZ® 326 developer for 3 minutes was highly effective at removing photoresist residue. Both these development and annealing techniques were used for all functionalised devices in subsequent sections.

### **2.6.3. Hydrophobicity of Carbon Nanotubes and Graphene**

As PEGylated linker dissolves well in aqueous solution, initial fluorescence imaging focused on functionalising devices with these linkers dissolved in 1XPBS. It was hoped that by keeping the device channels in a pH-controlled environment, the channel surface would be made more suitable for the attached receptors. Figure 2.10a shows a graphene film after exposure to pyrene-PEG-rhodamine (PPR) in 1XPBS solution for 1 hour. The pyrene-PEG-rhodamine has interacted with the silicon dioxide substrate (discussed

## 2.6. Identifying Functionalisation Issues using Fluorescence Microscopy

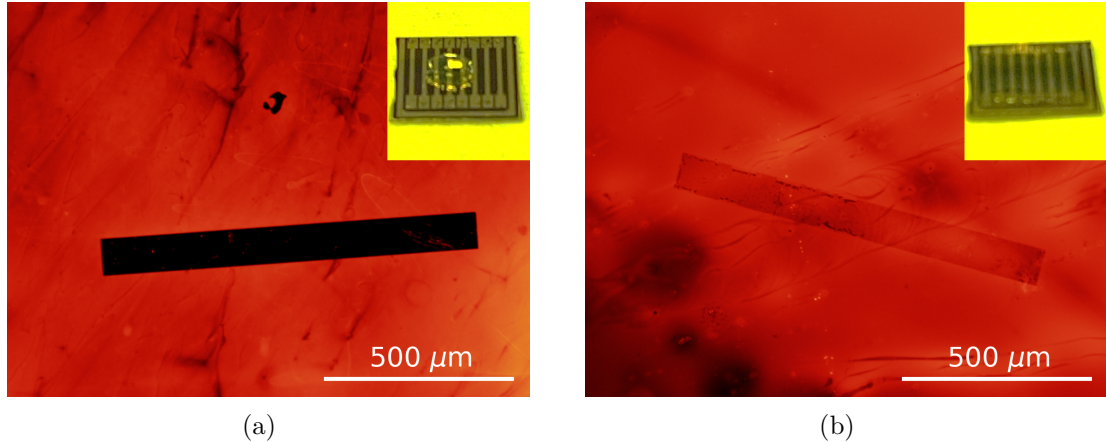


Figure 2.10.: Fluorescence images of a  $1000 \mu\text{m} \times 100 \mu\text{m}$  graphene channel after functionalisation with 1 mM pyrene-PEG-rhodamine in 1XPBS. The graphene film in (a) was not oxygen plasma cleaned before functionalisation, while the graphene film in (b) was oxygen plasma cleaned at 5 W for 15 s at 300 mTorr pressure immediately before functionalisation. Insets show a  $10 \mu\text{L}$  droplet placed on an unencapsulated carbon nanotube device before (a) and after (b) the same oxygen plasma treatment procedure. Images were taken using a Texas Red filter and a 1.8 s exposure time.

further in Section 2.6.4) but not the graphene film. The graphene has not attached to the pyrene or rhodamine due to the highly hydrophobic graphene surface repelling the surrounding solution, preventing  $\pi$ -stacking from occurring. The hydrophobicity of the graphene surface is not intrinsic to graphene, but instead results from a hydrocarbonaceous layer which forms on the channel surface when exposed to air [149]. A hydrophobic layer will also form on carbon nanotube networks [150], [151]. Treatment with oxygen plasma at 5 W for 15 s has previously been found to remove this hydrocarbonaceous layer, restoring the intrinsic hydrophilicity of graphene [152]. Storing the graphene surface in deionised water rather than air prevents the return of this hydrocarbon layer [149]. The use of a relatively low power plasma ensures damage to the graphene layer is minimised.

Treatment of an unencapsulated carbon nanotube network device at 5 W for 15 s at 300 mTorr greatly reduced the contact angle of a water droplet placed on the device surface, shown inset in Figure 2.10 before and after plasma treatment. A graphene film was then functionalised with pyrene-PEG-rhodamine in 1XPBS in the same manner as for the film in Figure 2.10a, except with the same plasma treatment performed on the film less than 1 minute before functionalisation. The result is shown in Figure 2.10b. The graphene now appears to interact with the pyrene-PEG-rhodamine. These results both indicate that the plasma treatment is increasing the hydrophilicity of the device surface, improving the ability of pyrene-PEG-rhodamine to  $\pi$ -stack with graphene. The disadvantage of this procedure is that the plasma cleaning introduces defects to the graphene surface

## 2. Non-Covalent Functionalisation of Carbon Nanotubes and Graphene

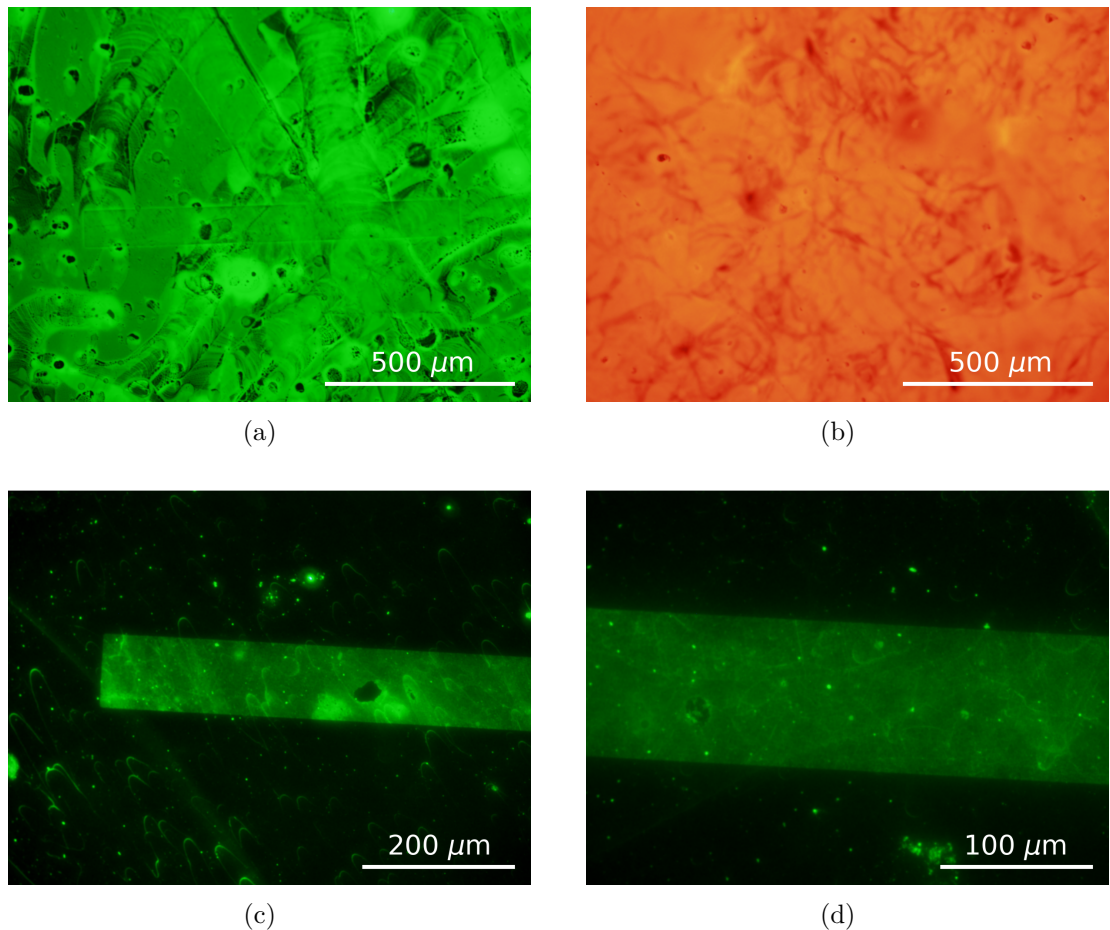


Figure 2.11.: The  $1000 \mu\text{m} \times 100 \mu\text{m}$  graphene film in image (a) was functionalised with 1 mM pyrene-PEG-FITC in 1XPBS after oxygen plasma treatment, taken using an FITC filter and a 1.6 s exposure time. (b) shows a silicon dioxide surface which had never been exposed to carbon nanotubes, graphene or photoresist after exposure to 1 mM pyrene-PEG-rhodamine in 1XPBS, taken using a Texas Red filter and a 1.8 s exposure time. Graphene films on a substrate functionalised with 1 mM pyrene-PEG-FITC in 1XPBS after oxygen plasma treatment then cleaned with m-CNT dispersion surfactant (NanoIntegris) are shown in (c) and (d), where a FITC filter was used, with 7.5 s and 7.75 s exposure times respectively.

## 2.6. Identifying Functionalisation Issues using Fluorescence Microscopy

which may be undesirable for device electrical behaviour. Furthermore, it was often found that devices functionalised in this manner had their conductance drop significantly after functionalisation, even though plasma treatment itself did not significantly alter device conductance. Solvent was therefore used for the initial linker functionalisation in Section 2.7, as it did not require a plasma cleaning step for successful attachment.

### 2.6.4. Substrate Interaction with Linker Molecules

Another issue that arose when verifying surface functionalisation was the interaction between pyrene linker and the silicon dioxide substrate. This interaction meant it was difficult to discern whether the pyrene group was interacting in a specific manner with the channel film. It was confirmed that pyrene-PEG was interacting with silicon dioxide, rather than residual photoresist or nanomaterial, by performing a pyrene-PEG-rhodamine functionalisation on pristine silicon dioxide, as shown in Figure 2.11b. The PEGylated linker supplier suggested that the surface should be thoroughly rinsed with surfactant to remove weakly-bound pyrene-PEG-FITC attached to the silicon dioxide, while preserving the pyrene-PEG-FITC strongly attached via  $\pi$ -stacking to the graphene or carbon nanotube film [153]. The following process was then used to remove pyrene-PEG-FITC from the silicon dioxide: the film was rinsed with DI water for 30 s, then placed in m-CNT dispersion solution (NanoIntegris) for 5 minutes at 70°C while agitating with a pipette, and finally rinsed with DI water, ethanol, acetone, IPA and nitrogen dried. The results of this thorough cleaning process are shown in Figure 2.11c and Figure 2.11d. The majority of pyrene-PEG-FITC was removed in regions with no graphene, but remained where graphene was present, indicating specific,  $\pi$ -stacking interaction took place between the pyrene-PEG-FITC and graphene. However, this surfactant rinse step was not used when performing functionalisation with biological materials, to prevent damage to the lipid membranes used.

### 2.6.5. Coffee-Ring Effect

From Table 2.1, full device submersion appears to be the most common approach for functionalisation with solution containing linker molecules like PBASE. However, some groups placed small droplets of solution onto the device channels when functionalisation, and this approach was tested as part of the fluorescence verification work. For functionalisation with his-tagged green fluorescent protein, after plasma cleaning at 5 W for 15 s at 300 mTorr, a 4  $\mu$ L droplet of 100  $\mu$ M pyrene-PEG-NTA in 1XPBS was placed on each graphene device channel and left covered in a humid environment for 15 minutes. The device was then rinsed with 1XPBS, submerged in 10 mM NiSO<sub>4</sub> in 1XPBS for 1 hour, rinsed in 1XPBS, then submerged in 10 mL of 100 ng/mL his-tag GFP solution (Thermofisher) overnight. Fluorescence microscope imaging showed that a ring of biomaterial would build up around the outer edge of regions where pyrene-PEG-NTA had been present, as seen in Figure 2.12.

## 2. Non-Covalent Functionalisation of Carbon Nanotubes and Graphene

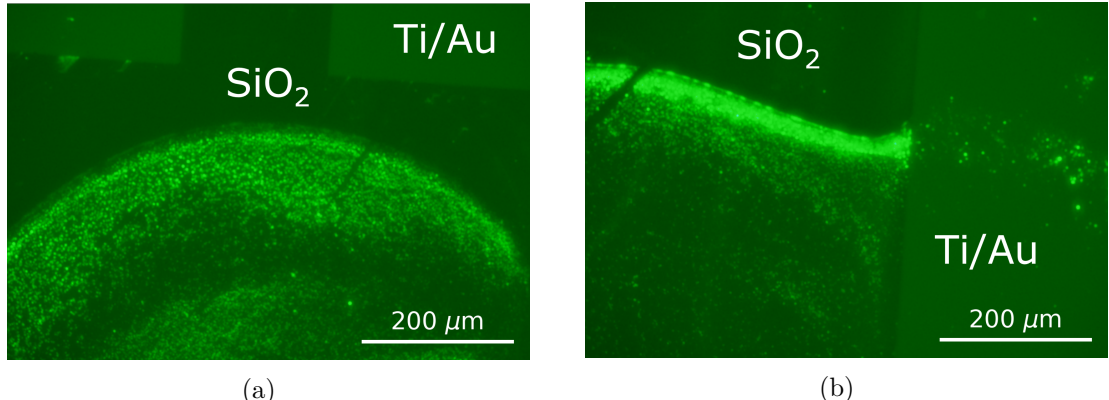


Figure 2.12.: Both (a) and (b) show a build-up of his-tag GFP at the edges of the droplet region where pyrene-PEG-NTA had been present, taken using an GFP filter and a 5 s exposure time. On the right hand side of (b), no his-tag GFP is visible on the metal electrode, as no pyrene-PEG attaches to the metal electrodes.

It appears this is a result of the his-tag GFP attaching to a dense region of pyrene-PEG-NTA at the edge of the functionalisation droplet. This accretion of pyrene-PEG-NTA at the edge of the droplet is a result of the coffee-ring effect, where the evaporation of the droplet leads to transport of particles to the droplet edges via capillary flow [18], [154]. As this gradient in surface coverage of attached proteins has unknown consequences for sensing, in subsequent sections devices were functionalised with PBASE or pyrene-PEG-NTA by submerging them in solution instead of dropcasting.

## 2.7. Verifying Linker-OR Nanodisc Attachment with Fluorescence Microscopy

### 2.7.1. GFP-OR Nanodisc Functionalisation

To verify the formation of amide (or imide) bonds between PBASE and the odorant receptors (ORs) contained within nanodiscs, a fluorescent biomarker was directly attached to the odorant receptors for detection with fluorescence microscopy. The biomarker used was the *Aequorea Victoria* green fluorescent protein (GFP). The functionalisation of unencapsulated carbon nanotube devices (steam-deposited, fabricated using post-June 2023 methods outlined in ?@sec-fabrication) with PBASE and GFP-OR nanodiscs was performed as follows:

1. The device was exposed to UV light for 1 minute, placed in AZ® 326 developer for 3 minutes, then rinsed with acetone, isopropanol and nitrogen dried.

## *2.7. Verifying Linker-OR Nanodisc Attachment with Fluorescence Microscopy*

2. The device was vacuum annealed for 1 hour at 150°C (Note: Steps 1 & 2 were added to ensure any residual photoresist on the channel was removed or passivated before functionalisation, see Section 2.6.2).
3. A solution of 1 mM PBASE (Setareh Biotech) in methanol prepared by fully dissolving 2 mg PBASE in 5 mL methanol by vortex mixing at 1000 rpm in a dark room (Note: PBASE was stored at -18°C for 18 months prior to use, and was thawed under vacuum for 15 minutes in dark conditions before opening)
4. The device was then rinsed with methanol, fully submerged in ~ 1 mL of PBASE in methanol solution and left covered with parafilm for 1 hour, then rinsed with methanol for 15 s, rinsed with 1XPBS for 15 s and nitrogen dried to remove residual PBASE.
5. The device was left dry and in darkness while collecting the GFP-OR nanodiscs from the -80°C freezer. An opaque cover was placed over the GFP-OR vial to shield it from light.
6. 20 µL GFP-OR nanodiscs (batch number ND-GFP-OR43b-0002, prepared 12 months earlier) were diluted in 2 mL 1XPBS (Note: The full 2 mL was used to flush out the nanodisc vial when preparing the nanodisc solution, with successive additions and subtractions of 50 µL 1XPBS into and from the vial).
7. The device was submerged in the GFP-OR43b nanodisc solution and left covered with parafilm for 1 hour in darkness, then rinsed with 1XPBS for 15 s.
8. For fluorescence microscopy, the device was briefly rinsed with DI water and nitrogen dried to remove dried-down salt residue left by the 1XPBS.

A control device was prepared using the same process but skipping steps 3 and 4.

### **2.7.2. Fluorescence Microscopy**

Fluorescence images of the GFP-OR43b and control devices discussed in Section 2.7.1 are shown in Figure 2.13. Fluorescence microscope images were taken immediately after functionalisation; devices were transported to the fluorescence microscope room in a foil-wrapped container, and the fluorescence microscope room was kept dark while images were taken. All fluorescence images were taken of channels with ungated resistance measurements within a 50-500 kΩ range both before and after functionalisation.

The silicon dioxide regions in each image appear bright under the GFP filter, indicating non-specific binding between the GFP-OR43b nanodiscs and the silicon dioxide substrate. As this device has been annealed, UV exposed and developed before functionalisation, this non-specific attachment is unlikely to be interaction with residual photoresist (see Section 2.6.2). The SiO<sub>2</sub> substrate also appears brighter in the images on the right of Figure 2.13, which are of the device initially exposed to PBASE. The discussion in Section 2.6.4 indicates that the pyrene moiety of PBASE non-specifically

2. Non-Covalent Functionalisation of Carbon Nanotubes and Graphene

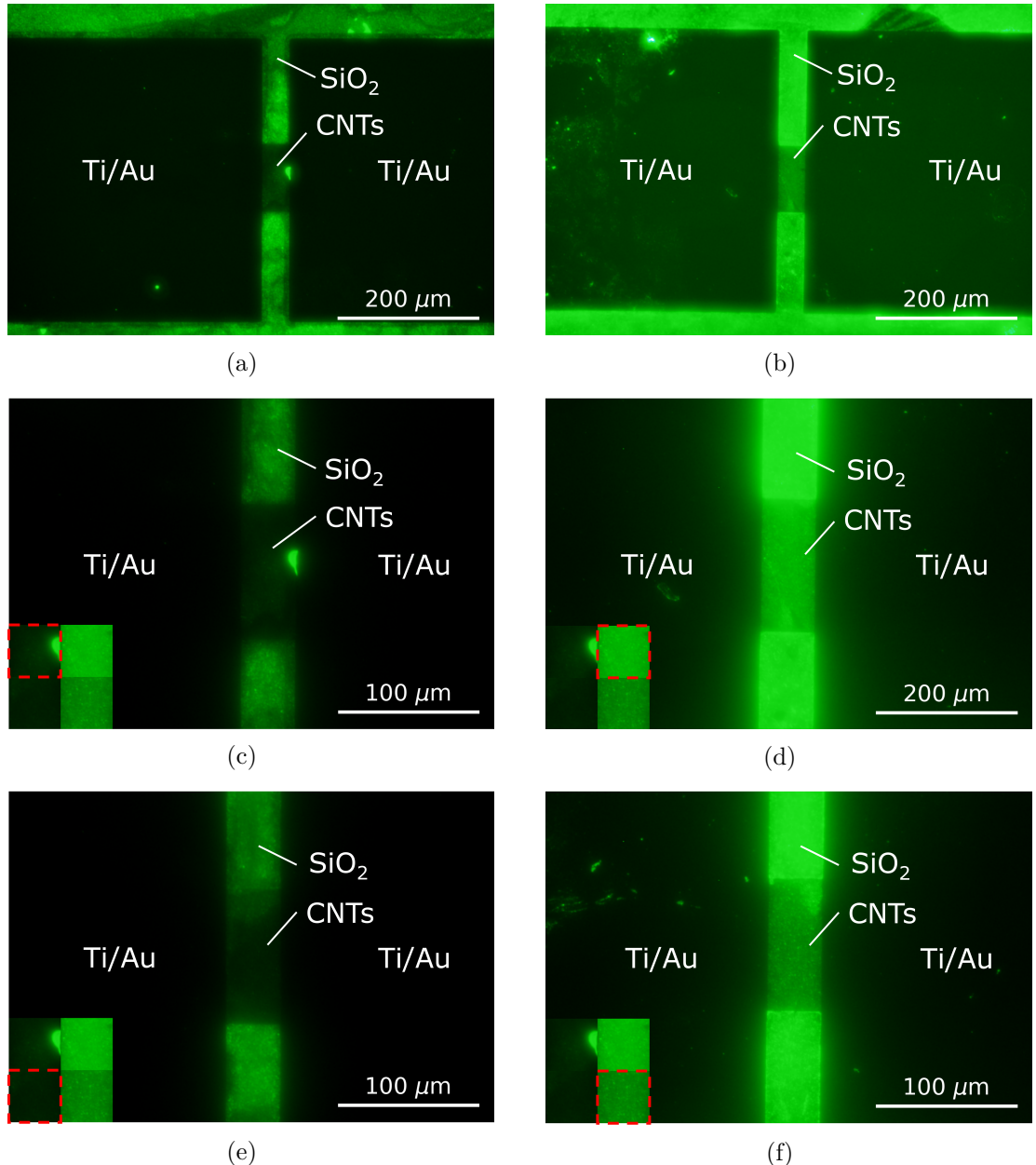


Figure 2.13.: The fluorescence images on the left side – (a), (c) and (e) – show unencapsulated carbon nanotube network channels from a device incubated in GFP-OR43b nanodiscs. The rectangular dark regions to the left and right of each image are the gold electrodes. The fluorescence images on the right – (b), (d) and (f) – show the channels of a similar device after successive PBASE and GFP-OR43b nanodisc incubation. Images (a) and (c) are both of the same channel on the first device, and images (b) and (d) are of the same channel on the second, but (c) and (d) were taken using a greater magnification. The insets in (c)-(f) compare the central channel region of (c)-(f) more directly. All images were taken with the same microscope settings (GFP filter and 10 s exposure time), directly after functionalisation in a dark room.

interacts with the silicon dioxide substrate. The attachment of GFP-OR43b nanodiscs to this PBASE coating appears have led to more GFP-OR43b nanodiscs attaching to the silicon dioxide, giving rise to the brighter fluorescence of the silicon dioxide seen for the PBASE-incubated device on the right of Figure 2.13.

A comparison of fluorescence in the channel region between images on the left of Figure 2.13 (GFP-OR43b only) and the images on the right (GFP-OR43b and PBASE) is given by the inset in Figure 2.13c-f. The inset demonstrates that the channels not incubated in PBASE are significantly less bright than those that had been incubated with PBASE. It appears that, as expected from the discussion in Section 2.6.3, the GFP-OR43b in 1XPBS is unable to approach the unmodified channel due to the hydrophobicity of the carbon nanotubes. However, when the carbon nanotubes are modified with PBASE, the GFP-OR43b is able to attach to the channel, and so the channel shows up brightly under the fluorescence microscope GFP filter. This trend was consistent across all conducting channels on each of the two devices. As far as I know, this is the first time fluorescence has been used to verify the successful attachment of odourant receptor nanodiscs to a carbon nanotube network.

## 2.8. Conclusion

It has been well-established in the literature that the  $\pi$ -stacking reaction mechanism between pyrene-based linkers and graphene and carbon nanotube network field-effect transistors can be used to create working biosensors. The previous use of various linker molecules for biosensor functionalisation was investigated. Despite the wide use of 1-pyrenebutanoic acid N-hydroxysuccinimide ester (PBASE) and 1-pyrenebutyric acid (PBA) for functionalisation of biosensors, the literature shows a significant variation in the methods used for attachment of linker molecules to a transistor channel. The most common methods, using 6 mM PBASE dissolved in dimethylformamide or 1 mM PBASE in methanol, stem directly from the first documented use of PBASE for functionalisation of carbon nanotube biosensors. In the last 6 years, more research has been done into optimising the PBASE methodology for graphene devices, but there is still disagreement in the literature over whether minimising or maximising PBASE coverage on a graphene device channel is desirable for sensing. Due to disagreement in the literature around suitable non-covalent methods for biosensor functionalisation, several steps were taken to identify a rapid and simple method for verifying successful functionalisation, and to locate any potential barriers to a successful functionalisation.

I first compared the advantages and disadvantages of the various linker molecules under investigation. The use of hydrogen NMR gave indications that water was present in PBASE samples prepared in DMSO. Concerns around the impact of the hydrolysis of PBASE on functionalisation mean that the presence of water is strongly undesirable. An alternative functionalisation approach less prone to hydrolysis is the reaction

## 2. Non-Covalent Functionalisation of Carbon Nanotubes and Graphene

of PBA with EDC in the presence of NHS. However, this process has its own disadvantages, such as undesirable protein interactions and the increased amount of steps and process variables involved. Pyrene-NTA is also less prone to hydrolysis than PBASE but unlike PBASE or PBA/EDC interacts with a specific protein tag, the histidine tag. PEGylation of the pyrene-NTA linker also means that the entire functionalisation process can be performed in aqueous solution, avoiding the introduction of non-organic solvents. This approach is desirable, since the non-aqueous solvents traditionally used for functionalisation may have negative impacts on device behaviour. For example, carbon nanotube device channel transfer characteristics were found to undergo a significant shift of  $\Delta V = -0.15 \pm 0.02$  when exposed to DMSO or MeOH for 1 hour.

Next, I verified that the pyrene groups of the linker molecules of interest were attaching successfully to either carbon nanotubes or graphene. Raman spectroscopy showed that incubating a highly-bundled carbon nanotube film in 5 mM PBASE or PBA in DMSO for 1 hour increased  $I_D/I_G$  by a factor of  $\sim 3$  relative to the DMSO-only case. Incubating a steam-deposited carbon nanotube device in a 1 mM concentration of PBASE in methanol or DMSO for 1 hour was found to cause a significant increase in device on-current relative to the solvent-only case, and a similar increase in on-current was seen for 5 mM PBA in DMSO relative to the DMSO-only case. When a PBA-functionalised device was placed in aqueous solution with 20 mM EDC and 40 mM NHS for 30 minutes, a further increase in on-current was seen. Fluorescence microscopy was used to demonstrate the successful attachment of pyrene-PEG to graphene using an attached FITC probe, where immersing a graphene film in 1 mM pyrene-PEG in ethanol led to the channels becoming brightly fluorescent relative to the background using a 1 s exposure time.

Various obstacles to successful functionalisation were encountered and addressed. Photoresist contamination was addressed with exposure and development steps before functionalisation (no exposure for SU8 encapsulated devices). Hydrophobicity of graphene films was addressed by plasma treatment before functionalisation in aqueous solution. A surfactant rinse was used to distinguish between weak substrate-linker interaction and  $\pi$ -stacking between linker and the channel. Finally, coffee-ring distribution of linker was addressed by always submerging the device in linker when functionalising.

Finally, fluorescence microscopy was used to investigate PBASE functionalisation of GFP-tagged odorant receptors. An eight-channel device was modified by submersion in 1 mM PBASE in methanol for 1 hour, then submersion in  $10 \mu\text{L mL}^{-1}$  OR43b nanodiscs in 1XPBS for 1 hour. An eight-channel control device was also prepared by submersion in  $10 \mu\text{L mL}^{-1}$  OR43b nanodiscs in 1XPBS for 1 hour, but with no PBASE. The channels of the PBASE-submersed devices showed significant GFP fluorescence, while the channels of the control devices showed little to no GFP fluorescence. As far as I am aware, this is the first time fluorescence has been used to verify successful attachment of odorant receptors to a carbon nanotube network.

### **3. Biosensing with Insect Odorant-Receptor Functionalised Carbon Nanotube Devices**

#### **3.1. Introduction**

To test devices with the new vapour delivery system, it was important to first ensure the functionalised devices worked consistently as biosensors in the existing aqueous sensing setup.

#### **3.2. Aqueous Sensing of Ethyl Hexanoate with OR22a-functionalised Carbon Nanotube Transistor**

##### **3.2.1. OR Nanodisc Functionalisation**

A carbon nanotube network field-effect transistor device, fabricated using post-June 2023 methods as described in [?@sec-fabrication](#), was functionalised with OR22a nanodiscs. The network used for the device was deposited using the steam-assisted surfactant method, and the device was encapsulated with AZ® 1518 using the post-Jan 2023 photolithography mask. The functionalisation was performed as follows:

1. The device was exposed to UV light for 1 minute, placed in AZ® 326 developer for 3 minutes, then rinsed with acetone, isopropanol and nitrogen dried.
2. The device was vacuum annealed for 1 hour at 150°C.

Note: Steps 1 & 2 were added to ensure any residual photoresist on the channel was removed or passivated before functionalisation, see Section 2.6.2.

3. A solution of 1 mM PBASE (Setareh Biotech) in methanol was prepared by fully dissolving 2 mg PBASE in 5 mL methanol by vortex mixing at 1000 rpm in a dark room.

Note: PBASE was stored at -18°C for 18 months prior to use, and was thawed under vacuum for 15 minutes in dark conditions before opening.

### *3. Biosensing with Insect Odorant-Receptor Functionalised Carbon Nanotube Devices*

4. The device was then rinsed with methanol, fully submerged in  $\sim$  1 mL of PBASE in methanol solution and left covered with parafilm for 1 hour, then rinsed with methanol for 15 s, rinsed with 1XPBS for 15 s and nitrogen dried to remove residual PBASE.
5. The device was left dry and in darkness while collecting the OR22a nanodiscs from the -80°C freezer.
6. 10  $\mu$ L OR22a nanodiscs (batch number ND-OR22a-SB018, 1.9 mg/mL, prepared 7 months earlier) were diluted in 1 mL 1XPBS

Note: The full 1 mL was used to flush out the nanodisc vial when preparing the nanodisc solution, with successive additions and subtractions of 50  $\mu$ L 1XPBS into and from the vial.

7. The device was submerged in the OR22a nanodisc solution and left covered with parafilm for 1 hour, then rinsed with 1XPBS for 15 s and gently nitrogen dried.

Liquid-gated electrical characteristics were taken of the sensing channel (channel 7) before and after functionalisation with OR22a. These electrical characteristics were taken in using a liquid gate buffer of 1XPBS containing 0.5% DMSO with the B1500A semiconductor device analyser. These characteristics are shown in Figure 3.1, shown using both a logarithmic and linear current scale. The device exhibited ambipolar characteristics before functionalisation, which is typically seen for steam-deposited carbon nanotube films (Section 1.3.2). However, *p*-type behaviour dominates after device functionalisation due to a significant drop in *n*-type conductance. There was little hysteresis present, which is also typical for these devices. A slight increase in hysteresis was observed post-functionalisation. Leakage current (shown by the dashed traces) never exceeds  $1 \times 10^{-7}$  V, both before and after functionalisation. The significant change in electrical characteristics observed could be due to five possible factors – adsorption of solvent onto the network, network attachment of PBASE without subsequent protein attachment, non-specific adsorption of protein onto the network, PBASE-mediated attachment of the membrane scaffold protein (MSP) of nanodiscs to the network, and PBASE-mediated attachment of odorant receptors to the network. Note that as the nanodisc volume is much larger than that of the odorant receptor, any direct protein adsorption is highly likely to be adsorption of the nanodisc membrane scaffold protein onto the carbon nanotube network. Odorant receptor attachment via PBASE is therefore the only desirable functionalisation result for sensing purposes.

Only minor changes were observed in the on-off ratio when comparing the device channel before and after functionalisation. The on-off ratio for the pristine channel was  $1120 \pm 220$ , fairly typical for a transfer curve from a steam-assisted surfactant-deposited CNT network device (see Section 1.3.2). The on-off ratio increased slightly to  $1830 \pm 550$  after functionalisation. We expect to see an increase in on-off ratio for a device successfully functionalised with OR22a, which may result from an increase in negative charge causing modulation of Schottky barriers between metallic and semiconducting carbon nanotubes

### 3.2. Aqueous Sensing of Ethyl Hexanoate with OR22a-functionalised Carbon Nanotube Transistor

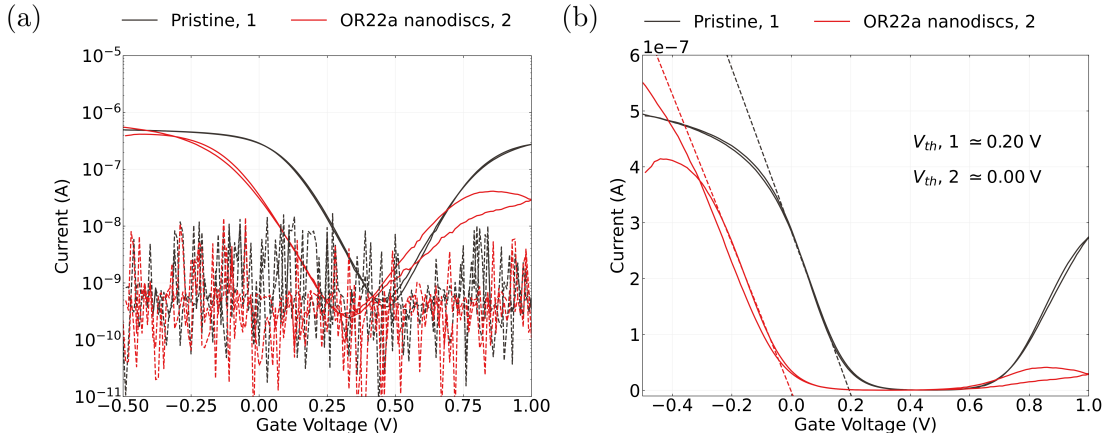


Figure 3.1.: Liquid-gated carbon nanotube network device transfer characteristics before and after OR22a nanodisc functionalisation. In (a), the characteristics are shown on a logarithmic scale, where the gate current for each transfer curve is shown with a dashed line. In (b), the characteristics are shown on a linear scale alongside a dashed line tangent to the subthreshold slope of the characteristic curve. The threshold voltage corresponding to the intercept of this slope with the x-axis is shown for each transfer characteristic curve.

within the network [75]. However, we also expect increased hole conductance from the attachment of PBASE, even without proteins being present (Section 2.3.3). It is therefore difficult to determine whether functionalisation has been successful from the on-off ratio of transfer characteristics alone.

Functionalisation of the channel resulted in a negative shift in threshold voltage of  $-0.20 \pm 0.03 \text{ V}$ . This is significantly in excess of threshold voltage shifts measured for both methanol adsorption ( $-0.15 \pm 0.02 \text{ V}$ ) and after exposure to PBASE in methanol ( $-0.06 \pm 0.04 \text{ V}$ ), confirming that protein has attached to the carbon nanotubes. However, both direct protein adsorption [37], [155] and empty nanodisc attachment [75] should also lead to a significant negative threshold voltage shift in the liquid-gated transfer characteristic curve. In all three cases, the voltage shift is predominantly the result of negative charge transfer from the adsorbed proteins to the semiconducting carbon nanotubes [37], [75], [155]. It is likely that the negative shift observed results from some combination of the three types of attachment. It should be noted that while the size of the functionalisation-induced threshold voltage shift can be used to determine whether protein has attached to the nanodisc network, it cannot be used to specifically determine whether odorant receptors have attached to the network.

Atomic force microscope images of the device channels both before functionalisation and after sensing with the functionalised device to confirm the presence of nanodiscs. As far as the author knows, these are the first atomic force microscope images taken of iOR nanodiscs found on a sensing channel rather than on a separate carbon nanotube

### 3. Biosensing with Insect Odorant-Receptor Functionalised Carbon Nanotube Devices

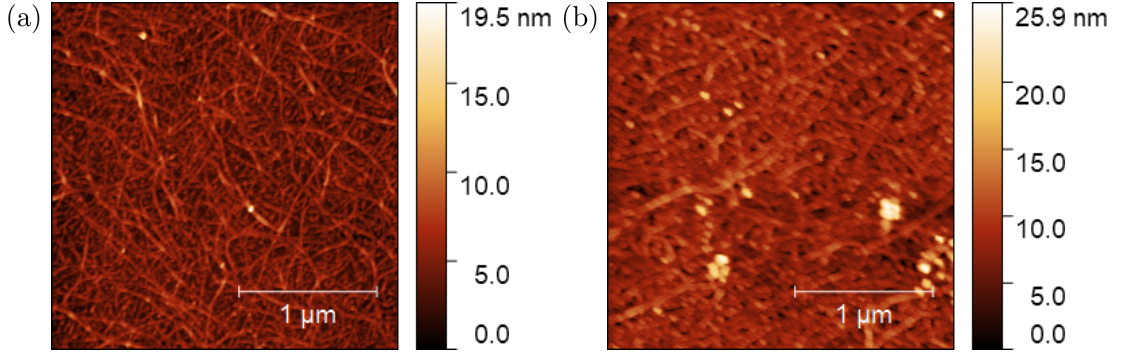


Figure 3.2.: Atomic force microscope images of the channel region of carbon nanotube network devices before and after functionalisation. The channel network of a pristine device is shown in (a), while (b) is of channel 7 from the sensing device functionalised in this section.

film; the wider 20  $\mu\text{m}$  encapsulation mask discussed in ?@sec-encapsulation made this possible. These images are shown in Figure 3.2. Aggregations of nanodiscs are visible in Figure 3.2 (c)–(d). These nanodisc clusters are especially sizable in the lower half of Figure 3.2 (c), where the two largest clusters are  $200 \pm 10 \text{ nm}$  across at their widest point. However, these features are still much smaller than most of the agglomerated nanodisc features seen by Murugathas *et al.* [75]. Furthermore, the nanodisc features closely follow the carbon nanotube bundles across the densely bundled morphology used by Murugathas *et al.* [75]. On the dense network morphology used here, the position of nanodisc clusters relative to the carbon nanotubes is less distinct. To confirm whether nanodiscs have preferentially attached to the carbon nanotubes, a more quantitative approach is needed.

The average height of the substrate was found for both pristine and functionalised atomic force microscope images using the masking tool in Gwyddion. The masks for each image are shown in Figure 3.3. Average substrate heights of  $2.5 \pm 0.2 \text{ nm}$  and  $3.3 \pm 0.4 \text{ nm}$  were found for the pristine and functionalised networks respectively, both within one standard deviation of the substrate height of the steam-assisted surfactant-deposited film analysed in Section 1.2.1. In Gwyddion, both networks were simplified to a binary representation, where features above a certain threshold were shown as white and features below shown as black, as shown in Figure 3.4. This representation has the appearance of a cross-section through the network at the threshold height. The threshold was chosen as the minimum height where carbon nanotube spindles were no longer apparent in the functionalised image, 8.7 nm above the substrate. Figure 3.4 (a) shows only a few, sparsely distributed features, the majority of which are below 50 nm. These features may correspond to surfactant or other surface contamination (Section 1.2). In Figure 3.4 (b), many features are over 50 nm across, and often form clusters which sometimes follow curved lines across the network; these patterns give a strong indication that nanodiscs are attaching to the carbon nanotubes.

### 3.2. Aqueous Sensing of Ethyl Hexanoate with OR22a-functionalised Carbon Nanotube Transistor

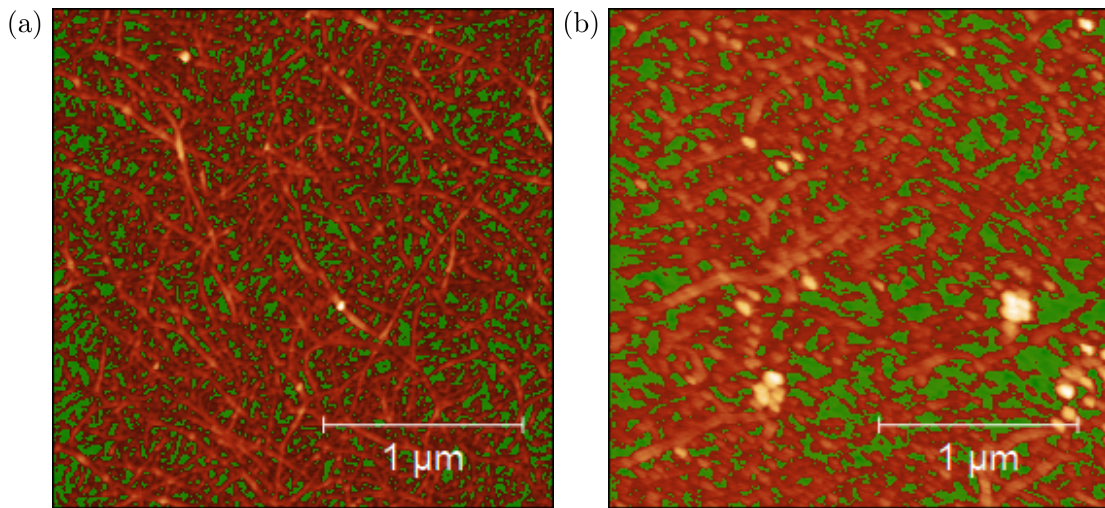


Figure 3.3.: Atomic force microscope images with the substrate background highlighted with a green mask. Here, (a) shows a device channel after functionalisation with PBASE and methanol, while (b) shows channel 7 from the sensing device functionalised with OR22a nanodiscs in this section.

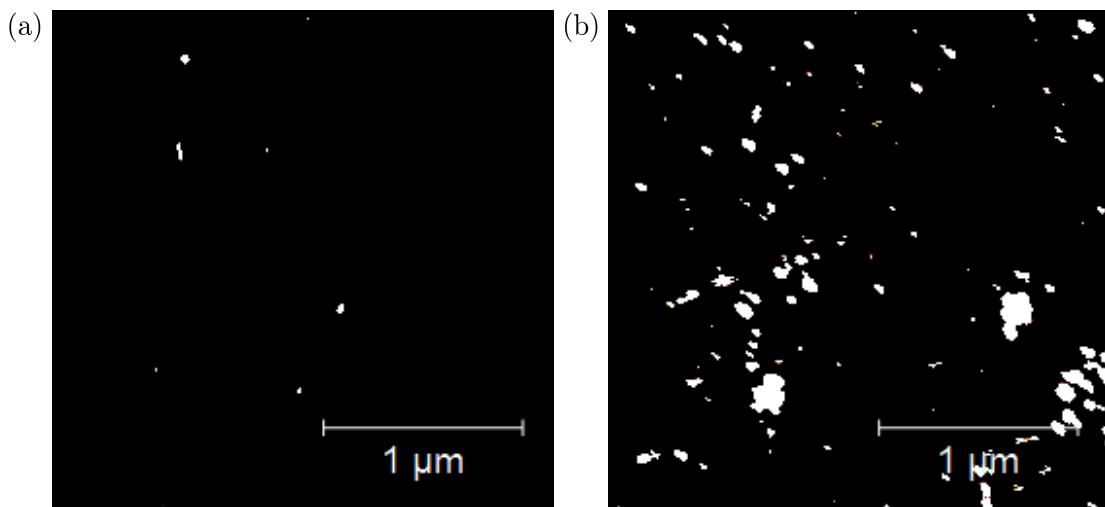


Figure 3.4.: Binary representations of the atomic force microscope images of (a) the pristine device, with a threshold height of 11.2 nm, and (b) the functionalised device, with a threshold height of 12 nm. Both thresholds are 8.7 nm above the substrate background of their respective images.

### *3. Biosensing with Insect Odorant-Receptor Functionalised Carbon Nanotube Devices*

As the maximum height of the functionalised AFM is 25.9 nm and only nanodisc features are present at 12.0 nm, there must be nanodisc agglomerates present at least 13.9 nm tall. The estimated height range for nanodisks is  $\sim 10 - 20$  nm [76], [156], [157]. Assuming a average carbon nanotube height of 1.45 nm, with a average substrate height of 3.3 nm, the nanodisc agglomerations could be up to  $\sim 21$  nm tall. Note that height measurements of biological samples taken via AFM have been shown to underestimate actual feature height by over 50% [12]. Even so, the breadths of the nanodisc features are significantly greater than their heights. While the cross-sections of the largest features are up to 20 nanodisks across, they are a few nanodisks high at most; certainly less than five. It appears that, rather than clustering together in solution and attaching as an aggregate, the nanodisks are individually attaching to preferred locations on the network. These locations may be at junctions between two large carbon nanotubes, which have a relatively large surface area available for binding, or at locations particularly clean of contamination. AFM images showing iOR-nanodisk functionalised carbon nanotube networks with significant vertical clustering have been reported, but these images were not of channels used for sensing [75].

#### **3.2.2. Aqueous Sensing of Ethyl Hexanoate**

The procedure used for biosensor detection of ethyl hexanoate in liquid was the same as the procedure outlined in Section 1.4, except 0.5% DMSO was present in the buffer solution (to improve ethyl hexanoate solubility) and dilutions of ethyl hexanoate in the same 0.5% DMSO 1XPBS buffer solution were added during the sensing series. The 0.5% DMSO 1XPBS was prepared by adding 5  $\mu$ L of DMSO to 995  $\mu$ L 1XPBS before device characterisation. The dilutions of ethyl hexanoate were prepared with the same 1XPBS at the same time, where 5  $\mu$ L of 200 fM, 200 pM, 200 nM and 200  $\mu$ M ethyl hexanoate in DMSO were placed into four individual vials containing 995  $\mu$ L 1XPBS each, giving 1mL vials of 1 fM, 1 pM, 1 nM and 1  $\mu$ M ethyl hexanoate in 0.5% DMSO 1XPBS. The ethyl hexanoate in DMSO dilutions were prepared beforehand as a 1:10 dilution series in DMSO using 200 mM stock solution, where dilutions ranged from 20 mM to 200 fM. Sampling measurements were taken using the B1500A semiconductor device analyser, with the transfer measurement in Figure 3.1 (b) taken directly before sensing. The full control series plus sensing sequence is shown in Figure 3.5. Gate current remained negligible across the entire sensing procedure.

The control series for the sensing series is shown in Figure 3.6 (a). No clear stepwise response is seen to buffer additions or subtractions. The functionalised device shows similar baseline drift behaviour to that of a pristine device, with a period of short-term decay quickly yielding to a more long-lived decay behaviour. A linear fit  $I = c_1 t + c_2$  to the region 1200 – 1800 had a gradient of  $c_1 = -1.76 \pm 0.02$  pA/s. This gradient is smaller than the range of values found for the linear fit approximating the longer-term drift of a pristine device (Section 1.4.1), but of the same order of magnitude. The linear fit was then subtracted from the control series and an exponential fit  $I = I_0 \exp(-t/\tau)$

### 3.2. Aqueous Sensing of Ethyl Hexanoate with OR22a-functionalised Carbon Nanotube Transistor

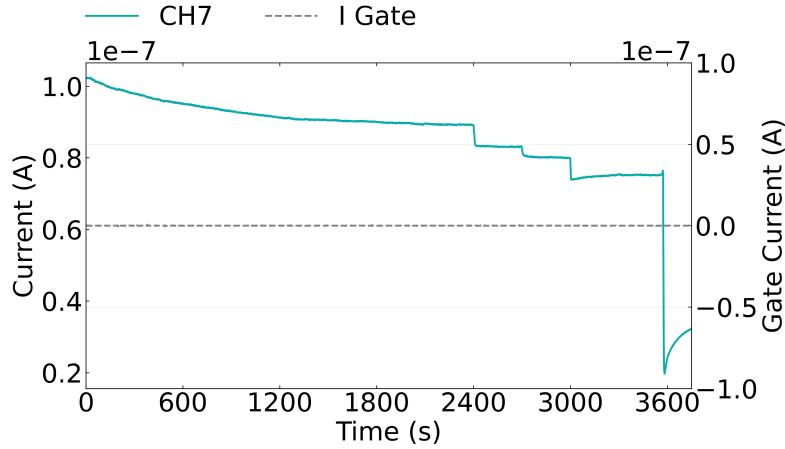


Figure 3.5.: The control series (before 1800 s) and ethyl hexanoate sensing series (after 1800 s) of the OR22a-functionalised device channel. No responses to 0.5% DMSO 1XPBS were seen during the control series, while significant responses to additions of ethyl hexanoate diluted in 0.5% DMSO 1XPBS were seen at 2400 s, 2700 s, 3000 s and 3600 s.

was performed on the remaining dataset, as shown in Figure 3.6 (b). A value of  $590 \pm 3$  s was found for the exponential time constant, similar to those found for the channels of the pristine device. This confirms that the 1800 s control series is sufficient to avoid the presence of short-term decay during sensing.

It appears that the exponential fit overestimates current measurements between 1100 s and 1500 s and underestimates between 1500 s and 1800 s. This deviation from the fit may result from the linear approximation used to represent long-term baseline drift being weaker for this channel than for those discussed previously in Section 1.4 and Section 1.5. This could result from the exponential terms for long-term baseline drift having relatively short time constants, so  $t \ll \tau_i$  no longer holds and higher order terms in the linear approximation are no longer negligible. This observation may indicate a relationship exists between device functionalisation and the long-lived device decay behaviour. However, it may simply result from the natural variation between randomly-deposited device channels. Further work may be required to confirm the existence of such a relationship, though this work is outside the scope of this thesis.

Figure 3.7 (a) shows the cleaned and filtered ethyl hexanoate sensing data from the OR22a-functionalised device from 1800 s onwards. The concentration of each 20  $\mu\text{L}$  addition is indicated above the corresponding addition time. The source-drain current across the channel decreased rapidly with each addition of ethyl hexanoate in 0.5 DMSO 1XPBS solution. This current decrease appears irreversible, as the current stabilises after each addition at a lower current level than prior to the addition. This behaviour appears to be a response by OR22a to its positive ligand ethyl hexanoate, similar to the response by OR22a to methyl hexanoate seen by Murugathas *et al.*. The presence of the ORCO

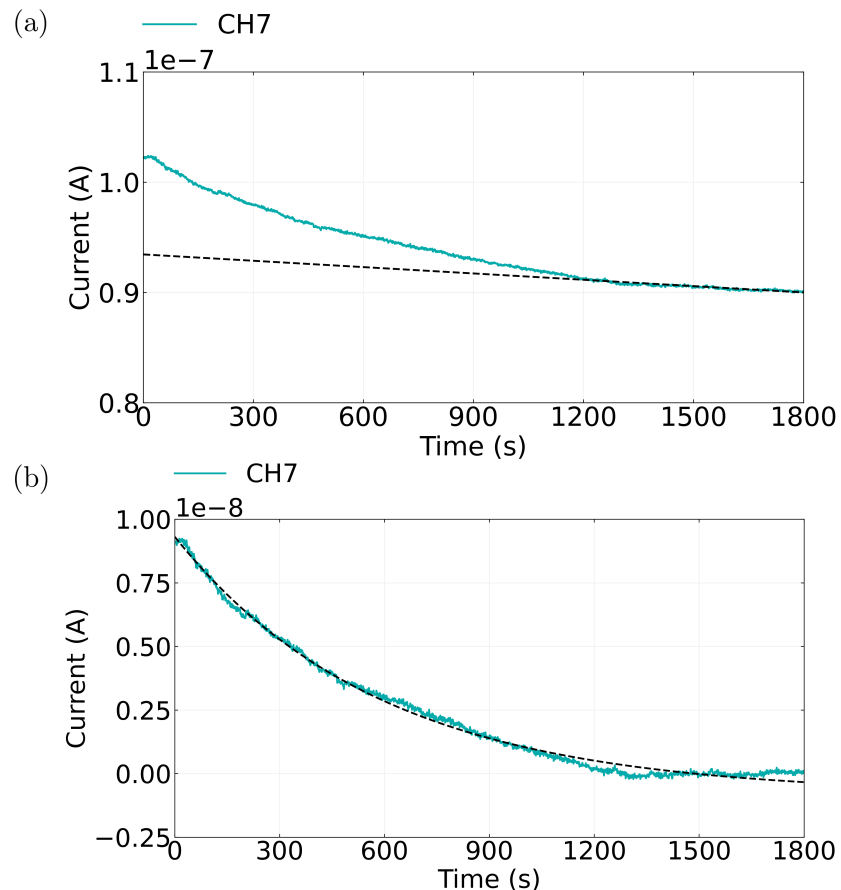


Figure 3.6.: The control series for the OR22a-functionalised device is shown in (a), alongside an extrapolated linear fit to the control series from 1200 s onwards. The control series with the linear approximation subtracted fitted to an exponential curve is shown in (b).

3.2. Aqueous Sensing of Ethyl Hexanoate with OR22a-functionalised Carbon Nanotube Transistor

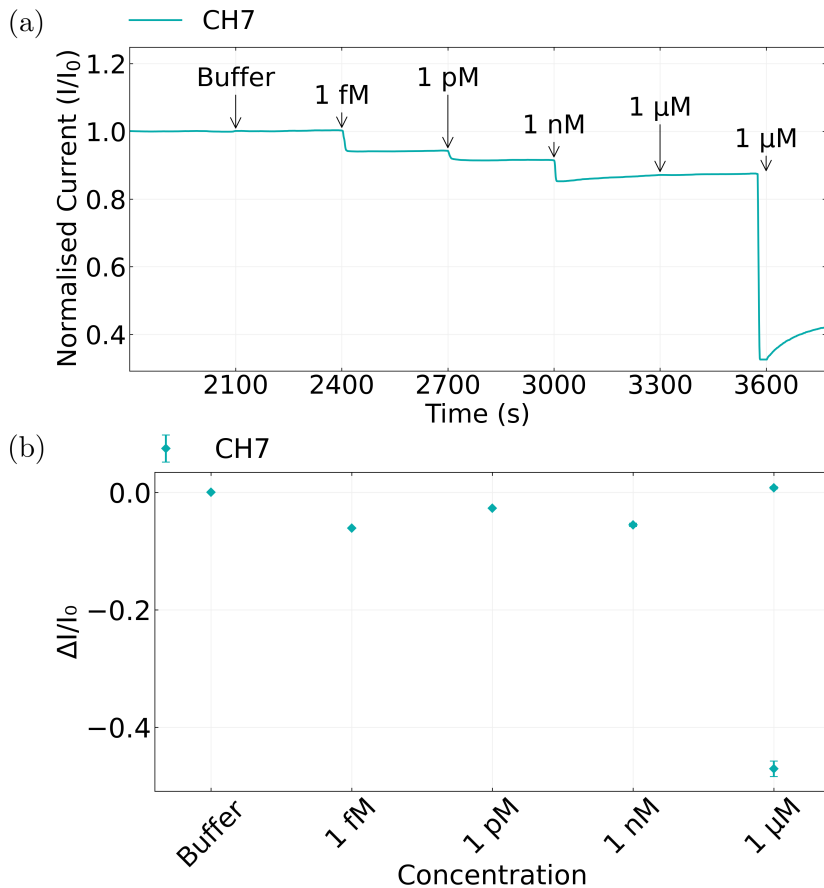


Figure 3.7.: The normalised sensing series for the OR22a-functionalised device is shown in (a). The current data has been despiked, with baseline drift removed and a moving median filter applied. The concentration of each  $20 \mu\text{L}$  addition is indicated above the time of addition. The signal data corresponding to the mean difference in current before and after each addition is shown in (b).

### 3. Biosensing with Insect Odorant-Receptor Functionalised Carbon Nanotube Devices

coreceptor was not required for responses to be seen. The device showed responses to ethyl hexanoate over a wide range of concentrations, beginning with a  $\sim 6\%$  response to 1 fM EtHex in 0.5 DMSO 1XPBS, while showing no response to 0.5% 1XPBS buffer. Interestingly, as seen in Figure 3.7 (b), no clear dose-dependent response was observed. The behaviour seen may be explained by a decreased sensitivity to subsequent additions seen by Murugathas *et al.* [75] competing with the logarithmic increases in the concentration around the channel.

### 3.3. Variability in Biosensor Behaviour

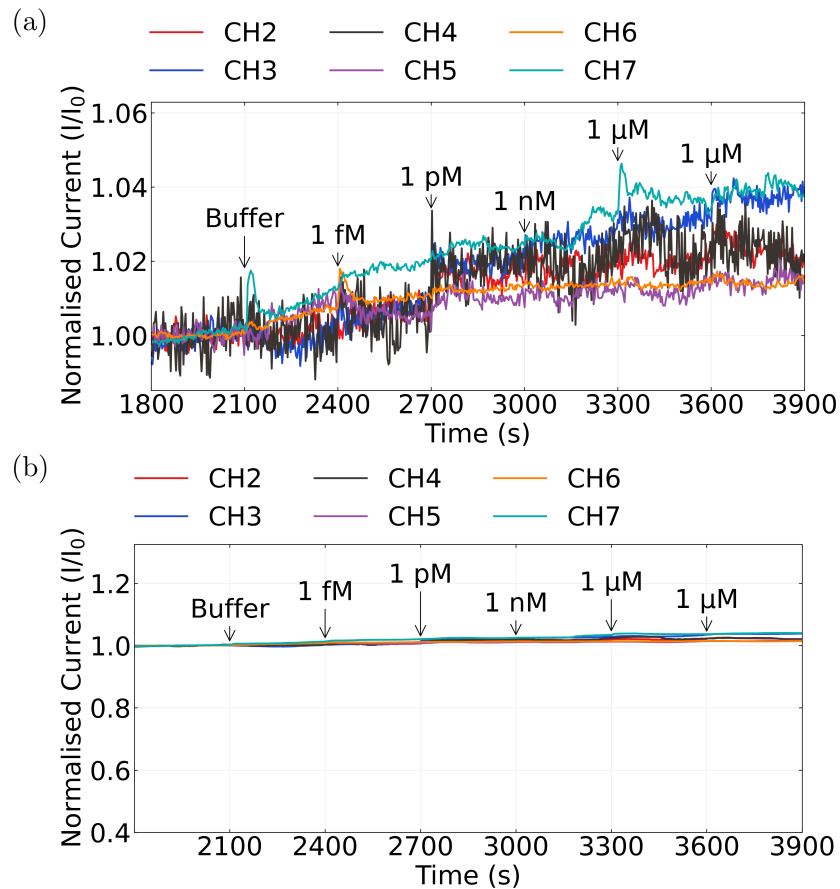


Figure 3.8.: The normalised sensing series of another OR22a-functionalised device across six multiplexed channels, where current data has been despiked and baseline drift removed. The concentration of each 20  $\mu\text{L}$  addition is indicated above the time of addition. The same sensing series is shown in both (a) and (b), where a moving median filter has been applied in (b).

Despite the successful detection of ethyl hexanoate by an OR22a nanodisc-functionalised

### 3.3. Variability in Biosensor Behaviour

biosensor in Section 3.2, it was found that this behaviour was not readily reproducible. The results from the previous section were not repeated when using the same procedure for fabrication of devices alongside an identical functionalisation process with the same batch of OR22a nanodiscs (ND-OR22a-SB018). The ethyl hexanoate sensing sequence from six functionalised device channels is shown in Figure 3.8. Figure 3.8 (a) has been left unfiltered to illustrate the variation in behaviour between channels, while Figure 3.8 (b) has been prepared in the same manner as Figure 3.7 (a). The current response to each analyte addition is similar to that seen after the initial addition without ethyl hexanoate present. The largest contributing factor to current change appears to be drift. Unlike the clear decreases in current subsequent to ethyl hexanoate additions seen in Figure 3.7 (a), no decreases are seen in Figure 3.8 (b) to any ethyl hexanoate solution addition.

Liquid-gated electrical characteristics were taken of each sensing channel from this device before and after functionalisation with OR22a, in the same manner as Section 3.2. These characteristics are shown in Figure 3.9. The average threshold shift was  $-0.06 \pm 0.02$ , the same as that of a device functionalised with PBASE in methanol without subsequent functionalisation with OR22a nanodiscs. To test whether protein was present on the channel, an atomic force microscope image was taken of channel 6, as shown in Figure 3.10. The same image analysis as in Section 3.2 was performed, with the substrate mask shown in Figure 3.11 (a) giving an average substrate height of  $3.8 \pm 0.4$ . A binary representation of the image with a 12.5 nm threshold, 8.7 nm above the average substrate height, is shown in Figure 3.11 (b). As with the functionalised device in Figure 3.4 (b), Figure 3.11 (b) shows clustering of features, many of which are larger than 50 nm across. It seems, therefore, that nanodisc aggregates up to 27.5 nm high are present on channel 6, despite the lack of a significant threshold shift as a result of functionalisation.

Both OR nanodisc and empty nanodisc attachment via PBASE have been shown to cause significant gating of the network (Section 3.2). Therefore, it might be reasoned that the lack of a gating effect, but with nanodiscs present, results from a direct attachment mechanism circumventing the PBASE linker. The amine group on proteins can be attached directly onto carbon nanotubes by adsorption, although this attachment is relatively weak [155]. **OR22a-noPBASE-AFM** shows an AFM image of a carbon nanotube network film after submersion in a 10 L/mL OR22a nanodisc in PBS solution for 1 hour (batch NDOR22a-0016-1), without prior exposure to PBASE in methanol. Figure 3.13 shows the substrate mask in (a) and a binary representation of this AFM with nanodisc aggregates clearly visible in (b). In Figure 3.14 (a), the negative threshold shift of a channel modified in this way was -0.27 V, similar in size to the shift due to functionalisation seen for the working biosensor. However, this device channel did not work as a sensor when tested with ethyl hexanoate. Figure 3.14 (b) shows a small, positive current response to additions of ethyl hexanoate diluted in 1% DMSO 1XPBS, which may result from the weakly attached OR22a nanodiscs being mechanically removed by the pressure of each addition on the device channels.

An explanation is required for the seemingly contradictory situation where nanodiscs can be present on a device channel without significant gating effects. The most straight-

### 3. Biosensing with Insect Odorant-Receptor Functionalised Carbon Nanotube Devices

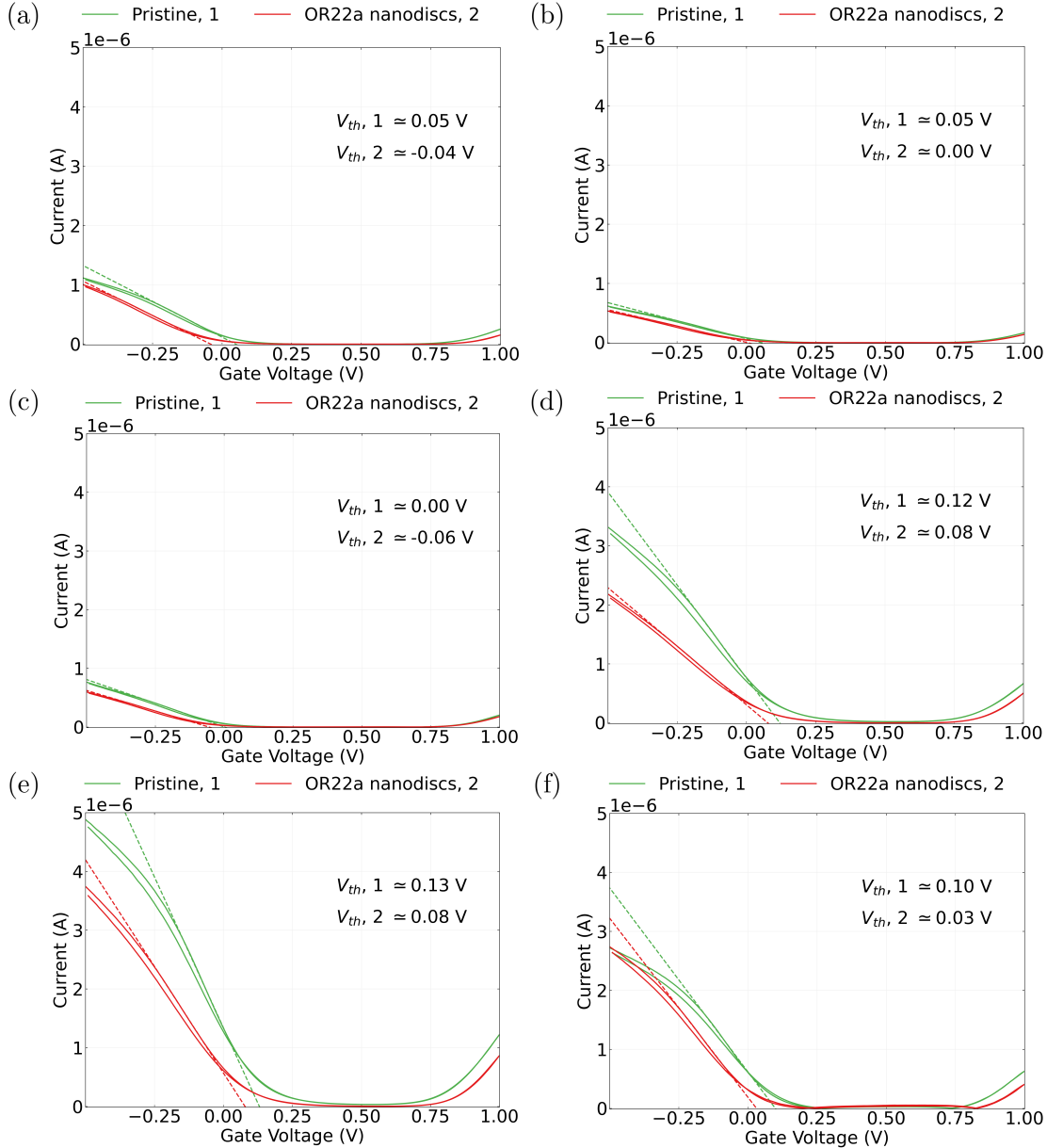


Figure 3.9.: Liquid-gated carbon nanotube network device transfer characteristics before and after OR22a nanodisc functionalisation. Each subfigure (a)-(f) corresponds to a different channel of the functionalised device; (a) corresponds to channel 2, (b) corresponds to channel 3, (c) corresponds to channel 4, (d) corresponds to channel 5, (e) corresponds to channel 6 and (f) corresponds to channel 7. The dashed line shown is tangent to the subthreshold slope of the characteristic curve. The threshold voltage corresponding to the intercept of this slope with the x-axis is shown for each transfer characteristic curve.

### 3.3. Variability in Biosensor Behaviour

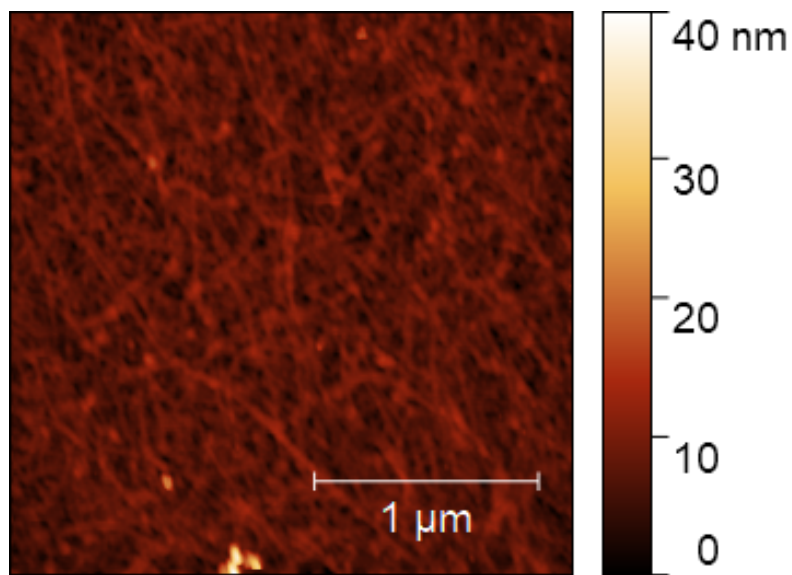


Figure 3.10.: An atomic force microscope image of channel 6 from the OR22a nanodisc functionalised device which showed no response to ethyl hexanoate.

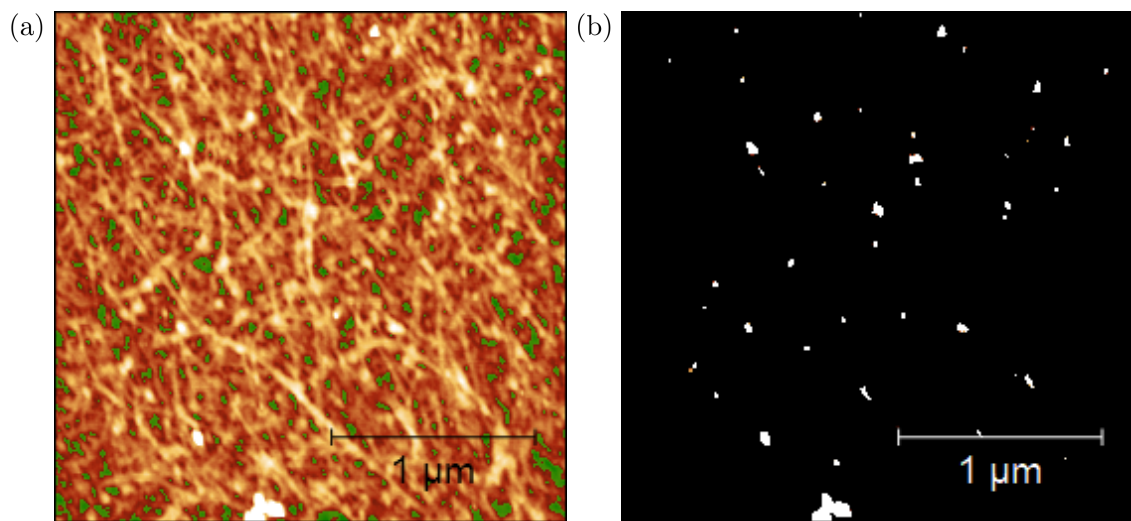


Figure 3.11.: The mask used to find the average substrate height of the functionalised channel 6 is shown in (a), with the substrate highlighted green. The bounds of the colour map have been lowered in (a), as colour mapping over the full height range makes it difficult to clearly distinguish between sub-20 nm features and the substrate. A binary representation of the atomic force microscope image with a threshold height of 12.5 nm is shown in (b).

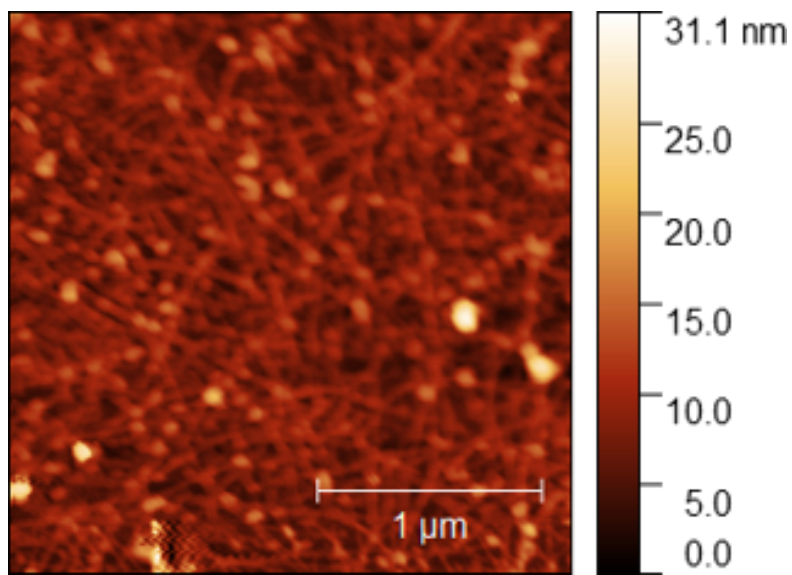


Figure 3.12.: An atomic force microscope image of a carbon nanotube film submerged in OR22a nanodiscs for 1 hour without prior exposure to PBASE or methanol.

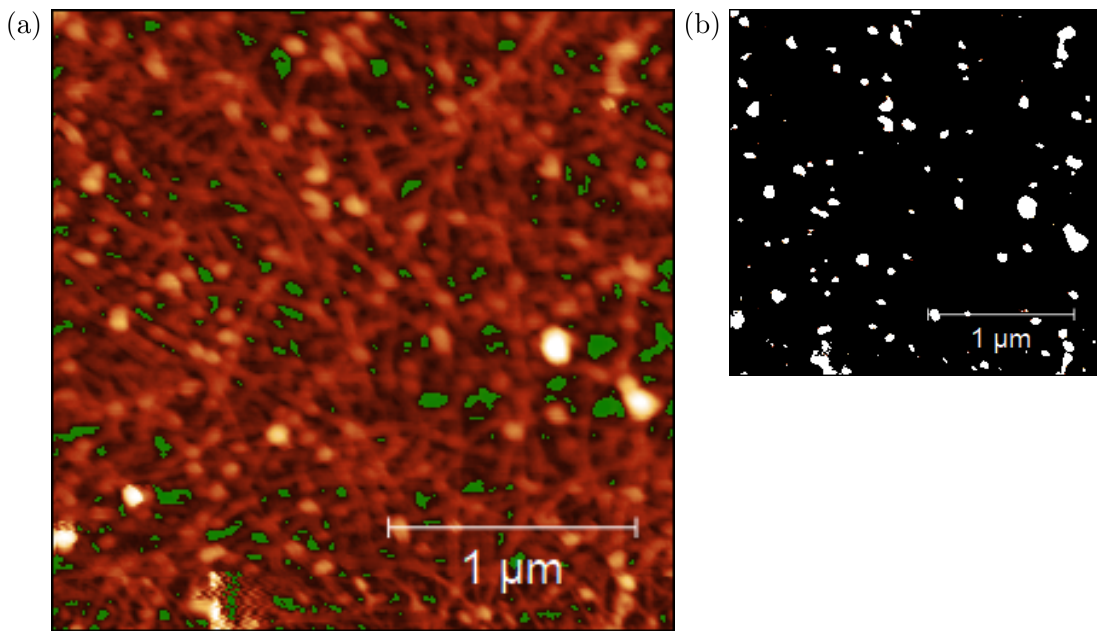


Figure 3.13.: The binary representation of the network, with a height threshold of 12.8 nm (average substrate height = 4.1 nm), is shown in (b).

### 3.4. Potential Sources of Variability

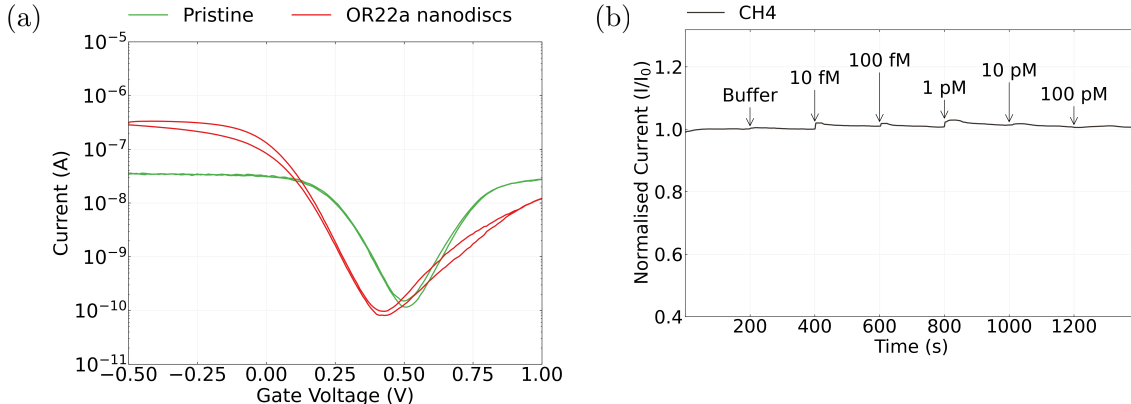


Figure 3.14.: The device characteristics in (a) are from channel 4 of the device placed in OR22a nanodisc solution for 1 hour without prior exposure to PBASE or methanol before and after functionalisation. Real-time sampling using this channel is shown in (b). A 20  $\mu$ L addition of 1% DMSO 1XPBS was made at 200 s. Subsequently, 20  $\mu$ L additions of ethyl hexanoate diluted in 1% DMSO 1XPBS were made at 400 s, 600 s, 800 s and 1000 s and 1200 s, with the concentration of each addition indicated above the time of addition.

forward explanation is that no reliable correlation exist between the two phenomena. Given the consistent threshold shift results for various linker functionalisations seen in Chapter 2, this scenario implies a significant variation in protein structure and charge behaviour within a single nanodisc batch, which seems unlikely. Another possibility is that some type of surface coating is causing nanodiscs to not attach to either PBASE or the carbon nanotubes. This surface coating might be attractive, attaching to both nanodiscs and carbon nanotubes, but forming a barrier layer between the two. Alternatively, this coating might be repulsive, causing nanodiscs to attach weakly to the substrate around the carbon nanotubes. Variations in the degree to which a network is coated may then explain why the same functionalisation method might work for one device but not another. The following section investigates ways of eliminating possible sources of surface coating for more reliable functionalisation results.

## 3.4. Potential Sources of Variability

Throughout the course of this thesis, multiple potential candidates for the unwanted surface coating discussed in the previous section have been identified. These include the surfactant used in carbon nanotube deposition (Section 1.2, Section 1.3) and the solvent used in functionalisation (Section 2.3.3). Another possibility is that PBASE itself is acting as a surface coating, which could result from multilayer coverage restricting access to directly attached PBASE (Section 2.3.1). Alternatively, PBASE may have hydrolysed

### *3. Biosensing with Insect Odorant-Receptor Functionalised Carbon Nanotube Devices*

into PBA prior to attachment, forming an inert surface layer upon -stacking around the carbon nanotubes. However, no threshold shift directly attributable to PBA attachment should occur (Section 2.4.3), and this is not what was observed when characterising the non-working device in Section 3.3. To understand which of these candidates is responsible for the significant variability in biosensor functionality, the sensing procedure was performed with slight variations on the biosensor fabrication and functionalisation procedures. In each test, an individual element of one of these procedures was altered to prevent the introduction of a specific surface coating. The biosensor was then characterised and tested to see if it would respond to its target ligand.

#### **3.4.1. Surfactant Contamination**

**Varying CNT network deposition approach**

**Functionalisation of Graphene Devices**

#### **3.4.2. Aggregation of Odorant Receptor Nanodiscs**

#### **3.4.3. Solvent Contamination**

### **3.5. Other Sources of Variability**

### **3.6. Vapour Sensing with Empty Nanodiscs**

### **3.7. Conclusion**

## A. Vapour System Hardware

Table A.1.: Major components used in construction of the vapour delivery system described in this thesis.

Description	Part No.	Manufacturer
Mass flow controller, 20 sccm full scale	GE50A013201SBV020	MKS Instruments
Mass flow controller, 200 sccm full scale	GE50A013202SBV020	MKS Instruments
Mass flow controller, 500 sccm full scale	FC-2901V	Tylan
Analogue flowmeter, 240 sccm max. flow	116261-30	Dwyer
Micro diaphragm pump	P200-B3C5V-35000	Xavitech
Analogue flow controller, for micro diaphragm pump	X3000450	Xavitech
10 mL Schott bottle	218010802	Duran
PTFE connection cap system	Z742273	Duran
Baseline VOC-TRAQ flow cell, red	043-951	Mocon
Humidity and temperature sensor	T9602	Telaire
Enclosure, for humidity and temperature sensor	MC001189	Multicomp Pro



## B. Python Code for Data Analysis

### B.1. Code Repository

The code used for general analysis of field-effect transistor devices in this thesis was written with Python 3.8.8. Contributors to the code used include Erica Cassie, Erica Happe, Marissa Dierkes and Leo Browning. The code is located on GitHub and the research group OneDrive, and is available on request.

### B.2. Atomic Force Microscope Histogram Analysis

The purpose of this code is to analyse atomic force microscope (AFM) images of carbon nanotube networks in .xyz format taken using an atomic force microscope and processed in Gwyddion (see [?@sec-afm-characterisation](#)). It was originally designed by Erica Happe in Matlab, and adapted by Marissa Dierkes and myself for use in Python. The code imports the .xyz data and sorts it into bins 0.15 nm in size for processing. To perform skew-normal distribution fits, both *scipy.optimize.curve\_fit* and *scipy.stats.skewnorm* modules are used in this code.

### B.3. Raman Spectroscopy Analysis

The purpose of this code is to analyse a series of Raman spectra taken at different points on a single film (see [?@sec-raman-characterisation](#)). Data is imported in a series of tab-delimited text files, with the low wavenumber spectrum ( $100\text{ cm}^{-1} - 650\text{ cm}^{-1}$ ) and high wavenumber spectrum ( $1300\text{ cm}^{-1} - 1650\text{ cm}^{-1}$ ) imported in separate datafiles for each scan location.

### B.4. Field-Effect Transistor Analysis

The purpose of this code is to analyse electrical measurements taken of field-effect transistor (FET) devices. Electrical measurements were either taken from the Keysight 4156C Semiconductor Parameter Analyser, National Instruments NI-PXIe or Keysight B1500A Semiconductor Device Analyser as discussed in [?@sec-electrical-characterisation](#);

### *B. Python Code for Data Analysis*

the code is able to analyse data in .csv format taken from all three measurement setups. The main Python file in the code base consists of three related but independent modules: the first analyses and plots sensing data from the FET devices, the second analyses and plots transfer characteristics from channels across a device, and the third compares individual channel characteristics before and after a modification or after each of several modifications. The code base also features a separate config file and style sheet which govern the behaviour of the main code. The code base was designed collaboratively by myself and Erica Cassie over GitHub using the Sourcetree Git GUI.

# Bibliography

- [1] H. Y. Zheng and N. O.V. Plank. “Facile fabrication of carbon nanotube network thin film transistors for device platforms”. In: *International Journal of Nanotechnology* 14.1-6 (2017), pp. 505–518. ISSN: 14757435. DOI: 10.1504/IJNT.2017.082473.
- [2] Thanihaichelvan Murugathas, Leo A. Browning, Marissa P. Dierkes, et al. “Data on liquid gated CNT network FETs on flexible substrates”. In: *Data in Brief* 21 (Dec. 2018), pp. 276–283. ISSN: 2352-3409. DOI: 10.1016/J.DIB.2018.09.093.
- [3] Thanihaichelvan Murugathas, Leo A. Browning, Marissa P. Dierkes, et al. “Metallic-semiconducting junctions create sensing hot-spots in carbon nanotube FET aptasensors near percolation”. In: *Biosensors and Bioelectronics* 130 (Apr. 2019), pp. 408–413. ISSN: 0956-5663. DOI: 10.1016/J.BIOS.2018.09.021.
- [4] Hong Phan T. Nguyen, Thanihaichelvan Murugathas, and Natalie O.V. Plank. “Comparison of Duplex and Quadruplex Folding Structure Adenosine Aptamers for Carbon Nanotube Field Effect Transistor Aptasensors”. In: *Nanomaterials (Basel, Switzerland)* 11.9 (Sept. 2021). ISSN: 2079-4991. DOI: 10.3390/NANO11092280. URL: <https://pubmed.ncbi.nlm.nih.gov/34578596/>.
- [5] Wim Wenseleers, Igor L. Vlasov, Etienne Goovaerts, et al. “Efficient Isolation and Solubilization of Pristine Single-Walled Nanotubes in Bile Salt Micelles”. In: *Advanced Functional Materials* 14.11 (Nov. 2004), pp. 1105–1112. ISSN: 1616-3028. DOI: 10.1002/ADFM.200400130. URL: <https://onlinelibrary.wiley.com/doi/full/10.1002/adfm.200400130%20https://onlinelibrary.wiley.com/doi/abs/10.1002/adfm.200400130%20https://onlinelibrary.wiley.com/doi/10.1002/adfm.200400130>.
- [6] Gildas Gavrel, Bruno Jousselme, Arianna Filoromo, et al. “Supramolecular Chemistry of Carbon Nanotubes”. In: (2013), pp. 95–126. DOI: 10.1007/128\_2013\_450.
- [7] Greg T. Hermanson. “Buckyballs, Fullerenes, and Carbon Nanotubes”. In: *Bioconjugate Techniques* (Jan. 2013), pp. 741–755. DOI: 10.1016/B978-0-12-382239-0.00016-9.
- [8] Maki Shimizu, Shunjiro Fujii, Takeshi Tanaka, et al. “Effects of surfactants on the electronic transport properties of thin-film transistors of single-wall carbon nanotubes”. In: *Journal of Physical Chemistry C* 117.22 (June 2013), pp. 11744–11749. ISSN: 19327455. DOI: 10.1021/JP3113254/SUPPL\_FILE/JP3113254\_SI\_001.PDF. URL: <https://pubs.acs.org/doi/full/10.1021/jp3113254>.

## Bibliography

- [9] Antonello Di Crescenzo, Valeria Ettorre, and Antonella Fontana. “Non-covalent and reversible functionalization of carbon nanotubes”. In: *Beilstein Journal of Nanotechnology* 5.1 (2014), p. 1675. ISSN: 21904286. DOI: 10.3762/BJNANO.5.178. URL: /pmc/articles/PMC4222398/%20/pmc/articles/PMC4222398/?report=abstract % 20https://www.ncbi.nlm.nih.gov/pmc/articles/PMC4222398/.
- [10] Melburne C. LeMieux, Mark Roberts, Soumendra Barman, et al. “Self-sorted, aligned nanotube networks for thin-film transistors”. In: *Science* 321.5885 (July 2008), pp. 101–104. ISSN: 00368075. DOI: 10.1126/SCIENCE.1156588. URL: https://www.science.org.
- [11] Chang Liu and Hui Ming Cheng. “Carbon nanotubes: controlled growth and application”. In: *Materials Today* 16.1-2 (Jan. 2013), pp. 19–28. ISSN: 1369-7021. DOI: 10.1016/J.MATTOD.2013.01.019.
- [12] Dusan Vobornik, Maohui Chen, Shan Zou, et al. “Measuring the Diameter of Single-Wall Carbon Nanotubes Using AFM”. In: *Nanomaterials* 13.3 (Feb. 2023), p. 477. ISSN: 20794991. DOI: 10.3390/NANO13030477. URL: https://www.mdpi.com/2079-4991/13/3/477/htm%20https://www.mdpi.com/2079-4991/13/3/477.
- [13] A. Azzalini and A. Capitanio. “Statistical applications of the multivariate skew normal distribution”. In: *Journal of the Royal Statistical Society Series B* 61.3 (1999), pp. 579–602. ISSN: 13697412. DOI: 10.1111/1467-9868.00194. arXiv: 0911.2093. URL: https://ideas.repec.org/a/bla/jorssb/v61y1999i3p579-602.html%20https://ideas.repec.org//a/bla/jorssb/v61y1999i3p579-602.html.
- [14] Matěj Velický, Adam J Cooper, Peter S Toth, et al. “Mechanical stability of substrate-bound graphene in contact with aqueous solutions”. In: *2D Materials* 2.2 (May 2015), p. 024011. ISSN: 2053-1583. DOI: 10.1088/2053-1583/2/2/024011. URL: https://iopscience.iop.org/article/10.1088/2053-1583/2/2/024011%20https://iopscience.iop.org/article/10.1088/2053-1583/2/2/024011/meta.
- [15] Erin E. Christensen, Mitesh Amin, Trevor M. Tumiel, et al. “Localized Charge on Surfactant-Wrapped Single-Walled Carbon Nanotubes”. In: *Journal of Physical Chemistry Letters* 13.46 (Nov. 2022), pp. 10705–10712. ISSN: 19487185. DOI: 10.1021/ACS.JPCLETT.2C02650. URL: https://pubs.acs.org/doi/full/10.1021/acs.jpclett.2c02650.
- [16] R. L. Graham, B. D. Lubachevsky, K. J. Nurmela, et al. “Dense packings of congruent circles in a circle”. In: *Discrete Mathematics* 181.1-3 (Feb. 1998), pp. 139–154. ISSN: 0012-365X. DOI: 10.1016/S0012-365X(97)00050-2.
- [17] Eckard Specht. *The best known packings of equal circles in a circle*. URL: http://hydra.nat.uni-magdeburg.de/packing/cci/cci.html (visited on 2023-09-11).

- [18] Robert D. Deegan, Olgica Bakajin, Todd F. Dupont, et al. “Capillary flow as the cause of ring stains from dried liquid drops”. In: *Nature* 1997 389:6653 389.6653 (1997), pp. 827–829. ISSN: 1476-4687. DOI: 10.1038/39827. URL: <https://www.nature.com/articles/39827>.
- [19] R. T. van Gaalen, C. Diddens, H. M.A. Wijshoff, et al. “Marangoni circulation in evaporating droplets in the presence of soluble surfactants”. In: *Journal of Colloid and Interface Science* 584 (Feb. 2021), pp. 622–633. ISSN: 0021-9797. DOI: 10.1016/J.JCIS.2020.10.057.
- [20] Mindy D. Bishop, Gage Hills, Tathagata Srimani, et al. “Fabrication of carbon nanotube field-effect transistors in commercial silicon manufacturing facilities”. In: *Nature Electronics* 2020 3:8 3.8 (June 2020), pp. 492–501. ISSN: 2520-1131. DOI: 10.1038/s41928-020-0419-7. URL: <https://www.nature.com/articles/s41928-020-0419-7>.
- [21] Yulia V Marchenko and Marc G Genton. “A suite of commands for fitting the skew-normal and skew-t models”. In: *The Stata Journal* 10.4 (2010), pp. 507–539.
- [22] Alexander A. Kane, Alexandra C. Ford, April Nissen, et al. “Etching of surfactant from solution-processed, type-separated carbon nanotubes and impact on device behavior”. In: *ACS Nano* 8.3 (Mar. 2014), pp. 2477–2485. ISSN: 1936086X. DOI: 10.1021/NN406065T. URL: <https://pubs.acs.org/doi/full/10.1021/nn406065t>.
- [23] Millie S. Dresselhaus, G. Dresselhaus, R. Saito, et al. “Raman spectroscopy of carbon nanotubes”. In: *Physics Reports* 409.2 (Mar. 2005), pp. 47–99. ISSN: 0370-1573. DOI: 10.1016/J.PHYSREP.2004.10.006.
- [24] Benjamin King and Balaji Panchapakesan. “Vacuum filtration based formation of liquid crystal films of semiconducting carbon nanotubes and high performance transistor devices”. In: *Nanotechnology* 25.17 (Apr. 2014), p. 175201. ISSN: 0957-4484. DOI: 10.1088/0957-4484/25/17/175201. URL: <https://iopscience.iop.org/article/10.1088/0957-4484/25/17/175201%20https://iopscience.iop.org/article/10.1088/0957-4484/25/17/175201/meta>.
- [25] M. Świniański, A. Dużyńska, A. P. Gertych, et al. “Determination of the electronic transport in type separated carbon nanotubes thin films doped with gold nanocrystals”. In: *Scientific Reports* 2021 11:1 11.1 (Aug. 2021), pp. 1–7. ISSN: 2045-2322. DOI: 10.1038/s41598-021-96307-6. URL: <https://www.nature.com/articles/s41598-021-96307-6>.
- [26] David C. Stone. “Application of median filtering to noisy data”. In: 73.10 (Oct. 2011), pp. 1573–1581. ISSN: 0008-4042. DOI: 10.1139/V95-195. URL: <https://cdnsciencepub.com/doi/10.1139/v95-195>.
- [27] Douglas R. Kauffman and Alexander Star. “Electronically monitoring biological interactions with carbon nanotube field-effect transistors”. In: *Chemical Society Reviews* 37.6 (May 2008), pp. 1197–1206. ISSN: 1460-4744. DOI: 10.1039/B709567H. URL: <https://pubs.rsc.org/en/content/articlehtml/2008/cs/>

## Bibliography

- b709567h % 20https : / / pubs . rsc . org / en / content / articlelanding / 2008 / cs / b709567h.
- [28] Iddo Heller, Jaan Mānnik, Serge G. Lemay, et al. “Optimizing the signal-to-noise ratio for biosensing with carbon nanotube transistors”. In: *Nano Letters* 9.1 (Jan. 2009), pp. 377–382. ISSN: 15306984. DOI: 10.1021/NL8031636/SUPPL\_FILE/NL8031636\_SI\_001.PDF. URL: <https://pubs.acs.org/doi/full/10.1021/nl8031636>.
  - [29] Woo Jong Yu, Un Jeong Kim, Bo Ram Kang, et al. “Adaptive Logic Circuits with Doping-Free Ambipolar Carbon Nanotube Transistors”. In: *NANO LETTERS* 9.4 (2009), pp. 1401–1405. DOI: 10.1021/nl803066v. URL: <https://pubs.acs.org/sharingguidelines>.
  - [30] Vladimir Derenskyi, Widiantha Gomulya, Jorge Mario Salazar Rios, et al. “Carbon Nanotube Network Ambipolar Field-Effect Transistors with 108 On/Off Ratio”. In: *Advanced Materials* 26.34 (Sept. 2014), pp. 5969–5975. ISSN: 15214095. DOI: 10.1002/ADMA.201401395.
  - [31] Faris M. Albarghouthi, Nicholas X. Williams, James L. Doherty, et al. “Passivation Strategies for Enhancing Solution-Gated Carbon Nanotube Field-Effect Transistor Biosensing Performance and Stability in Ionic Solutions”. In: *ACS Applied Nano Materials* 5.10 (Oct. 2022), pp. 15865–15874. ISSN: 25740970. DOI: 10.1021/ACSANM.2C04098. URL: <https://doi.org/10.1021/acsanm.2c04098>.
  - [32] Eric Pop, Sumit Dutta, David Estrada, et al. “Avalanche, Joule breakdown and hysteresis in carbon nanotube transistors”. In: *IEEE International Reliability Physics Symposium Proceedings* (2009), pp. 405–408. ISSN: 15417026. DOI: 10.1109/IRPS.2009.5173287.
  - [33] Nima Rouhi, Dheeraj Jain, Katayoun Zand, et al. “Fundamental limits on the mobility of nanotube-based semiconducting inks”. In: *Advanced Materials* 23.1 (Jan. 2011), pp. 94–99. ISSN: 09359648. DOI: 10.1002/ADMA.201003281.
  - [34] Jana Zaumseil. “Single-walled carbon nanotube networks for flexible and printed electronics”. In: *Semiconductor Science and Technology* 30.7 (June 2015), p. 074001. ISSN: 0268-1242. DOI: 10.1088/0268-1242/30/7/074001. URL: <https://iopscience.iop.org/article/10.1088/0268-1242/30/7/074001%20https://iopscience.iop.org/article/10.1088/0268-1242/30/7/074001/meta>.
  - [35] Xuan P A Gao, Gengfeng Zheng, and Charles M Lieber. “Subthreshold Regime has the Optimal Sensitivity for Nanowire FET Biosensors”. In: (2010). DOI: 10.1021/nl9034219. URL: <https://pubs.acs.org/sharingguidelines>.
  - [36] Donghun Kang, Noejung Park, Ju Hye Ko, et al. “Oxygen-induced p-type doping of a long individual single-walled carbon nanotube”. In: *Nanotechnology* 16.8 (May 2005), p. 1048. ISSN: 0957-4484. DOI: 10.1088/0957-4484/16/8/008. URL: <https://iopscience.iop.org/article/10.1088/0957-4484/16/8/008%20https://iopscience.iop.org/article/10.1088/0957-4484/16/8/008/meta>.

- [37] Iddo Heller, Anne M. Janssens, Jaan Männik, et al. “Identifying the mechanism of biosensing with carbon nanotube transistors”. In: *Nano Letters* 8.2 (Feb. 2008), pp. 591–595. ISSN: 15306984. DOI: 10.1021/NL072996I. URL: <https://pubs.acs.org/doi/full/10.1021/nl072996i>.
- [38] Yoshiyuki Nonoguchi, Atsushi Tani, Tomoko Murayama, et al. “Surfactant-driven Amphoteric Doping of Carbon Nanotubes”. In: *Chemistry - An Asian Journal* 13.24 (Dec. 2018), pp. 3942–3946. ISSN: 1861471X. DOI: 10.1002 / ASIA . 201801490.
- [39] Chris J. Barnett, Cathren E. Gowenlock, Kathryn Welsby, et al. “Spatial and Contamination-Dependent Electrical Properties of Carbon Nanotubes”. In: *Nano letters* 18.2 (Feb. 2018), pp. 695–700. ISSN: 1530-6992. DOI: 10.1021 / ACS . NANOLETT.7B03390. URL: <https://pubmed.ncbi.nlm.nih.gov/29257695/>.
- [40] Joon Sung Lee, Sunmin Ryu, Kwonjae Yoo, et al. “Origin of gate hysteresis in carbon nanotube field-effect transistors”. In: *Journal of Physical Chemistry C* 111.34 (Aug. 2007), pp. 12504–12507. ISSN: 19327447. DOI: 10.1021/JP074692Q. URL: <https://pubs.acs.org/doi/full/10.1021/jp074692q>.
- [41] Sang Won Lee, Si Young Lee, Seong Chu Lim, et al. “Positive gate bias stress instability of carbon nanotube thin film transistors”. In: *Applied Physics Letters* 101.5 (July 2012). ISSN: 00036951. DOI: 10.1063 / 1.4740084 / 111432. URL: [/aip/apl/article/101/5/053504/111432/Positive-gate-bias-stress-instability-of-carbon](https://aip.org/article/101/5/053504/111432/Positive-gate-bias-stress-instability-of-carbon).
- [42] Tae Jun Ha, Daisuke Kiriya, Kevin Chen, et al. “Highly stable hysteresis-free carbon nanotube thin-film transistors by fluorocarbon polymer encapsulation”. In: *ACS Applied Materials and Interfaces* 6.11 (June 2014), pp. 8441–8446. ISSN: 19448252. DOI: 10.1021 / AM5013326. URL: <https://pubs.acs.org/doi/full/10.1021/am5013326>.
- [43] Woong Kim, Ali Javey, Ophir Vermesh, et al. “Hysteresis Caused by Water Molecules in Carbon Nanotube Field-Effect Transistors”. In: *NANO LETTERS* 3.2 (2003), pp. 193–198. DOI: 10.1021/nl0259232.
- [44] Aaron D. Franklin, George S. Tulevski, Shu Jen Han, et al. “Variability in carbon nanotube transistors: Improving device-to-device consistency”. In: *ACS Nano* 6.2 (Feb. 2012), pp. 1109–1115. ISSN: 19360851. DOI: 10.1021/NN203516Z. URL: <https://pubs.acs.org/doi/full/10.1021/nn203516z>.
- [45] Helene Conseil, Morten S. Jellesen, and Rajan Ambat. “Experimental study of water absorption of electronic components and internal local temperature and humidity into electronic enclosure”. In: *Proceedings of the 16th Electronics Packaging Technology Conference, EPTC 2014* (Jan. 2014), pp. 355–359. DOI: 10.1109/EPTC.2014.7028356.

## Bibliography

- [46] I. Heller, S. Chattoor, J. Männik, et al. “Comparing the weak and strong gate-coupling regimes for nanotube and graphene transistors”. In: *physica status solidi (RRL) – Rapid Research Letters* 3.6 (Sept. 2009), pp. 190–192. ISSN: 1862-6270. DOI: 10.1002/PSSR.200903157. URL: <https://onlinelibrary.wiley.com/doi/full/10.1002/pssr.200903157>%20<https://onlinelibrary.wiley.com/doi/abs/10.1002/pssr.200903157>.
- [47] Iddo Heller, Sohail Chattoor, Jaan Männik, et al. “Influence of electrolyte composition on liquid-gated carbon nanotube and graphene transistors”. In: *Journal of the American Chemical Society* 132.48 (Dec. 2010), pp. 17149–17156. ISSN: 00027863. DOI: 10.1021/JA104850N/SUPPL\_FILE/JA104850N\_SI\_001.PDF. URL: <https://pubs.acs.org/doi/full/10.1021/ja104850n>.
- [48] Fengnian Xia, Damon B. Farmer, Yu Ming Lin, et al. “Graphene field-effect transistors with high on/off current ratio and large transport band gap at room temperature”. In: *Nano Letters* 10.2 (Feb. 2010), pp. 715–718. ISSN: 15306984. DOI: 10.1021/NL9039636/ASSET/IMAGES/LARGE/NL-2009-039636\_0003.JPG. URL: <https://pubs.acs.org/doi/full/10.1021/nl9039636>.
- [49] Dmitry Kireev, Max Brambach, Silke Seyock, et al. “Graphene transistors for interfacing with cells: towards a deeper understanding of liquid gating and sensitivity”. In: *Scientific Reports* 2017 7:1 7.1 (July 2017), pp. 1–12. ISSN: 2045-2322. DOI: 10.1038/s41598-017-06906-5. URL: <https://www.nature.com/articles/s41598-017-06906-5>.
- [50] Antonio Di Bartolomeo, Filippo Giubileo, Salvatore Santandrea, et al. “Charge transfer and partial pinning at the contacts as the origin of a double dip in the transfer characteristics of graphene-based field-effect transistors”. In: *Nanotechnology* 22.27 (May 2011), p. 275702. ISSN: 0957-4484. DOI: 10.1088/0957-4484/22/27/275702. URL: <https://iopscience.iop.org/article/10.1088/0957-4484/22/27/275702>%20<https://iopscience.iop.org/article/10.1088/0957-4484/22/27/275702/meta>.
- [51] Zengguang Cheng, Qiaoyu Zhou, Chenxuan Wang, et al. “Toward intrinsic graphene surfaces: A systematic study on thermal annealing and wet-chemical treatment of SiO<sub>2</sub>-supported graphene devices”. In: *Nano Letters* 11.2 (Feb. 2011), pp. 767–771. ISSN: 15306984. DOI: 10.1021/NL103977D/SUPPL\_FILE/NL103977D\_SI\_001.PDF. URL: <https://pubs.acs.org/doi/full/10.1021/nl103977d>.
- [52] Dong Wook Shin, Hyun Myoung Lee, Seong Man Yu, et al. “A facile route to recover intrinsic graphene over large scale”. In: *ACS Nano* 6.9 (Sept. 2012), pp. 7781–7788. ISSN: 19360851. DOI: 10.1021/NN3017603/SUPPL\_FILE/NN3017603\_SI\_001.PDF. URL: <https://pubs.acs.org/doi/full/10.1021/nn3017603>.
- [53] Tingting Feng, Dan Xie, Jianlong Xu, et al. “Back-gate graphene field-effect transistors with double conductance minima”. In: *Carbon* 79.1 (Nov. 2014), pp. 363–368. ISSN: 0008-6223. DOI: 10.1016/J.CARBON.2014.07.078.

- [54] Song ang Peng, Zhi Jin, Dayong Zhang, et al. “How Do Contact and Channel Contribute to the Dirac Points in Graphene Field-Effect Transistors?” In: *Advanced Electronic Materials* 4.8 (Aug. 2018), p. 1800158. ISSN: 2199-160X. DOI: 10.1002/AELM.201800158. URL: <https://onlinelibrary.wiley.com/doi/full/10.1002/aelm.201800158>
- [55] Y. Bargaoui, M. Troudi, P. Bondavalli, et al. “Gate bias stress effect in single-walled carbon nanotubes field-effect-transistors”. In: *Diamond and Related Materials* 84 (Apr. 2018), pp. 62–65. ISSN: 0925-9635. DOI: 10.1016/J.DIAMOND.2018.03.011.
- [56] Steven G. Noyce, James L. Doherty, Zhihui Cheng, et al. “Electronic Stability of Carbon Nanotube Transistors under Long-Term Bias Stress”. In: *Nano Letters* 19.3 (Mar. 2019), pp. 1460–1466. ISSN: 15306992. DOI: 10.1021/ACS.NANOLETT.8B03986. URL: <https://pubs.acs.org/doi/full/10.1021/acs.nanolett.8b03986>.
- [57] H. Lin and S. Tiwari. “Localized charge trapping due to adsorption in nanotube field-effect transistor and its field-mediated transport”. In: *Applied Physics Letters* 89.7 (Aug. 2006), p. 73507. ISSN: 00036951. DOI: 10.1063/1.2337104. URL: [/aip/apl/article/89/7/073507/332595/Localized-charge-trapping-due-to-adsorption-in](https://aip.org/article/89/7/073507/332595/Localized-charge-trapping-due-to-adsorption-in).
- [58] Sandeep Agnihotri, Mark J. Rood, and Massoud Rostam-Abadi. “Adsorption equilibrium of organic vapors on single-walled carbon nanotubes”. In: *Carbon* 43.11 (Sept. 2005), pp. 2379–2388. ISSN: 0008-6223. DOI: 10.1016/J.CARBON.2005.04.020.
- [59] Chang Young Lee and Michael S. Strano. “Understanding the dynamics of signal transduction for adsorption of gases and vapors on carbon nanotube sensors”. In: *Langmuir* 21.11 (May 2005), pp. 5192–5196. ISSN: 07437463. DOI: 10.1021/LA046867I/ASSET/IMAGES/LARGE/LA046867IF00003.JPG. URL: <https://pubs.acs.org/doi/full/10.1021/la046867i>.
- [60] Nimibofa Ayawei, Augustus Newton Ebelegi, and Donbebe Wankasi. “Modelling and Interpretation of Adsorption Isotherms”. In: *Journal of Chemistry* 2017 (2017). ISSN: 20909071. DOI: 10.1155/2017/3039817.
- [61] Mohammad Mehdi Sabzehmeidani, Sahar Mahnaee, Mehrorang Ghaedi, et al. “Carbon based materials: a review of adsorbents for inorganic and organic compounds”. In: *Materials Advances* 2.2 (Feb. 2021), pp. 598–627. ISSN: 26335409. DOI: 10.1039/D0MA00087F. URL: <https://pubs.rsc.org/en/content/articlehtml/2021/ma/d0ma00087f>
- [62] “piD-TECH® eVx User Manual 143-175 Rev 1.0”. URL: <https://www.ametekmocon.com/products/oemphotoionization/pidtechevxpathoionizationdetector>.

## Bibliography

- [63] *Technical Application Articles - Ion Science UK*. URL: <https://ionscience.com/en/gas-and-leak-detectors/customer-support/support-documents/technical-application-articles/> (visited on 2024-02-27).
- [64] Niazul I. Khan and Edward Song. “Detection of an IL-6 Biomarker Using a GFET Platform Developed with a Facile Organic Solvent-Free Aptamer Immobilization Approach”. In: *Sensors 2021, Vol. 21, Page 1335* 21.4 (Feb. 2021), p. 1335. ISSN: 1424-8220. DOI: 10.3390/S21041335. URL: <https://www.mdpi.com/1424-8220/21/4/1335>.
- [65] Bajramshahe Shkodra, Mattia Petrelli, Martina Aurora Costa Angeli, et al. “Electrolyte-gated carbon nanotube field-effect transistor-based biosensors: Principles and applications”. In: *Applied Physics Reviews* 8.4 (Dec. 2021), p. 41325. ISSN: 19319401. DOI: 10.1063/5.0058591 / 1076095. URL: [/aip/apr/article/8/4/041325/1076095/Electrolyte-gated-carbon-nanotube-field-effect](https://aip.org/article/8/4/041325/1076095/Electrolyte-gated-carbon-nanotube-field-effect).
- [66] Nikita Nekrasov, Natalya Yakunina, Averyan V. Pushkarev, et al. “Spectral-phase interferometry detection of ochratoxin a via aptamer-functionalized graphene coated glass”. In: *Nanomaterials* 11.1 (Jan. 2021), pp. 1–10. ISSN: 20794991. DOI: 10.3390/nano11010226. URL: <https://www.mdpi.com/2079-4991/11/1/226>.
- [67] Vladyslav Mishyn, Adrien Hugo, Teresa Rodrigues, et al. “The holy grail of pyrene-based surface ligands on the sensitivity of graphene-based field effect transistors”. In: *Sensors and Diagnostics* 1.2 (Mar. 2022), pp. 235–244. ISSN: 2635-0998. DOI: 10.1039/D1SD00036E. URL: [https://pubs.rsc.org/en/content/articlelanding/2022/sd/d1sd00036e](https://pubs.rsc.org/en/content/articlehtml/2022/sd/d1sd00036e).
- [68] Erica Cassie, Hamish Dunham, Erica Happe, et al. “A comparison between oestradiol aptamers as receptors in CNT FET biosensors”. In: *Sensors and Diagnostics* 2.6 (Nov. 2023), pp. 1561–1573. ISSN: 2635-0998. DOI: 10.1039/D3SD00055A. URL: [https://pubs.rsc.org/en/content/articlelanding/2023/sd/d3sd00055a](https://pubs.rsc.org/en/content/articlehtml/2023/sd/d3sd00055a).
- [69] Mitchell B. Lerner, Felipe Matsunaga, Gang Hee Han, et al. “Scalable production of highly sensitive nanosensors based on graphene functionalized with a designed G protein-coupled receptor”. In: *Nano Letters* 14.5 (May 2014), pp. 2709–2714. ISSN: 15306992. DOI: 10.1021/NL5006349/SUPPL\_FILE/NL5006349\_SI\_001. PDF. URL: <https://pubs.acs.org/doi/full/10.1021/nl5006349>.
- [70] Sae Ryun Ahn, Ji Hyun An, Seung Hwan Lee, et al. “Peptide hormone sensors using human hormone receptor-carrying nanovesicles and graphene FETs”. In: *Scientific reports* 10.1 (Dec. 2020). ISSN: 2045-2322. DOI: 10.1038/S41598-019-57339-1. URL: <https://pubmed.ncbi.nlm.nih.gov/31942024/>.

- [71] Jing Tong, Lei Zhang, Yi Wang, et al. "High response photodetection by applying the optimized photoreceptor protein modification on graphene based field effect transistors". In: *FrMat* 7 (July 2020), p. 222. ISSN: 22968016. DOI: 10.3389 / FMATS.2020.00222. URL: <https://ui.adsabs.harvard.edu/abs/2020FrMat...7.222T/abstract>.
- [72] Shiyu Wang, Md Zakir Hossain, Kazuo Shinozuka, et al. "Graphene field-effect transistor biosensor for detection of biotin with ultrahigh sensitivity and specificity". In: *Biosensors and Bioelectronics* 165 (Oct. 2020), p. 112363. ISSN: 18734235. DOI: 10.1016 / J.BIOS.2020.112363. URL: [/pmc / articles / PMC7272179 / %20 / pmc / articles / PMC7272179 / ?report = abstract % 20https : //www.ncbi.nlm.nih.gov/pmc/articles/PMC7272179 /](https://pmc.ncbi.nlm.nih.gov/pmc/articles/PMC7272179/).
- [73] Brett R. Goldsmith, Joseph J. Mitala, Jesusa Josue, et al. "Biomimetic chemical sensors using nanoelectronic readout of olfactory receptor proteins". In: *ACS Nano* 5.7 (July 2011), pp. 5408–5416. ISSN: 19360851. DOI: 10.1021 / NN200489J / SUPPL \_FILE/NN200489J \_SI \_001.PDF. URL: <https://pubs.acs.org/doi/full/10.1021/nn200489j>.
- [74] Minju Lee, Heehong Yang, Daesan Kim, et al. "Human-like smelling of a rose scent using an olfactory receptor nanodisc-based bioelectronic nose". In: *Scientific reports* 8.1 (Dec. 2018). ISSN: 2045-2322. DOI: 10.1038/S41598-018-32155-1. URL: [https://pubmed.ncbi.nlm.nih.gov/30224633 /](https://pubmed.ncbi.nlm.nih.gov/30224633/).
- [75] Thanihaichelvan Murugathas, Han Yue Zheng, Damon Colbert, et al. "Biosensing with Insect Odorant Receptor Nanodiscs and Carbon Nanotube Field-Effect Transistors". In: *ACS Applied Materials and Interfaces* 11.9 (Mar. 2019), pp. 9530–9538. ISSN: 19448252. DOI: 10.1021/ACSAM1.8B19433. URL: <https://pubs.acs.org/doi/full/10.1021/acsami.8b19433>.
- [76] Thanihaichelvan Murugathas, Cyril Hamiaux, Damon Colbert, et al. "Evaluating insect odorant receptor display formats for biosensing using graphene field effect transistors". In: *ACS Applied Electronic Materials* 2.11 (Nov. 2020), pp. 3610–3617. ISSN: 26376113. DOI: 10.1021/ACSAELM.0C00677/ASSET/IMAGES / LARGE/EL0C00677\_0006.JPG. URL: <https://pubs.acs.org/doi/full/10.1021/acsaelm.0c00677>.
- [77] Dongseok Moon, Yeon Kyung Cha, So ong Kim, et al. "FET-based nanobiosensors for the detection of smell and taste". In: *Science China. Life sciences* 63.8 (Aug. 2020), pp. 1159–1167. ISSN: 1869-1889. DOI: 10.1007/S11427-019-1571-8. URL: [https://pubmed.ncbi.nlm.nih.gov/31974862 /](https://pubmed.ncbi.nlm.nih.gov/31974862/).
- [78] Jin Yoo, Daesan Kim, Heehong Yang, et al. "Olfactory receptor-based CNT-FET sensor for the detection of DMMP as a simulant of sarin". In: *Sensors and Actuators B: Chemical* 354 (Mar. 2022), p. 131188. ISSN: 0925-4005. DOI: 10.1016/J.SNB.2021.131188.

## Bibliography

- [79] Brenda Long, Mary Manning, Micheal Burke, et al. “Non-Covalent Functionalization of Graphene Using Self-Assembly of Alkane-Amines”. In: *Advanced Functional Materials* 22.4 (Feb. 2012), pp. 717–725. ISSN: 1616-3028. DOI: 10.1002/adfm.201101956. URL: <https://onlinelibrary.wiley.com/doi/full/10.1002/adfm.201101956>%20<https://onlinelibrary.wiley.com/doi/abs/10.1002/adfm.201101956>.
- [80] Kishan Thodkar, Pierre Andre Cazade, Frank Bergmann, et al. “Self-assembled pyrene stacks and peptide monolayers tune the electronic properties of functionalized electrolyte-gated graphene field-effect transistors”. In: *ACS Applied Materials and Interfaces* 13.7 (Feb. 2021), pp. 9134–9142. ISSN: 19448252. DOI: 10.1021/ACSAAMI.0C18485/ASSET/IMAGES/LARGE/AM0C18485\_0006.JPG. URL: <https://pubs.acs.org/doi/full/10.1021/acsaami.0c18485>.
- [81] Carbonnanotube. *File:Noncovalent carboncarbonnanotube.png*. 2015. URL: [https://en.m.wikipedia.org/wiki/File:Noncovalent\\_carboncarbonnanotube.png](https://en.m.wikipedia.org/wiki/File:Noncovalent_carboncarbonnanotube.png) (visited on 2023-10-13).
- [82] Emilio M. Pérez and Nazario Martín. “ $\pi$ - $\pi$  interactions in carbon nanostructures”. In: *Chemical Society Reviews* 44.18 (Sept. 2015), pp. 6425–6433. ISSN: 1460-4744. DOI: 10.1039/C5CS00578G. URL: <https://pubs.rsc.org/en/content/articlehtml/2015/cs/c5cs00578g>%20<https://pubs.rsc.org/en/content/articlelanding/2015/cs/c5cs00578g>.
- [83] Chelsea R. Martinez and Brent L. Iverson. “Rethinking the term “pi-stacking””. In: *Chemical Science* 3.7 (June 2012), pp. 2191–2201. ISSN: 2041-6539. DOI: 10.1039/C2SC20045G. URL: <https://pubs.rsc.org/en/content/articlehtml/2012/sc/c2sc20045g>%20<https://pubs.rsc.org/en/content/articlelanding/2012/sc/c2sc20045g>.
- [84] Yan Zhou, Yi Fang, and Ramaraja P. Ramasamy. “Non-Covalent Functionalization of Carbon Nanotubes for Electrochemical Biosensor Development”. In: *Sensors (Basel, Switzerland)* 19.2 (Jan. 2019). ISSN: 1424-8220. DOI: 10.3390/S19020392. URL: <https://pubmed.ncbi.nlm.nih.gov/30669367/>.
- [85] J. A. M. J. Frisch and G. W. Trucks and H. B. Schlegel and G. E. Scuseria and M. A. Robb and J. R. Cheeseman and G. Scalmani and V. Barone and G. A. Petersson and H. Nakatsuji and X. Li and M. Caricato and A. V. Marenich and J. Bloino and B. G. Janesko and R. G. J. E. Peralta, F. Ogliaro, et al. *Gaussian~16 Revision C.01*. 2016.
- [86] Yasuhiro Oishi, Hirotugu Ogi, Satoshi Hagiwara, et al. “Theoretical Analysis on the Stability of 1-Pyrenebutanoic Acid Succinimidyl Ester Adsorbed on Graphene”. In: *ACS Omega* 7.35 (Sept. 2022), pp. 31120–31125. ISSN: 24701343. DOI: 10.1021/ACsomega.2C03257/ASSET/IMAGES/LARGE/AO2C03257\_0004.JPG. URL: <https://pubs.acs.org/doi/full/10.1021/acsomega.2c03257>.

- [87] Kenzo Maehashi, Taiji Katsura, Kagan Kerman, et al. “Label-free protein biosensor based on aptamer-modified carbon nanotube field-effect transistors”. In: *Analytical Chemistry* 79.2 (Jan. 2007), pp. 782–787. ISSN: 00032700. DOI: 10.1021/ac060830g. URL: <https://pubs.acs.org/doi/full/10.1021/ac060830g>.
- [88] Cristina García-Aljaro, Lakshmi N. Cella, Dhamanand J. Shirale, et al. “Carbon nanotubes-based chemiresistive biosensors for detection of microorganisms”. In: *Biosensors and Bioelectronics* 26.4 (Dec. 2010), pp. 1437–1441. ISSN: 09565663. DOI: 10.1016/j.bios.2010.07.077.
- [89] R. J. Chen, Y. Zhang, D. Wang, et al. “Noncovalent sidewall functionalization of single-walled carbon nanotubes for protein immobilization”. In: *Journal of the American Chemical Society* 123.16 (2001), pp. 3838–3839. ISSN: 00027863. DOI: 10.1021/ja010172b. URL: <http://pubs.acs.org..>
- [90] Lakshmi N. Cella, Pablo Sanchez, Wenwan Zhong, et al. “Nano aptasensor for Protective Antigen Toxin of Anthrax”. In: *Analytical Chemistry* 82.5 (Mar. 2010), pp. 2042–2047. ISSN: 00032700. DOI: 10.1021/ac902791q. URL: <https://pubs.acs.org/doi/full/10.1021/ac902791q>.
- [91] Basanta K. Das, Chaker Tlili, Sushmee Badhulika, et al. “Single-walled carbon nanotubes chemiresistor aptasensors for small molecules: Picomolar level detection of adenosine triphosphate”. In: *Chemical Communications* 47.13 (Mar. 2011), pp. 3793–3795. ISSN: 1364548X. DOI: 10.1039/c0cc04733c. URL: <https://pubs.rsc.org/en/content/articlehtml/2011/cc/c0cc04733c%20https://pubs.rsc.org/en/content/articlelanding/2011/cc/c0cc04733c>.
- [92] Koen Besteman, Jeong O. Lee, Frank G.M. Wiertz, et al. “Enzyme-coated carbon nanotubes as single-molecule biosensors”. In: *Nano Letters* 3.6 (June 2003), pp. 727–730. ISSN: 15306984. DOI: 10.1021/NL034139U. URL: <https://pubs.acs.org/doi/full/10.1021/nl034139u>.
- [93] Deana Kwong Hong Tsang, Tyler J. Lieberthal, Clare Watts, et al. “Chemically Functionalised Graphene FET Biosensor for the Label-free Sensing of Exosomes”. In: *Scientific Reports* 9.1 (Sept. 2019), pp. 1–10. ISSN: 20452322. DOI: 10.1038/s41598-019-50412-9. URL: <https://www.nature.com/articles/s41598-019-50412-9>.
- [94] Gregory R. Wiedman, Yanan Zhao, Arkady Mustaev, et al. “An Aptamer-Based Biosensor for the Azole Class of Antifungal Drugs”. In: *mSphere* 2.4 (Aug. 2017). ISSN: 23795042. DOI: 10.1128/msphere.00274-17. URL: [/pmc/articles/PMC5566834/](https://pmc.ncbi.nlm.nih.gov/pmc/articles/PMC5566834/)?report=abstract %20<https://www.ncbi.nlm.nih.gov/pmc/articles/PMC5566834/>.
- [95] Zhaoli Gao, Han Xia, Jonathan Zauberman, et al. “Detection of Sub-fM DNA with Target Recycling and Self-Assembly Amplification on Graphene Field-Effect Biosensors”. In: *Nano Letters* 18.6 (June 2018), pp. 3509–3515. ISSN: 15306992. DOI: 10.1021/acs.nanolett.8b00572. URL: <https://pubs.acs.org/doi/full/10.1021/acs.nanolett.8b00572>.

## Bibliography

- [96] Michael T. Hwang, B. Landon Preston, Lee Joon, et al. “Highly specific SNP detection using 2D graphene electronics and DNA strand displacement”. In: *Proceedings of the National Academy of Sciences of the United States of America* 113.26 (June 2016), pp. 7088–7093. ISSN: 10916490. DOI: 10.1073/pnas.1603753113. URL: <https://www.pnas.org/doi/abs/10.1073/pnas.1603753113>.
- [97] Zhuang Hao, Yunlu Pan, Cong Huang, et al. “Modulating the Linker Immobilization Density on Aptameric Graphene Field Effect Transistors Using an Electric Field”. In: *ACS Sensors* 5.8 (Aug. 2020), pp. 2503–2513. ISSN: 23793694. DOI: 10.1021/ACSSENSORS.0C00752/ASSET/IMAGES/LARGE/SE0C00752\_0008.JPG. URL: <https://pubs.acs.org/doi/full/10.1021/acssensors.0c00752>.
- [98] Mohd Maidin Nur Nasyifa, A. Rahim Ruslinda, Nur Hamidah Abdul Halim, et al. “Immuno-probed graphene nanoplatelets on electrolyte-gated field-effect transistor for stable cortisol quantification in serum”. In: *Journal of the Taiwan Institute of Chemical Engineers* 117 (Dec. 2020), pp. 10–18. ISSN: 18761070. DOI: 10.1016/j.jtice.2020.12.008.
- [99] Rui Campos, Jérôme Borme, Joana Rafaela Guerreiro, et al. “Attomolar label-free detection of dna hybridization with electrolyte-gated graphene field-effect transistors”. In: *ACS Sensors* 4.2 (Feb. 2019), pp. 286–293. ISSN: 23793694. DOI: 10.1021/acssensors.8b00344. URL: <https://pubs.acs.org/doi/full/10.1021/acssensors.8b00344>.
- [100] Murat Kuscu, Hamideh Ramezani, Ergin Dinc, et al. “Graphene-based Nanoscale Molecular Communication Receiver: Fabrication and Microfluidic Analysis”. In: (June 2020). arXiv: 2006.15470. URL: <https://arxiv.org/abs/2006.15470v2>.
- [101] Shicai Xu, Jian Zhan, Baoyuan Man, et al. “Real-time reliable determination of binding kinetics of DNA hybridization using a multi-channel graphene biosensor”. In: *Nature Communications* 8.1 (Mar. 2017), pp. 1–10. ISSN: 20411723. DOI: 10.1038/ncomms14902. URL: <https://www.nature.com/articles/ncomms14902>.
- [102] Niazul I. Khan, Mohammad Mousazadehkasir, Sujoy Ghosh, et al. “An integrated microfluidic platform for selective and real-time detection of thrombin biomarkers using a graphene FET”. In: *Analyst* 145.13 (June 2020), pp. 4494–4503. ISSN: 13645528. DOI: 10.1039/d0an00251h. URL: <https://pubs.rsc.org/en/content/articlehtml/2020/an/d0an00251h%20https://pubs.rsc.org/en/content/articlelanding/2020/an/d0an00251h>.
- [103] T Ono, K Kamada, R Hayashi, et al. “Lab-on-a-graphene-FET detection of key molecular events underpinning influenza 2 virus infection and effect of antiviral drugs 3 Running title: Graphene-FET detects reactions in an influenza infection MAIN TEXT”. In: *bioRxiv* (Mar. 2020), p. 2020.03.18.996884. DOI: 10.1101/2020.03.18.996884. URL: <https://doi.org/10.1101/2020.03.18.996884>.

- [104] Han Yue Zheng, Omar A. Alsager, Bicheng Zhu, et al. “Electrostatic gating in carbon nanotube aptasensors”. In: *Nanoscale* 8.28 (July 2016), pp. 13659–13668. ISSN: 20403372. DOI: 10.1039/c5nr08117c. URL: <https://pubs.rsc.org/en/content/articlehtml/2016/nr/c5nr08117c%20https://pubs.rsc.org/en/content/articlelanding/2016/nr/c5nr08117c>.
- [105] Jun Pyo Kim, Byung Yang Lee, Joohyung Lee, et al. “Enhancement of sensitivity and specificity by surface modification of carbon nanotubes in diagnosis of prostate cancer based on carbon nanotube field effect transistors”. In: *Biosensors and Bioelectronics* 24.11 (July 2009), pp. 3372–3378. ISSN: 09565663. DOI: 10.1016/j.bios.2009.04.048. URL: <https://pubmed.ncbi.nlm.nih.gov/19481922/>.
- [106] Jagriti Sethi, Michiel Van Bulck, Ahmed Suhail, et al. “A label-free biosensor based on graphene and reduced graphene oxide dual-layer for electrochemical determination of beta-amyloid biomarkers”. In: *Microchimica Acta* 187.5 (May 2020), pp. 1–10. ISSN: 14365073. DOI: 10.1007/s00604-020-04267-x. URL: <https://link.springer.com/article/10.1007/s00604-020-04267-x>.
- [107] Yasuhide Ohno, Kenzo Maehashi, and Kazuhiko Matsumoto. “Label-free biosensors based on aptamer-modified graphene field-effect transistors”. In: *Journal of the American Chemical Society* 132.51 (Dec. 2010), pp. 18012–18013. ISSN: 00027863. DOI: 10.1021/ja108127r. URL: <https://pubs.acs.org/doi/full/10.1021/ja108127r>.
- [108] Ryan J. Lopez, Sofia Babanova, Kateryna Artyushkova, et al. “Surface modifications for enhanced enzyme immobilization and improved electron transfer of PQQ-dependent glucose dehydrogenase anodes”. In: *Bioelectrochemistry* 105 (Oct. 2015), pp. 78–87. ISSN: 1878562X. DOI: 10.1016/j.bioelechem.2015.05.010. URL: <https://pubmed.ncbi.nlm.nih.gov/26011132/>.
- [109] Guinevere Strack, Robert Nichols, Plamen Atanassov, et al. “Modification of carbon nanotube electrodes with 1-pyrenebutanoic acid, succinimidyl ester for enhanced bioelectrocatalysis”. In: *Methods in Molecular Biology* 1051 (2013), pp. 217–228. ISSN: 10643745. DOI: 10.1007/978-1-62703-550-7\_14. URL: <https://pubmed.ncbi.nlm.nih.gov/23934807/>.
- [110] Greg T. Hermanson. “The Reactions of Bioconjugation”. In: *Bioconjugate Techniques* (Jan. 2013), pp. 229–258. DOI: 10.1016/B978-0-12-382239-0.00003-0.
- [111] Malcolm Hinnemo, Jie Zhao, Patrik Ahlberg, et al. “On Monolayer Formation of Pyrenebutyric Acid on Graphene”. In: *Langmuir* 33.15 (Apr. 2017), pp. 3588–3593. ISSN: 15205827. DOI: 10.1021/ACS.LANGMUIR.6B04237/ASSET/IMAGES/LARGE/LA-2016-04237V\_0003.JPG. URL: <https://pubs.acs.org/doi/full/10.1021/acs.langmuir.6b04237>.
- [112] Xue V. Zhen, Emily G. Swanson, Justin T. Nelson, et al. “Noncovalent monolayer modification of graphene using pyrene and cyclodextrin receptors for chemical sensing”. In: *ACS Applied Nano Materials* 1.6 (June 2018), pp. 2718–2726. ISSN:

## Bibliography

25740970. DOI: 10.1021/acsanm.8b00420. URL: <https://pubs.acs.org/doi/full/10.1021/acsanm.8b00420>.
- [113] Ryan J. White, Noelle Phares, Arica A. Lubin, et al. “Optimization of electrochemical aptamer-based sensors via optimization of probe packing density and surface chemistry”. In: *Langmuir : the ACS journal of surfaces and colloids* 24.18 (Sept. 2008), pp. 10513–10518. ISSN: 0743-7463. DOI: 10.1021/LA800801V. URL: <https://pubmed.ncbi.nlm.nih.gov/18690727/>.
- [114] Yu Chen, Tze Sian Pui, Patthara Kongsuphol, et al. “Aptamer-based array electrodes for quantitative interferon- $\gamma$  detection”. In: *Biosensors and Bioelectronics* 53 (Mar. 2014), pp. 257–262. ISSN: 1873-4235. DOI: 10.1016/J.BIOS.2013.09.046. URL: <https://pubmed.ncbi.nlm.nih.gov/24144556/>.
- [115] Greg T. Hermanson. “Homobifunctional Crosslinkers”. In: *Bioconjugate Techniques* (Jan. 2013), pp. 275–298. DOI: 10.1016/B978-0-12-382239-0.00005-4.
- [116] *1-Pyrenebutyric acid N-hydroxysuccinimide ester - [1H NMR] - Spectrum - SpectraBase*. URL: <https://spectrabase.com/spectrum/FxRoJanrm9t> (visited on 2023-10-19).
- [117] R. G. Lebel and D. A.I. Goring. “Density, Viscosity, Refractive Index, and Hygroscopicity of Mixtures of Water and Dimethyl Sulfoxide”. In: *Journal of Chemical and Engineering Data* 7.1 (Jan. 1962), pp. 100–101. ISSN: 15205134. DOI: 10.1021/JE60012A032 / ASSET / JE60012A032.FP.PNG\_V03. URL: <https://pubs.acs.org/doi/abs/10.1021/je60012a032>.
- [118] Alexander B. Artyukhin, Michael Stadermann, Raymond W. Friddle, et al. “Controlled electrostatic gating of carbon nanotube FET devices”. In: *Nano Letters* 6.9 (Sept. 2006), pp. 2080–2085. ISSN: 15306984. DOI: 10.1021/NL061343J / SUPPL\_FILE/NL061343JSI20060609\_104449.PDF. URL: <https://pubs.acs.org/doi/full/10.1021/nl061343j>.
- [119] M. Mohsen-Nia, H. Amiri, and B. Jazi. “Dielectric constants of water, methanol, ethanol, butanol and acetone: Measurement and computational study”. In: *Journal of Solution Chemistry* 39.5 (2010), pp. 701–708. ISSN: 00959782. DOI: 10.1007/S10953-010-9538-5.
- [120] Johannes Hunger, Richard Buchner, Mohamed E. Kandil, et al. “Relative permittivity of dimethylsulfoxide and N, N -dimethylformamide at temperatures from (278 to 328) K and pressures from (0.1 to 5) MPa”. In: *Journal of Chemical and Engineering Data* 55.5 (May 2010), pp. 2055–2065. ISSN: 00219568. DOI: 10.1021/JE9010773 / SUPPL\_FILE / JE9010773\_SI\_001.PDF. URL: <https://pubs.acs.org/doi/full/10.1021/je9010773>.
- [121] Ning Gao, Teng Gao, Xiao Yang, et al. “Specific detection of biomolecules in physiological solutions using graphene transistor biosensors”. In: *Proceedings of the National Academy of Sciences of the United States of America* 113.51 (Dec. 2016), pp. 14633–14638. ISSN: 10916490. DOI: 10.1073/PNAS.1625010114 /

- SUPPL\_FILE/PNAS.201625010SI.PDF. URL: <https://www.pnas.org/doi/abs/10.1073/pnas.1625010114>.
- [122] Kyoungseon Min, Jungbae Kim, Kyungmoon Park, et al. “Enzyme immobilization on carbon nanomaterials: Loading density investigation and zeta potential analysis”. In: *Journal of Molecular Catalysis B: Enzymatic* 83 (Nov. 2012), pp. 87–93. ISSN: 1381-1177. DOI: 10.1016/J.MOLCATB.2012.07.009.
- [123] Xuan Xu, Jiachao Yu, Jing Qian, et al. “Functionalization of nitrogen-doped carbon nanotubes by 1-pyrenebutyric acid and its application for biosensing”. In: *IEEE Sensors Journal* 14.7 (2014), pp. 2341–2346. ISSN: 1530437X. DOI: 10.1109/JSEN.2014.2309974.
- [124] Mercè Pacios, Iñigo Martin-Fernandez, Xavier Borrisé, et al. “Real time protein recognition in a liquid-gated carbon nanotube field-effect transistor modified with aptamers”. In: *Nanoscale* 4.19 (Sept. 2012), pp. 5917–5923. ISSN: 2040-3372. DOI: 10.1039/C2NR31257C. URL: <https://pubs.rsc.org/en/content/articlehtml/2012/nr/c2nr31257c%20https://pubs.rsc.org/en/content/articlelanding/2012/nr/c2nr31257c>.
- [125] Marcin S. Filipiak, Marcel Rother, Nesha M. Andoy, et al. “Highly sensitive, selective and label-free protein detection in physiological solutions using carbon nanotube transistors with nanobody receptors”. In: *Sensors and Actuators B: Chemical* 255 (Feb. 2018), pp. 1507–1516. ISSN: 0925-4005. DOI: 10.1016/J.SNB.2017.08.164.
- [126] Jie Liu, Florence Appaix, Olivier Bibari, et al. “Control of neuronal network organization by chemical surface functionalization of multi-walled carbon nanotube arrays”. In: *Nanotechnology* 22.19 (May 2011). ISSN: 1361-6528. DOI: 10.1088/0957-4484/22/19/195101. URL: <https://pubmed.ncbi.nlm.nih.gov/21436508/>.
- [127] Christoph Fenzl, Pranati Nayak, Thomas Hirsch, et al. “Laser-Scribed Graphene Electrodes for Aptamer-Based Biosensing”. In: *ACS sensors* 2.5 (May 2017), pp. 616–620. ISSN: 2379-3694. DOI: 10.1021/ACSSENSORS.7B00066. URL: <https://pubmed.ncbi.nlm.nih.gov/28723173/>.
- [128] Deepak Sehgal and Inder K. Vijay. “A Method for the High Efficiency of Water-Soluble Carbodiimide-Mediated Amidation”. In: *Analytical Biochemistry* 218.1 (Apr. 1994), pp. 87–91. ISSN: 0003-2697. DOI: 10.1006/ABIO.1994.1144.
- [129] Greg T. Hermanson. “Zero-Length Crosslinkers”. In: *Bioconjugate Techniques* (Jan. 2013), pp. 259–273. DOI: 10.1016/B978-0-12-382239-0.00004-2.
- [130] Greg T. Hermanson. “Microparticles and Nanoparticles”. In: *Bioconjugate Techniques* (Jan. 2013), pp. 549–587. DOI: 10.1016/B978-0-12-382239-0.00014-5.
- [131] Gang Wei, Changjiang Pan, Jörg Reichert, et al. “Controlled assembly of protein-protected gold nanoparticles on noncovalent functionalized carbon nanotubes”. In: *Carbon* 48.3 (Mar. 2010), pp. 645–653. ISSN: 0008-6223. DOI: 10.1016/J.CARBON.2009.10.006.

## Bibliography

- [132] Meng Lan, Guoli Fan, Wei Sun, et al. “Synthesis of hybrid Zn–Al–In mixed metal oxides/carbon nanotubes composite and enhanced visible-light-induced photocatalytic performance”. In: *Applied Surface Science* 282 (Oct. 2013), pp. 937–946. ISSN: 0169-4332. DOI: 10.1016/J.APSUSC.2013.06.095.
- [133] Mitchell B. Lerner, James M. Resczenski, Akshay Amin, et al. “Toward quantifying the electrostatic transduction mechanism in carbon nanotube molecular sensors”. In: *Journal of the American Chemical Society* 134.35 (Sept. 2012), pp. 14318–14321. ISSN: 00027863. DOI: 10.1021/JA306363V/SUPPL\_FILE/JA306363V\_SI\_001.PDF. URL: <https://pubs.acs.org/doi/full/10.1021/ja306363v>.
- [134] Michael Holzinger, Jessica Baur, Raoudha Haddad, et al. “Multiple functionalization of single-walled carbon nanotubes by dip coating”. In: *Chemical Communications* 47.8 (Feb. 2011), pp. 2450–2452. ISSN: 1364-548X. DOI: 10.1039/C0CC03928D. URL: <https://pubs.rsc.org/en/content/articlehtml/2011/cc/c0cc03928d%20https://pubs.rsc.org/en/content/articlelanding/2011/cc/c0cc03928d>.
- [135] Yoshihisa Amano, Ayako Koto, Shohei Matsuzaki, et al. “Construction of a biointerface on a carbon nanotube surface for efficient electron transfer”. In: *Materials Letters* 174 (July 2016), pp. 184–187. ISSN: 0167-577X. DOI: 10.1016/J.MATLET.2016.03.113.
- [136] Y. Y. Chang, H. Li, and H. Sun. “Immobilized Metal Affinity Chromatography (IMAC) for Metalloproteomics and Phosphoproteomics”. In: *Inorganic and Organometallic Transition Metal Complexes with Biological Molecules and Living Cells* (Jan. 2017), pp. 329–353. DOI: 10.1016/B978-0-12-803814-7.00009-5.
- [137] Alexander Star, Jean Christophe P. Gabriel, Keith Bradley, et al. “Electronic detection of specific protein binding using nanotube FET devices”. In: *Nano Letters* 3.4 (Apr. 2003), pp. 459–463. ISSN: 15306984. DOI: 10.1021/NL0340172. URL: <https://pubs.acs.org/doi/full/10.1021/nl0340172>.
- [138] Christopher M. Dundas, Daniel Demonte, and Sheldon Park. “Streptavidin-biotin technology: Improvements and innovations in chemical and biological applications”. In: *Applied Microbiology and Biotechnology* 97.21 (Nov. 2013), pp. 9343–9353. ISSN: 01757598. DOI: 10.1007/S00253-013-5232-Z/FIGURES/3. URL: <https://link.springer.com/article/10.1007/s00253-013-5232-z>.
- [139] Greg T. Hermanson. “(Strept)avidin–Biotin Systems”. In: *Bioconjugate Techniques* (Jan. 2013), pp. 465–505. DOI: 10.1016/B978-0-12-382239-0.00011-X.
- [140] Michael Fairhead and Mark Howarth. “Site-specific biotinylation of purified proteins using BirA”. In: *Methods in molecular biology (Clifton, N.J.)* 1266 (2015), p. 171. ISSN: 10643745. DOI: 10.1007/978-1-4939-2272-7\_12. URL: /pmc/articles/PMC4304673/%20/pmc/articles/PMC4304673/?report=abstract%20https://www.ncbi.nlm.nih.gov/pmc/articles/PMC4304673/.

- [141] Greg T. Hermanson. “PEGylation and Synthetic Polymer Modification”. In: *Bioconjugate Techniques* (Jan. 2013), pp. 787–838. DOI: 10.1016/B978-0-12-382239-0.00018-2.
- [142] Mehdi Meran, Pelin Deniz Akkus, Ozge Kurkcuoglu, et al. “Noncovalent Pyrene-Polyethylene Glycol Coatings of Carbon Nanotubes Achieve in Vitro Biocompatibility”. In: *Langmuir* 34.40 (Oct. 2018), pp. 12071–12082. ISSN: 15205827. DOI: 10.1021/ACS.LANGMUIR.8B00971. URL: <https://pubs.acs.org/doi/full/10.1021/acs.langmuir.8b00971>.
- [143] Hiroko Miki, Atsunobu Isobayashi, Tatsuro Saito, et al. “Ionic liquids with wafer-scalable graphene sensors for biological detection”. In: *IEEE Transactions on Nanobioscience* 18.2 (Apr. 2019), pp. 216–219. ISSN: 15361241. DOI: 10.1109/TNB.2019.2905286.
- [144] Nozomi Nakayama-Ratchford, Sarunya Bangsaruntip, Xiaoming Sun, et al. “Non-Covalent Functionalization of Carbon Nanotubes by Fluorescein-Polyethylene Glycol: Supramolecular Conjugates with pH Dependent Absorbance and Fluorescence”. In: *Journal of the American Chemical Society* 129.9 (Mar. 2007), p. 2448. ISSN: 00027863. DOI: 10.1021/JA068684J. URL: /pmc/articles/PMC4161124/%20/pmc/articles/PMC4161124/?report=abstract%20https://www.ncbi.nlm.nih.gov/pmc/articles/PMC4161124/.
- [145] Zhenghai Tang, Yanda Lei, Baochun Guo, et al. “The use of rhodamine B-decorated graphene as a reinforcement in polyvinyl alcohol composites”. In: *Polymer* 53.2 (Jan. 2012), pp. 673–680. ISSN: 0032-3861. DOI: 10.1016/J.POLYMER.2011.11.056.
- [146] Maria G. Khrenova, Alexander V. Nemukhin, and Vladimir G. Tsirelson. “Origin of the  $\pi$ -stacking induced shifts in absorption spectral bands of the green fluorescent protein chromophore”. In: *Chemical Physics* 522 (June 2019), pp. 32–38. ISSN: 0301-0104. DOI: 10.1016/J.CHEMPHYS.2019.02.010.
- [147] Yuan Qiu, Haisi Hu, Dongxu Zhao, et al. “Concentration-dependent dye aggregation and disassembly triggered by the same artificial helical foldamer”. In: *Polymer* 170 (Apr. 2019), pp. 7–15. ISSN: 0032-3861. DOI: 10.1016/J.POLYMER.2019.02.063.
- [148] Jeng Hao Pai, Yuli Wang, Gina To A. Salazar, et al. “A Photoresist with Low Fluorescence for Bioanalytical Applications”. In: *Analytical chemistry* 79.22 (Nov. 2007), p. 8774. ISSN: 00032700. DOI: 10.1021/AC071528Q. URL: /pmc/articles/PMC2435225/%20/pmc/articles/PMC2435225/?report=abstract%20https://www.ncbi.nlm.nih.gov/pmc/articles/PMC2435225/.
- [149] Ali Ashraf, Yanbin Wu, Michael C. Wang, et al. “Spectroscopic investigation of the wettability of multilayer graphene using highly ordered pyrolytic graphite as a model material”. In: *Langmuir* 30.43 (Nov. 2014), pp. 12827–12836. ISSN: 15205827. DOI: 10.1021/LA503089K/SUPPL\_FILE/LA503089K\_SI\_001.PDF. URL: <https://pubs.acs.org/doi/full/10.1021/la503089k>.

## Bibliography

- [150] Grzegorz Stando, Damian Łukawski, Filip Lisiecki, et al. “Intrinsic hydrophilic character of carbon nanotube networks”. In: *Applied Surface Science* 463 (Jan. 2019), pp. 227–233. ISSN: 0169-4332. DOI: 10.1016/J.APSUSC.2018.08.206.
- [151] Minsuk Park, In Seung Choi, and Sang Yong Ju. “Quantification and removal of carbonaceous impurities in a surfactant-assisted carbon nanotube dispersion and its implication on electronic properties”. In: *Nanoscale Advances* 4.17 (Aug. 2022), pp. 3537–3548. ISSN: 2516-0230. DOI: 10.1039/D2NA00153E. URL: <https://pubs.rsc.org/en/content/articlehtml/2022/na/d2na00153e%20https://pubs.rsc.org/en/content/articlelanding/2022/na/d2na00153e>.
- [152] Young Jun Shin, Yingying Wang, Han Huang, et al. “Surface-energy engineering of graphene”. In: *Langmuir* 26.6 (Mar. 2010), pp. 3798–3802. ISSN: 07437463. DOI: 10.1021/LA100231U/ASSET/IMAGES/LARGE/LA-2010-00231U\_0005.JPEG. URL: <https://pubs.acs.org/doi/full/10.1021/la100231u>.
- [153] Creative PEGWorks. *Functionalisation with Pyrene-PEG-Rhodamine*. 2022.
- [154] Shunsuke F. Shimobayashi, Mikiko Tsudome, and Tomo Kurimura. “Suppression of the coffee-ring effect by sugar-assisted depinning of contact line”. In: *Scientific Reports* 2018 8:1 8.1 (Dec. 2018), pp. 1–9. ISSN: 2045-2322. DOI: 10.1038/s41598-018-35998-w. URL: <https://www.nature.com/articles/s41598-018-35998-w>.
- [155] K. Bradley, M. Briman, A. Star, et al. “Charge Transfer from Adsorbed Proteins”. In: *Nano Letters* 4.2 (Feb. 2004), pp. 253–256. ISSN: 15306984. DOI: 10.1021/NL034985. URL: <https://pubs.acs.org/doi/full/10.1021/nl034985>.
- [156] Abhinav Nath, William M. Atkins, and Stephen G. Sligar. “Applications of phospholipid bilayer nanodiscs in the study of membranes and membrane proteins”. In: *Biochemistry* 46.8 (Feb. 2007), pp. 2059–2069. ISSN: 00062960. DOI: 10.1021/BI602371N/ASSET/IMAGES/LARGE/BI602371NF00005.JPG. URL: <https://pubs.acs.org/doi/full/10.1021/bi602371n>.
- [157] Timothy H. Bayburt and Stephen G. Sligar. “Membrane protein assembly into Nanodiscs”. In: *FEBS letters* 584.9 (May 2010), pp. 1721–1727. ISSN: 1873-3468. DOI: 10.1016/J.FEBSLET.2009.10.024. URL: <https://pubmed.ncbi.nlm.nih.gov/19836392/>.